EVALUATING RESERVE BRIDGE CAPACITY

THROUGH DESTRUCTIVE TESTING

OF A DECOMISSIONED BRIDGE

by

Kervin Michaud

A thesis submitted to the Faculty of the University of Delaware in partial
fulfillment of the requirements for the degree of Master of Civil Engineering

Winter 2011

EVALUATING RESERVE BRIDGE CAPACITY

THROUGH DESTRUCTIVE TESTING

OF A DECOMISSIONED BRIDGE

by

Kervin Michaud

Approved: _____
Michael J. Chajes, Ph.D.
Professor in charge of thesis on behalf of the Advisory Committee

Approved: _____
Jennifer E. Righman McConnell, Ph.D.
Professor in charge of thesis on behalf of the Advisory Committee

Approved: _____
Harry W. Shenton III, Ph.D.
Chair of the Department of Civil and Environmental Engineering

Approved: _____
Michael J. Chajes, Ph.D.
Dean of the College of Engineering

Approved: _____
Charles G. Riordan, Ph.D.
Vice Provost for Graduate and Professional Education

ACKNOWLEDGMENTS

TABLE OF CONTENTS

APPENDICES

LIST OF TABLES

LIST OF FIGURES

ABSTRACT

This thesis provides testing results from a unique full-scale destructive bridge test of a skewed steel plate girder bridge located in Wilmington, Delaware. The goal of the test was to load the structure beyond its elastic limit to observe transverse load redistribution and to examine the reserve capacity of the structure. The bridge is the second in a series of eight bridges to be decommissioned by the owner, the Delaware River Bay and Authority (DRBA) and the second bridge that was tested by the University of Delaware. The bridge studied here was in good condition and was only decommissioned as part of a traffic realignment project. The bridge was loaded using a loading mechanism consisting of a reaction frame comprised of stiffened girders, coil rods embedded in a mass of concrete covered with backfill beneath the bridge, and hydraulic jacks. Numerous strain gauges were used to monitor the response of the bridge during testing.

The equivalent of 17 HS-20 vehicles was applied during the testing without any yielding being recorded in the girders. As a result of the limited applied loading (which was governed by the capacity of the coil rods), a detailed finite element model was calibrated using the recorded response of the bridge. The numerical model was used to predict the post elastic response of the bridge, as well as the structure's ultimate capacity of 30 HS-20 vehicles. The design codes predicted

capacity of 12 HS-20 vehicles, which demonstrates the significant reverse capacity of the structure.

Other conclusions from this work are that the loading mechanism was an efficient way of loading the bridge and is promising for use during future destructive bridge tests. Ultimate strength predictions from finite element analysis should be used to determine the required capacity of the loading mechanism and design it accordingly in order to ensure that post-elastic response can be captured.

Chapter 1

INTRODUCTION

1.1 Motivation

Modern bridge design codes are primarily based on one-dimensional "line-girder" analyses and the capacity of individual structural members. The line-girder approach simplifies bridge design, but does not consider how load is redistributed throughout the structure once the response enters the inelastic regime. This redistribution between girders after yielding can be significant. Cross frames, diaphragms, and the deck most likely play a large role in this load redistribution. Thus, only by using a system-level approach to examining the bridge can this load redistribution be completely evaluated. Employing a system-level approach will yield a more accurate estimate for the load capacity of a bridge, and this capacity is likely to be higher than the capacity predicted by a line-girder approach.

While finding a bridge's capacity using a line-girder approach is quite common, finding the ultimate capacity using a more accurate system-level approach is far less typical. It has been well documented that the nation's bridge infrastructure is in desperate need of an overhaul. Thus a better understanding of the system-level ultimate limit states and response of the bridges would provide the opportunity for a better recognition and prioritization of the most deficient structures. Using a system-level approach could also result in more efficiently designed structures. Thus, a better

understanding of the system performance of bridges can help bridge owners prioritize the limited financial resources available for constructing and maintaining our nation's bridge infrastructures.

1.2   Objective

The best way to learn about the ultimate capacity of bridges is to conduct full-scale destructive bridge tests. However, such opportunities are rare because bridges that are in good enough condition to result in a useful test are rarely decommissioned and made available to researchers. Fortunately, an opportunity to conduct such a full-scale destructive bridge test presented itself to researchers at the University of Delaware and was conducted on October 8, 2010. This thesis documents results from this unique destructive bridge test designed to study system-level reserve bridge capacity.

The primary objective of this thesis is to study the actual ultimate load capacity of a specific bridge and compare that capacity to what current design codes predict. By doing so, a better understanding of load redistribution, initiated as one or more girders begin to yield, will be achieved. The study of the system-level behavior is based on both the full-scale test results as well as a calibrated finite element model of the bridge.

1.3   Thesis Outline

This thesis will present not only the execution and results of a full-scale destructive bridge, but also the response and ultimate capacity of the bridge that is predicted using a calibrated finite element model. The materials presented are organized as follows.

Chapter 2 presents a detailed description of the bridge as well as the background leading up to the destructive bridge test, including prior tests that aided in developing both the test plan and the finite element model.

Chapter 3 describes the loading mechanism and procedure that was used to load the bridge. A detailed description of the loading mechanism is also found in this chapter.

Chapter 4 presents the instrumentation setup used for the test, as well as the data resulting from the test. An explanation of how the raw test results were converted into data used to validate the finite element model is also presented in this chapter.

Chapter 5 compares and calibrates the numerical bridge model with the field test data. Using the calibrated model, the system-level ultimate capacity and post-elastic response of the structure is evaluated.

Chapter 6 presents the conclusions of the study. This chapter also provides recommendations for improving future full-scale destructive bridge tests.

Chapter 2

BACKGROUND

2.1   Project History

The Delaware River & Bay Authority (DRBA) is currently in the process of removing eight existing bridges in order to realign and improve traffic conditions on the Delaware side of the Delaware Memorial Bridge. Bridge 11 and Bridge 7R were the first two bridges that have been removed. During this process, DRBA has given the University of Delaware the opportunity to destructively load test the behavior of these structures.

Bridge 11 was the first bridge to be tested by the University of Delaware. This bridge served as one of the exit ramps off of Interstate 295. The main objective of the test was to evaluate the behavior of the bridge when loaded to its ultimate capacity and understand the manner in which the bridge redistributed loads. The bridge was loaded with over 2 million pounds of asphalt millings. This method of loading the structure was the most efficient option available due to the limited time constrains and budget of the project. The bridge response was monitored through the 102 strain gauges that were attached to the structure. The findings from the Bridge 11 test noted that for

4

future bridge tests a Finite Element Model (FEM) that predicted the bridge behavior during testing should be completed. The FEM will allow the user to examine any area and response (strain, stress, displacement, etc.) of the bridge instead of only the areas that were instrumented. The results from Bridge 11 also suggested other methods to improve the testing methods for Bridge 7R. A thorough discussion of the results from Bridge 11 was given by Quinn (2005).

Bridge 7R was the second bridge that the DRBA has made available to the University of Delaware for a destructive bridge test and is the subject of this thesis. A detailed description of the bridge is discussed in Section 2.2 herein. The destructive bridge test was originally scheduled to take place in the spring of 2007. However, due to unforeseeable delays in the construction process, the testing was not conducted until October 2010. Therefore other tests pertaining to Bridge 7R were done during the intervening time to better understand the bridge before testing the structure.

A diagnostic test of the actual structure under service loads was the first completed bridge test pertaining to Bridge 7R. This diagnostic test was completed by Ross (2007). The other test was a 1/5th-scaled destructive test that mimicked Bridge 7R and was completed by Bechtel (2009). Additional information on these previous tests will be given in Sections 2.3 and 2.4. Both tests provided critical information used in validating and improving the FEM of the full size and scaled bridges. Both of these previous studies also included finite element analysis (FEA) of the respective structures. The diagnostic test was useful for examining the bridge at elastic load levels while the scaled test was useful for examining the bridge at post-elastic load levels. The commercial software FEMAP 9.2 was used for preprocessing while ABAQUS 6.7-1 was
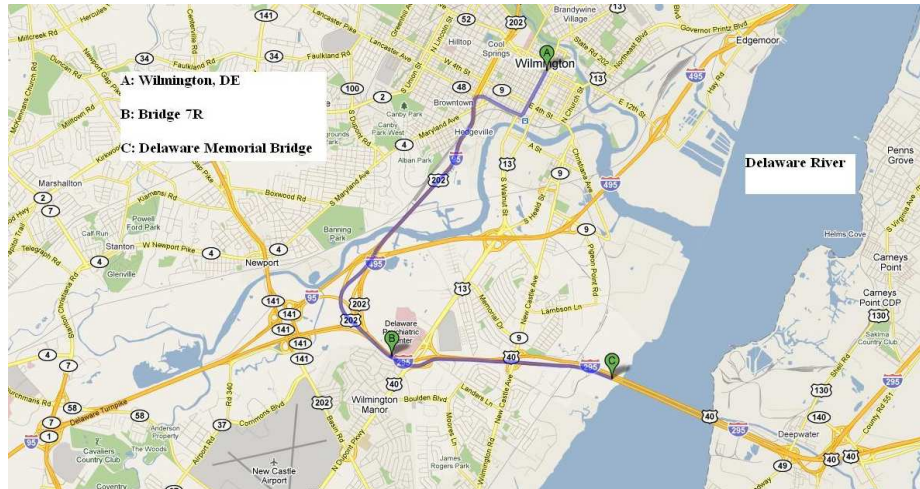
Figure 2.1   Map of Bridge 7R Site

used for analysis and post-processing of both structures. Bechtel et al (2011) also
reviewed other relevant literature relating to destructive testing and associated modeling
of steel bridges.

2.2   Bridge History

2.2.1   Bridge 7R Location

Bridge 7R is located 4 miles south of Wilmington, DE and 2.7 miles west of
The Delaware Memorial Bridge. Refer to Figure 2.1 for a map of the bridge location
with respect to these specific locations. The structure served as an exit ramp that allowed
vehicles traveling from Interstate 295 North to enter North DuPont Parkway (Routes 13
south / 40 west). The exit ramp is the first exit for vehicles traveling onto Interstate 295
North from Interstate 95 (North or South). Figure 2.2 displays a closer satellite view of
Bridge 7R that is denoted by the star. Baylor Boulevard is the roadway that crosses
underneath Bridge 7R, which can be seen in this figure.

Figure 2.2   Satellite View of Bridge 7R

2.2.2   Structural Description

Bridge 7R was designed in 1958 and its construction was completed in 1962. The bridge is a three span steel girder bridge that is vertically supported by two concrete abutments and two intermediate concrete piers. The spans of the bridge are simply supported and extend 105.33 ft in length. The destructive test that is the focal point of this thesis occurred on the middle span of the bridge. A plan view of the middle span can be seen in Figure 2.3. The bridge consists of four ASTM-A7 steel plate girders that are spaced 8 ft on center with exterior girders spaced 2 ft away from the outer edge of the bridge parapets. Thus, the total width of the bridge measures 28 ft. On both sides of the bridge there are 18 in. wide concrete parapets, 30 in. wide sidewalks and steel handrails. Thus, the width of the roadway is 20 ft. The bridge girders and abutments are on a 63 degree skew from tangent to the supports.
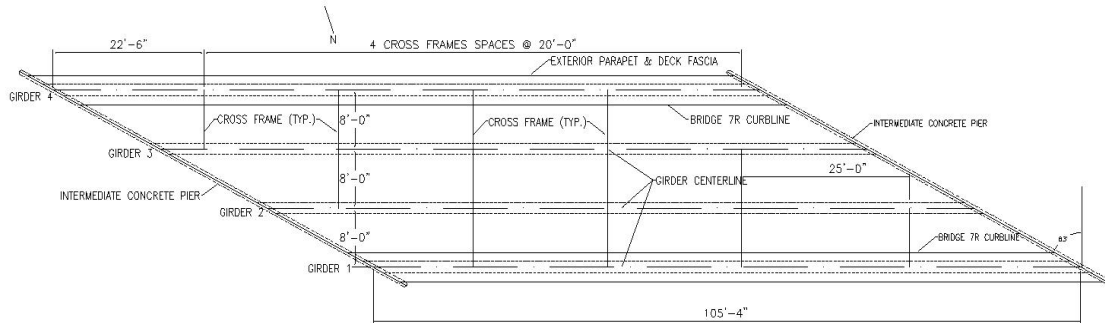
Figure 2.3   Plan View of Middle Span

The webs of the plate girders are 60 x 3/8 in. The exterior girders have a 20 x 1 in. top flange and a 20 x 1¼ in. bottom flange. The interior girders have an 18 x 7/8 in. top flange and a 20 x 1 in. bottom flange. Cover plates measuring 1½ in. thick and 20 in. wide were welded to the bottom flanges of the interior girders, 32.75 ft on either side of the centerline. Cover plates measuring 1-7/8 in. thick and 20 in. wide were welded to the bottom flanges of the exterior girders, 32.25 ft on each side of the centerline. The web was stiffened with double-sided transverse stiffeners on the interior girders and single-sided transverse stiffeners and single-sided longitudinal stiffeners on the exterior girders. Shear connectors connect the girder with the 8 in. thick concrete deck, creating composite action between the two members.

"K"-shaped cross frames are spaced 20 ft on center along the bridge to laterally brace the girders. The cross frames are constructed of 4x3½ x3/8 in. double

steel angles and are connected together by bolts and gusset plates as shown in Figure 2.4. The steel angle forming the bottom chord of the cross frame has its upper leg connected to the gusset plates that are also connected to the transverse stiffeners, which also serve as cross frame connection plates in these locations. The steel angle forming the top of the cross frames has its bottom leg connected to the connection plates. The inclined members of the cross frames have their bottom legs connected to gusset plates that are also attached to the other angles. Which leg of the angle that was directly connected to the structure was later considered in developing the instrumentation plan, as described in Section 4.4. In addition to the cross frames, end diaphragms were used to brace the end of the girders. The steel plate girder diaphragms were equal in depth to the steel girders.

Figure 2.4   Cross Frame to Gusset Plate Connection

9

Prior to the bridge test, the concrete parapets were removed in order to make validating the modeling of the bridge easier due to the uncertainty regarding the contribution of the parapets and to decrease the amount of loading needed to cause failure of the bridge. The parapets of the bridge give the bridge some additional strength that was not accounted for in the design of the bridge, which is created from the composite connection between the bridge and parapet, similar to the composite connection of the bridge deck and plate girders. Figure 2.5 shows a photo of the bridge before the test.

Figure 2.5   Photo of middle span w/ parapets removed

2.2.3   Neutral Axis Location of Girders

The calculated neutral axis locations were 50.8 in. from the base of the

bottom flange for the interior girders and 45.7 in. at the exterior girders for the midspan

portions of the girders where cover plates exist. These values were based upon the

weight of concrete equaling 150 pounds per cubic (pcf) and a compressive strength of

concrete of 9,000 psi. This value was based on the compressive strength value

corresponding to the calibration of the FEA, described in Section 5.1.4. (If a

conventional compressive strength of 4,000 psi is used, the neutral axis locations

decrease to 46.1 in. and 40.7 in for the interior and exterior girders, respectively.) The

effective concrete width used for the interior girders was 8 ft, while 6 ft was used for the

exterior girders. The different flange sizes of the interior and exterior girders were also

taken into account in the calculations. That the exterior girders have bottom flanges that

are more than half an inch thicker and effective concrete widths that are 2 ft smaller than

the interior girders is why the neutral axis locations is significantly lower in the exterior

girders.

2.3   Diagnostic Bridge Test

The diagnostic load test took place on November 23, 2005. The test was

conducted by driving a fully loaded triaxle dump truck across the bridge. The test was

conducted to ensure that the structural members of the bridge were functioning as they

were initially designed to and measure the transverse load distribution between girders.

The following subsections will go into specific detail pertaining to the diagnostic test that

was performed on Bridge 7R. Section 2.3.1 will explain the instrumentation setup of the

test and Section 2.3.2 will provide the results of the test.

Section 2.3.3 compares the diagnostic test data with the FEA results. The model was created with the intent to predict the bridge's inelastic response during the destructive test. Therefore, a validation of the FEM was completed by comparing the FEA data with the diagnostic test data. The reader is referred to Ross (2007) for a complete description of the diagnostic testing and associated FEA.

2.3.1 Diagnostic Test Procedures

The displacement of the bridge was measured by two potentiometers that were located at the midspans of Girders 2 and 3. A total of eight strain gauges were installed on Bridge 7R to measure the strain response of the bridge. Four strain gauges were installed at the bottom fascia of the bottom flange on each girder's midspan. Two more gauges were installed on the bottom fascia of the top flange of Girders 3 and 4 at each girder's midspan. Two more gauges were installed at the west end of Girder 3, in a similar arrangement as the gauges at midspan. These two gauges were used to assess the amount of fixity occurring at the bearings. Figure 2.3 previously showed the girder numbering convention and orientation of the bridge.

During the test the triaxle truck drove over the bridge three times, moving from west to east, at an average speed of 5 mph. On Pass 1, the truck drove adjacent to the south curb and on Pass 3 the truck drove adjacent to the north curb. Pass 2 was completed by driving the truck along the roadway centerline. At the back tires, the average weight was 12.33 kips and at the front tires, the average weight was 7.92 kips.

2.3.2 Diagnostic Test Summary

Graphs were constructed of the recorded strain vs. time (or strain time history) during each pass to better evaluate the results from the bridge test. The

maximum strain recorded during the test was 60.9 microstrains. This value occurred during Pass 1 on the bottom flange of Girder 2. The time history graphs also proved that the parapets on either side of the bridge provided additional strength to Girders 1 and 4. This was concluded based on the lower strain values on the exterior girders compared to the interior girders. Even though the truck drove across opposite sides of the bridge during Passes 1 and 3, due to the skew of Bridge 7R, the peak strains in Pass 1 and Pass 3 were not mirror opposites of one another. However, from pass to pass the distribution of load between each girder was consistent with expectations in that when the load was over a particular girder, more loads were distributed to that girder.

2.3.3 Diagnostic Test and FEA Comparison

The FEA was compared to the diagnostic test by examining the strains in the girders, the transverse distribution of load between girders, and determining the neutral axis location of the girders. The strains during each pass were compared by examining the strain readings of the two highest strained girders per pass. For example, Girders 3 and 4 were evaluated during Pass 3 of the test. The FEM was loaded with static truck loads at different longitudinal increments on the bridge. Graphs of the strain readings vs. truck load locations on the bridge were then produced to compare the field test data and model. The results from the graphs showed good correlation, with the expectation of Girder 4 during Pass 3. The FEA predicted considerably more strain in Girder 4 than was recorded during testing. It was hypothesized that the fixity near the supports of Girder 4 may have caused the strains to reduce at the girder.

The transverse distribution of loads during each pass was another method of validating the FEM. Both the model and diagnostic test distribution factors were calculated by dividing the strain of a particular girder by the sum of strain values at all four girders. The distribution factors for each girder were calculated using the strain values for all girders during the pass and time causing the max strain in the girder of interest. The distribution factors between the FEA and test were in good correlation. However, similar to the midspan strain values, the FEA predicted a higher distribution factor for Girder 4.

An approximate location of the neutral axis was determined by using the strain gauges that were attached to the top and bottom flanges of Girders 3 and 4. As expected, the top flanges of the girders had low strain values that were in compression and the bottom flanges of the girders had strain values that were in tension. From the diagnostic test, the estimated neutral axis location at Girder 3 was 54.5 in. and was 55.7 in. at Girder 4; both of these locations are measured from the bottom of the bottom flange. Ross concluded that these values were close to the calculated theoretical neutral axis locations.

2.4   1/5TH-Scale-on-Steel Girder Bridge Test

The scaled bridge test took place during the beginning of 2008. The objective of the test was to test the ultimate capacity of the bridge as a system while observing the transverse moment redistribution of a bridge of similar scale to the destructive bridge test. Since destructive bridge tests do not occur often and the delay of the full-scale destructive bridge test was prolonged, it was of interest to also compare a FEA with the results obtained from the scaled bridge test. It is not often where a scaled

14

model of the FEA can be used to examine the inelastic response of a bridge before the actual bridge test. Therefore, it is important to learn from this unique opportunity of examining a structure as a system inelasticity though the FEM.

2.4.1   1/5th-Scale Slab-on-Steel Girder Bridge Specimen Design

Dimensional analysis and the Buckingham Pi Theorem (Buckingham, 1914) was used to replicate a full-scale model of Bridge 7R at 1/5th scale as close as possible while also fitting within the space limitations of the laboratory. This meant that the skew assumed in the scaling process was 25 degrees and a new prototype bridge was designed based on this level of skew. Every physical quantity (geometry, the loading applied on the bridge and etc.) of the bridge was then scaled by the Pi terms (with the exception of the dead load, which was not influential to the test results) to obtain the 1/5th-scale specimen. The Pi terms also scaled the properties (yield moment, plastic moment, etc.) of the individual structural members of the bridge. The members were designed using the 2004 AASHTO Load and Resistance Factor Design (LFRD) Bridge Design Specifications (2007) for the girders and Steel Construction Manual (AISC, 2005) for the cross frames.

The result of this design and scaling process was that the scaled bridge girders were constructed of M12x11.8 rolled steel beams. The four beams were 19 ft in length and spaced 11.6 in. on center. The beams are also fully composite with the 2 in. deck, which are connected using 24 shear studs per beam.

2.4.2   1/5th-Scale Slab-on-Steel Girder Bridge Test Procedures

The loading schemes for the bridge were scaled to simulate one scaled AASHTO HS-20 design truck per loading increment. Three hydraulic jacks were used to

add loading and pauses in loading throughout the test to allow the loads to transfer throughout the entire structure and instrumentation readings to stabilize. The jacks were centered over one of the interior girders, where each axle of the truck acted as a single point load. This was done with the intent to avoid a direct shear failure of the concrete deck and allow for redistribution of the loads to be able to be more easily observed. The scaled truck axles are spaced 2.8 feet apart with the front axle applying 320 lbs of load per increment and each of the two back axles applying 1280 lbs of load per increment. Eighteen (18) strain gauges were installed on each girder, for a total of 64 strains gauges.

2.4.3   1/5th-Scale Slab-on-Steel Girder Bridge Test Summary

As expected, the first sign of yielding in the bridge occurred at the bottom flange of the girder that was directly under the applied loads. The yielding occurred at 12 scaled trucks. The yielding reached the middle of the web as the loads surpassed 19 scaled trucks. The ultimate load for the structure was 22 scaled trucks and the governing failure mode was extensive longitudinal cracking of the concrete deck of the bridge. At this loading, only 30% of the four-girder cross-section at midspan has yielded.

The most significant conclusion found as a result of the FEA of the scaled bridge test is that modeling the concrete deck properly is the key in order to replicate the inelastic response of the bridge. Since the deck was the main load transfer mechanism between the girders (the specimen was designed to prevent load transfer through bending of the cross-frames to simplify interpretation of the test results), it must be accurately modeled so that the girders experience similar load distribution. The cracking of the concrete during truck increments 12-22 decreased the transverse load distribution between the girders, thus applying additional loading onto the girder that had the loading

16

directly above it. Due to this cracking and the resulting change in stiffness of the model, a FEA using explicit analysis was used. This analysis accounts for the cracking of the concrete and therefore reduces the moduli of the deck as the deck begins to crack (at higher loads). Using the explicit model in the FEA, an accurate representation of the scaled bridge test was achieved.

Chapter 3

LOADING METHODS

3.1   Loading Process

In order to replicate the testing in the FEA, a precise method of loading the

structure was necessary to have accurate input for the model and be able to correlate

results between the field test and FEA. The method of loading the structure was also

selected to maximize the moment applied to the girders of the bridge. Thus, the design

firm HNTB (the Engineer of Record for the larger realignment project) designed a

loading mechanism that would apply concentrated loadings onto the bridge in increments.

Each increment represents one AASHTO HS-20 vehicle, which has front wheel weights

of 4 kips and back wheel weights of 16 kips, for a total weight of 72 kips. The front axle

of the loading mechanism (which will be explained in more detail in Section 3.3) is to the

right of Figure 3.1 and the back axles are to the left of this.

A total of seventeen load increments were applied to the bridge, totaling

1224 kips of applied load and creating an HS-340 design truck. A conversion between

the hydraulic jack pressure and loads was used to approximate the desired loading at each

jack during each increment. The loading was applied using two hydraulic systems. One

system applied the front axle loadings and the other system applied the back axle

loadings. After both systems were jacked at each increment, loading was momentarily

paused to allow loads to stabilize. The loading sequences between the two jacking
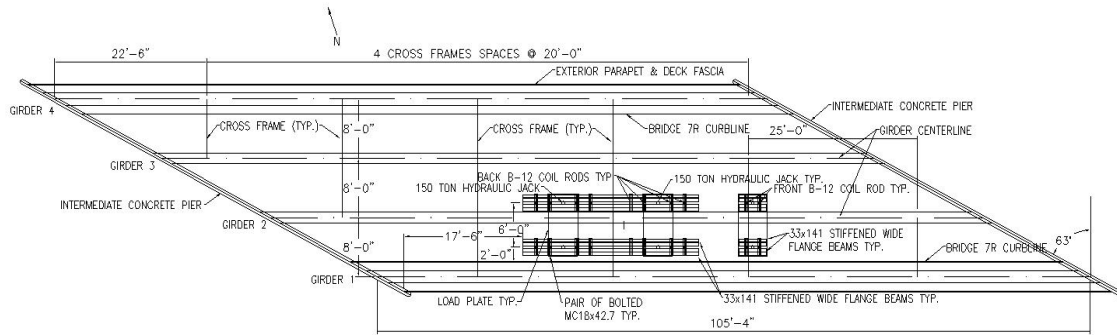
Figure 3.1   Plan Views of Bridge and Loading Mechanism

systems were not jacked simultaneously. Therefore, prior to load stabilization during each loading increment, there is some sensitivity in the data based on the gauge's location relative to the jacking system. This is discussed in more detail in Section 4.2, where a thorough discussion of the bridge's strain response is presented.

3.2   Loading Mechanism Location

The location and orientation of the loading mechanism was positioned to induce the maximum localized force effect possible onto Bridge 7R. Figure 3.1 shows this position. The loading mechanism is located 2 ft transversely from the edge of the bridge's south curb and 17.5 ft longitudinally from the southeast corner of the bridge.

This transverse distance was based on the extreme of the wheel line placement currently specified in the AASHTO LRFD Bridge Design Specifications (2010). The 2 ft transverse distance, positioned one of the loading mechanism's line of jacks between Girders 1 and 2. The other line of jacks is located in between Girders 2 and 3. See Figure 3.1 for reference. By transversely locating the loading as close to one side of the bridge as possible, this will maximize the opportunities to observe load

redistribution after girder yielding. This will allow greater stresses on Girder 2 and minimize the force required to produce yielding in this girder, which is a critical consideration in designing the loading mechanism.

The longitudinal positioning of the loading mechanism maximizes the flexural moment in Girder 2. The orientation (the front axle on the east versus west side of the bridge) was determined based on FEA that showed that this orientation increased the transverse redistribution of moment from Girder 2. More information about the orientation of the loading mechanism can be found in Ross (2007).

3.3   Loading Mechanism Physical Description

A plan view of the loading mechanism was previously shown in Figure 3.1, while a cross-section view is shown in Figure 3.2 and a photo of the above-deck portion of the loading mechanism is shown in Figure 3.3. These show the key components of the loading mechanism, which are the six hydraulic jacks, four pairs of stiffened W33x141 wide flange beams, and twenty coil rods that are placed vertically through holes drilled in the bridge deck. As seen in the figures, the load from the jacks is first resisted by the pairs of stiffened beams, which are in turn restrained by the coil rods that are embedded in concrete and backfill beneath the bridge. Some additional components of the loading mechanism include: steel load plates placed on top of the bridge deck under each pair of jacks representing a single axle to minimize local stresses on the surface of the deck; pairs of MC18x42.7 placed on top of the stiffened beams; and additional steel channels at both ends of each pair of stiffened beams so that none of the structural members rested on the hydraulic jacks at the onset of the test. Figure 3.4 displays a close up of the lower part of the above-deck portion of the loading mechanism.
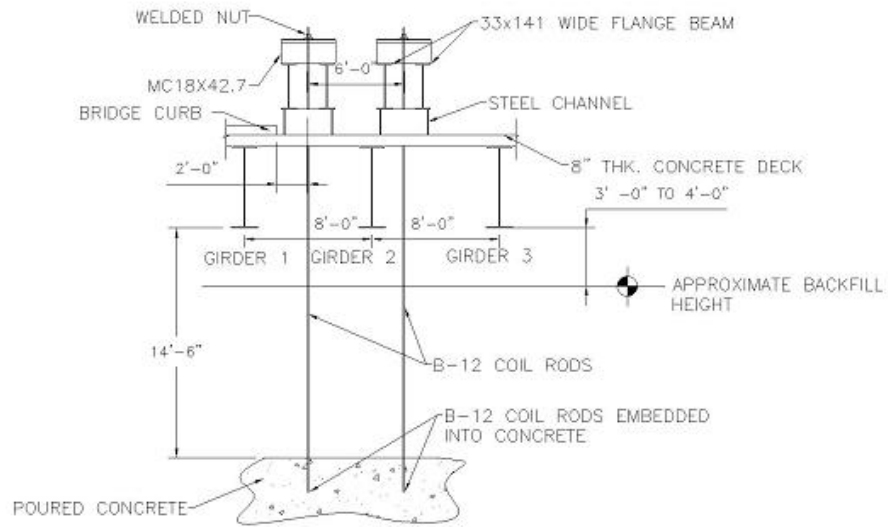
Figure 3.2   Cross-Section View of Loading Mechanism

Figure 3.3   Photo of Loading Mechanism, Side View

21

Figure 3.4   Photo of Loading Mechanism from Bridge Deck

Holes of 3 in. diameter were drilled through the concrete deck and load plate (where applicable) to allow the passage of the 1 1/2 in. diameter B-12 Dayton Richmond coil rods that passed through the bridge deck. The coil rods passed between the two stiffened wide flange beams and the two MC18x42.7, which were bolted to one another. At the top of each MC18x42.7 pair, the coil rods also passed through a steel plate with a hole drilled through its middle to allow the coil rods through. A nut was tightened against this plate. Welds were placed between: the plate and MC18x42.7 pair, the plate and nut, as well as the nut and B-12 coil rod. Whether this was necessary or advisable or not was a source of debate between the project participants. Figure 3.5 shows one of the twenty coil rod and bolt connections.

22

As shown in Figure 3.2, the B-12 rods were first vertically embedded into concrete, 14.5 ft below the bridge, where Baylor Boulevard formerly crossed under the bridge. The coil rods were not long enough to reach the necessary height above the bridge deck. Therefore, each B-12 coil rod was individually spliced onto additional coil rods using Dayton Superior's D-110 US/MC-SAE coupler splice system. Before the bottom coil rods were spliced to the additional coil rods, the bottom coil rods were nearly covered to the top with backfill. More back fill was used to cover the next set of coil rods and then spliced together with additional coil rods. The process continued until the backfill reached approximately 3-4 ft. away from the bottom of the bridge and the coil rods were approximately 5-6 ft. above the bridge deck. Figure 3.6 displays a photo of the structure (looking north), where the backfill height and coil rods below the bridge can be seen.
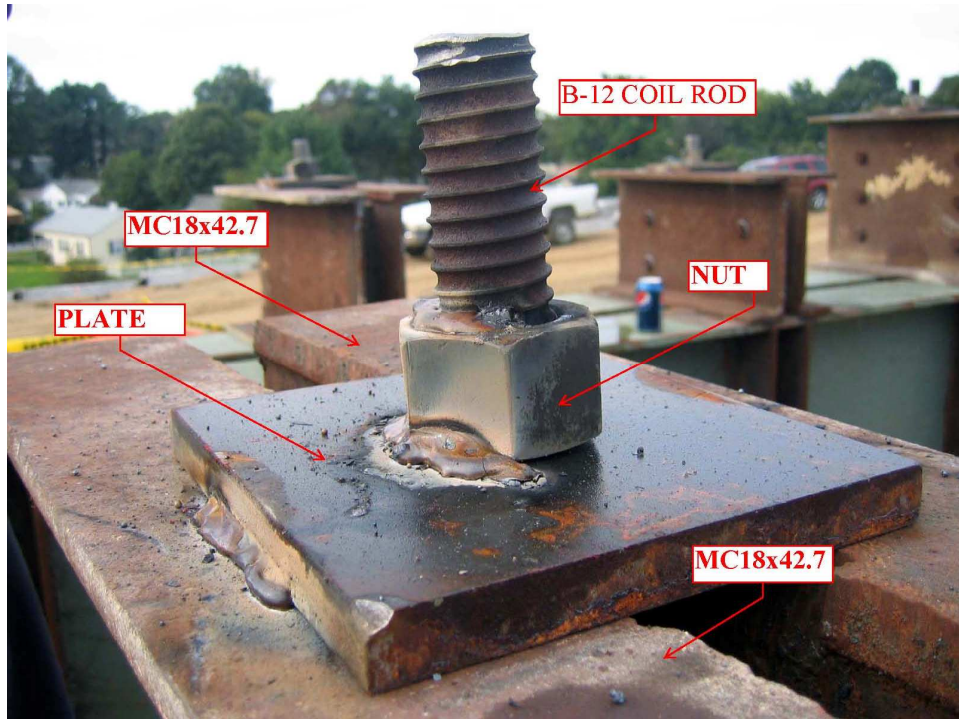
Figure 3.5   Close Up Photo of Coil Rod on Loading Mechanism

Figure 3.6   Photo of Bridge 7R, Facing North

Figure 3.7 displays a plan view of an HS-20 truck (at the top portion of the figure) and the loading mechanism that was used during the bridge test (at the bottom portion of the figure). As shown in the figure, the dimensions of the truck and loading mechanism are the same. The HS-20 truck transverse distance between wheels is 6 ft. and the longitudinal distances between each axle are a minimum of 14 ft, which would cause the worst-case scenario for the subject structure. The transverse distance between the centerline of the hydraulic jacks was 6 ft. and the longitudinal distance between the hydraulic jacks were 14 ft. The use of four coil rods at each back wheel location was based on the amount needed to resist HS-20 load increments. The load at each front wheel location is resisted by two coil rods in order to resist the force from the jack symmetrically, despite the fact that only one rod would be needed based on the anticipated forces.
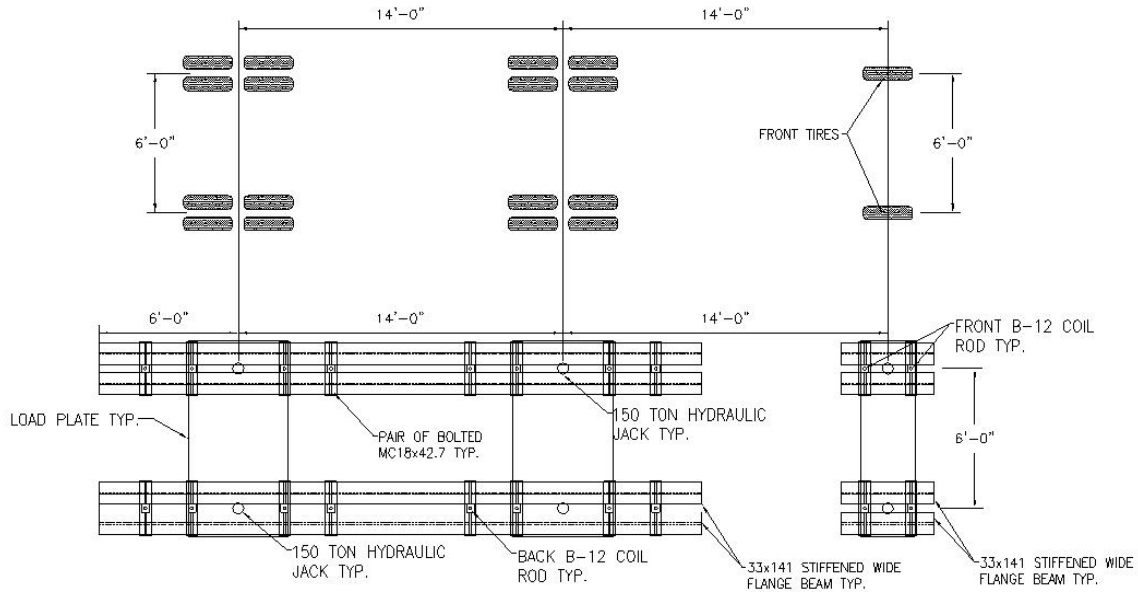
Figure 3.7   Plain Views of HS-20 Truck and Loading Mechanism

3.4   Bridge 7R Capacity Predicted by AASHTO (2010)

It was a primary objective of this work to compare the field data and FEA with the current design standards (AASHTO 2010) to understand the reverse capacity of Bridge 7R relative to these standards. The capacity calculations from the design standards will be shown and explained in this section. This includes both girder capacity, which is directly given in AASHTO, and the ultimate system capacity, which is not directly specified. The ultimate capacity results from the FEA will be discussed later in Sections 5.3 and 5.4.

While AASHTO does not explicitly quantify a system-level capacity, one reasonable way of this value could be quantified is the number of AASHTO HS-20 vehicles necessary to cause an applied moment great enough to cause flexural yielding

25

equal to the nominal moment capacity in each of the four girders (which is M_y for this case). Another more extreme metric would be the number of AASHTO HS-20 vehicles necessary to cause an applied moment equal to the plastic moment capacity in each of the four girders. Because all girders do not initially share equally in resisting the applied load, these calculations assume that once the moment capacity is achieved in a given girder, it continues to resist this level of moment, but any additional moment is redistributed to the remaining girders that have not achieved their moment capacity. Ross (2007) has shown that this is equal to summing the moment capacity of all of the girders in the cross-section. Dividing the system-level capacity by the moment produced by a HS-20 vehicle (M_{truck}) will give the number of trucks causing the AASHTO system-level capacity.

Section 3.4.1 first quantifies the girder capacity in terms of HS-20 trucks. Section 3.4.2 then presents the calculations for the system-capacity (again in terms of HS-20 trucks) of Bridge 7R by using the moment that was produced by the loading mechanism and neglecting load and impact factors in the calculations (or, in other words, assuming these factors equal 1.00). Thus, these calculations remove the conservatism inherent to design codes and are meant to serve as a basis for comparison to the actual test results, where the load is known with relative certainty. Because the girder capacity per AASHTO of these slender web girders is M_y, this will be referred to as the yield moment system-capacity. The capacity based on all girders achieving M_p is also given in this section to provide an upper-bound of system capacity. Section 3.4.3 calculates the system-capacity and associated number of trucks in a similar manner but uses the worst-

case truck moments as well as AASHTO load and impact factors. The result of these calculations is termed the AASTHO system-level capacity.

3.4.1   Girder Capacity

Based on the longitudinal positioning of the loading mechanism relative to Girder 2, the moment produced during each increment of loading (as a result of concentrated axle loads of 32k, 32k, and 8k spaced at 14 ft) was calculated to be 1,616 ft-kips (or 19,392 in.-kips, not including the load or impact factor). This value will be compared to the sum of the yield moments of each girder to determine the yield moment system capacity in terms of number of HS-20 vehicles.

The yield moment of the girders was calculated using Equation 3.1.

$$\sigma_y = \frac{M_{D1}}{S_{NC}} + \frac{M_{D2}}{S_{LT}} + \frac{M_{AD}}{S_{ST}} \tag{3.1}$$

Here σ_y is the yield strength of the governing (bottom) flange, which was taken as 36 ksi. It should be recalled that the actual minimum specified yield strength of the girders is 33 ksi, but is taken as 36 ksi for consistency with the FEA and to account for the fact that the actual yield strength is most likely greater than the minimum specified yield strength.

M_{D1} is the moment that is produced by the dead loads of the concrete deck, cross frames, and girders. For the interior girders (Girders 2 and 3) the unfactored M_{D1} is 19,154 in.-kips. For the exterior girders (Girder 1 and 4) the unfactored M_{D1} is 16,875 in.-kips. Including a dead load factor of 1.25 gives the factored dead load capacity (M_{D1}) for both the interior and exterior girders of 23,943 in.-kips and 21,087 in.-kips respectively. In these calculations the unit weight of steel is taken as 490 lb/ft³, the unit weight of concrete is taken as 150 lb/ft³, the actual girder area is used, the concrete

27

effective widths are used to determine the distribution of the concrete weight, and the weight of the cross-frames and miscellaneous steel distributed to each girder is taken as 10% of the girder weight. M_{D2} is the moment that is produced by the dead load of the concrete parapets. Since the parapets were removed before testing, M_{D2} is taken as zero.

The denominators in Equation 3.1 represent the section modulus of the girder under various composite action conditions. S_{NC} is the section modulus of only the steel girder; S_{LT} is the long term section modulus; and S_{ST} is the short term section modulus. For the interior girders these values are 2,813 in.-kips, 3,494 in.-kips; 3,700 in.-kips, respectively. The corresponding values for the exterior girders are 3,467 in.-kips, 4,135 in.-kips; 4,420 in.-kips.

Substituting the above unfactored values into Equation 3.1, gives M_{AD} equal to 9,000 ft-kips for the interior girders and M_{AD} equal to 11,467 ft-kips for the exterior girders. Substituting the above factored values into Equation 3.1, gives M_{AD} equal to 8,476 ft-kips for the interior girders and M_{AD} equal to 11,020 ft-kips for the exterior girders.

Due to the placement of the loading mechanism, Girder 2 will be the first girder to experience flexural yielding. Therefore, the girder capacity results are based on the interior girder capacity. Using the unfactored live load moment interior girder moment of 9,000 ft-kips and dividing by the product of the moment produced by a single truck (1,616 ft-kips) and the AASHTO load distribution factor of 0.476, gives an actual girder capacity (discounting load factors) of 12 trucks.

The girder capacity of 12 trucks neglects the conservatism that would result from using the AASHTO specifications in two ways. First, the truck moment is not

based on the exact longitudinal position causing the greatest moment. Secondly, the load and impact factors are neglected. By changing the longitudinal positioning to produce the maximum moment (1,620 ft-kips) in Bridge 7R and including a distribution factor of 0.476, live load factor of 1.75 and impact factor of 1.33 , the maximum moment was calculated to be 1,795 ft-kips per truck. Dividing the factored interior girder live load moment capacity (M_{AD} = 8,476 ft-kips) by the moment induced by a single truck gives an AASHTO girder capacity of 5 HS-20 trucks.

3.4.2 Yield Moment System Capacity

As discussed above, the yield moment system capacity represents the sum of the yield moments of each girder (based on assuming redistribution of load once an individual girder reaches its yield moment) expressed in terms of number of HS-20 vehicles. The live load capacity of the structure is then the sum of the M_{AD} values for each girder shown in the previous section $\left(\sum_{1}^{n=4} M_{AD} \right)$, which totals 40,934 ft-kips. Dividing this capacity by the moment produced by a single truck in the position of the loading mechanism (1,616 ft-kips) gives the yield moment system capacity of the bridge (discounting load factors) to be 25.3 HS-20 trucks.

The same calculations were performed based on a girder capacity of M_p (versus M_y) to give an upper bound of the system capacity that may be obtained. To do this, M_p of the interior girder was calculated to be 13,209 ft-kips and M_p of the exterior girder was calculated to be 15,924 ft-kips. The dead loads carried by each interior girder (1,596 ft-kips) and exterior girder (1,406 ft-kips) were subtracted from these capacities. The sum of the remaining capacity of each girder was then calculated as 52,252 ft-kips.

29

Dividing this value by the 1,616 ft-kips generated by a single truck gives the plastic

moment system capacity of the bridge to be 32.34 HS-20 trucks.

3.4.3 AASHTO System Capacity

While the capacities of 25 and 32 trucks computed in the previous section

will be later used to compare to the actual bridge performance, a value based on the

AASHTO specifications was also calculated that included the positioning to induce the

greatest moment as well as load and impact factors. This is done in order to understand

the system capacity that would result from using the conservatism inherent to the

AASHTO specifications. The factored live load capacities (M_{AD}) that were calculated in

Section 3.4.1 of 8,476 ft-kips and 11,019 ft-kips for the interior and exterior girders,

respectively, was totaled for a live load capacity for the structure $\left(\sum_{1}^{n=4} M_{AD}\right)$ of 38,990

ft-kips. Dividing this value by the 3,771 ft-kips generated per factored truck gives the

AASHTO system level capacity as 10.3 trucks. Comparing this capacity of 10.3 trucks to

the 25.3 trucks calculated in the previous section shows that the AASHTO load factors

significantly reduce the predicted capacity of the structure (by more than half in this

case). These system capacities will be compared to the field test and FEA results in

Section 6.2.

Chapter 4

FIELD TEST RESULTS

4.1 Instrumentation Layout

The destructive testing instrumentation layout included a total of sixty-eight strain gauges. Six of the gauges were attached to the B-12 coil rods that were part of the loading mechanism. These gauges were used to quantify the applied loading. The remaining sixty-two gauges were attached to the bridge girders and cross-frames to observe the response of the bridge during testing. The instrumentation plan was developed using the FEA of the bridge to determine the critical areas of the bridge that should be examined during testing.

The strain gauges were connected to two data acquisition systems; a MicroMeasurements System 4000 and a System 5000. During the 14th load increment of the test, a power outage shut down the data acquisition systems. After the data acquisition systems rebooted it was determined that the load must be removed from the bridge and the test repeated because it was not going to be possible to otherwise correlate the results from before and after the power outage. When the test was repeated, unfortunately, the System 4000 did not retain strain readings from the second bridge test. A total of thirty-three strain gauge readings were retained from the System 5000. Fortunately, that was enough data to compare the actual response of the bridge with the

FEA. Five of the retained strain gauges were attached to the B-12 coil rods. The remaining twenty-eight gauges were attached to the bridge's girders and cross frames.

Figure 4.1 displays the location and labels of the strain gauges that were attached to the coil rods on the loading mechanism. The strain gauges labeled X1 and X4 represent gauges that were attached to the coil rods corresponding to the jacks representing the lighter front axle of the HS-20 vehicle, which will be denoted as the front bars. Strain gauges labeled X2, X3, X5, and X6 represent gauges that were attached to the coil rods corresponding to the jacks representing the heavier back axles of the HS-20 vehicle, which will be denoted as the back bars. Of the six bars, only the data from gages X1 through X5 was retained. This is indicated visually in Figure 4.1 by representing these locations with solid dark squares, while X6 is represented by a solid dark circle.

The strain gauges on the bridge were located at several different girder cross-sections and on several cross frames. Each of these locations is termed a "gauge grouping" and Figure 4.2 displays the labels and locations of these strain gauge groupings on the bridge. As was also done in Figure 4.1, the solid dark squares indicate a location where the strain gauge data was retained during testing while the solid dark circles indicates a location where the strain gauge data was not retained during testing. Additionally, the bottom flange strain data at gauge grouping G2-B was manually recorded at discrete time stamps during testing. This data is included in Appendix A for completeness although it was not ultimately used in this work since the time stamps for this data set do not correspond to the time stamps ultimately selected for data evaluation (which are described in the following section). The large asterisk near the midspan of

32
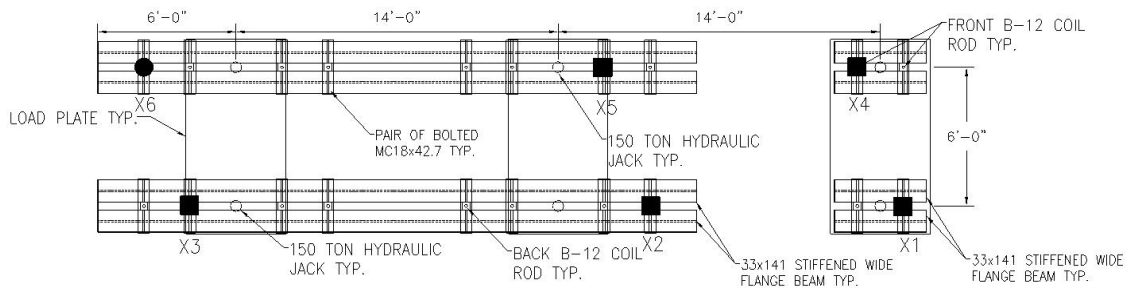
Figure 4.1   Coil Rods Strain Gauge Locations
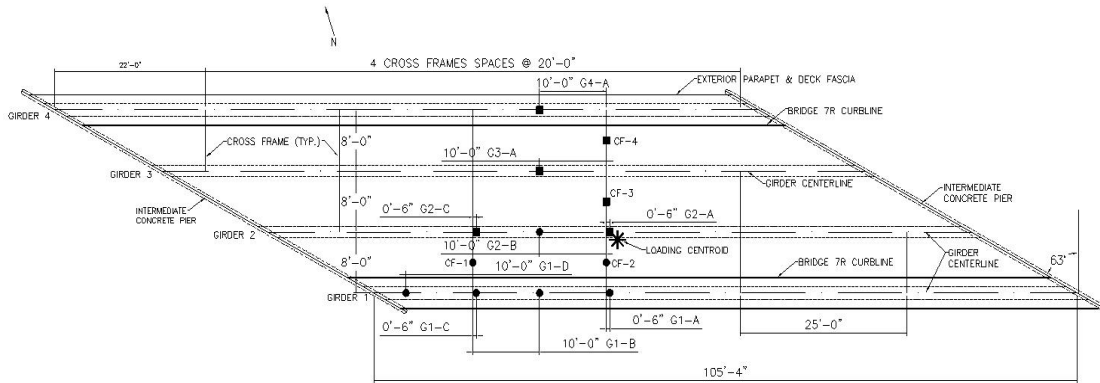
Figure 4.2   Gauge Grouping Locations

Gauge Grouping	Direct Distance
G2-A	1'-7"
G2-C	21'-3"
G3-A	14'-10"
G4-A	20'-9"

Table 4.1   Distances between Girder Gauge Groupings and Centroid of Loading

Girder 2 in the figure indicates the location of the loading centroid. Distances between the loading centroid and the gauge groupings are given in Table 4.1.

Figure 4.3 displays (via the square symbols) the locations of each individual gauge within each of the nine gauge groupings on the girders. The view shown in the figure is from the perspective of looking west, which corresponds to the left side of Figure 4.2. The labels of the strain gauges reflect their location as follows. The first part of the label begins with the letter "G" followed by a number denoting the girder number on which the gauge was located. The second part of the label abbreviates the location of the gauge on the girder cross-section with respect to the bottom flange, top flange, or web and indicates whether the gauge is on the south (1) or north (2) side of the girder. The last part of the label distinguishes the longitudinal position on the girder from other gauge groupings on the same girder. For example gauge G2-BF2-C is located on the north side of the bottom flange of Girder 2 in the third (C) gauge grouping (moving west to east).

Gauge groupings G1-B, G2-B, G3-A, and G4-A had a pair of gauges that were generally attached to the top of the bottom flanges' fascia, 2 in. away from the outer edges of the flanges. However, the south gauge in gauge grouping G1-B (Gauge G1-BF1-B) and the north gauge in gauge grouping G4-A (Gauge G4-BF2-A) are attached 2 in. away from the outer edge of the bottom fascia of the bottom flange. This was done in order to avoid potential damage to the gauges when the parapets were removed.

The remaining gauge groupings have three pairs of strain gauges, for a total of six per grouping. One pair of gauges in these groupings is located in a similar manner as previously mentioned, on top of the bottom flange fascia, 2 in. from each girder edge. However, the south gauges for Gauge G1-A (Gauge G1-BF1-A), G1-C (Gauge G1-BF1-

34
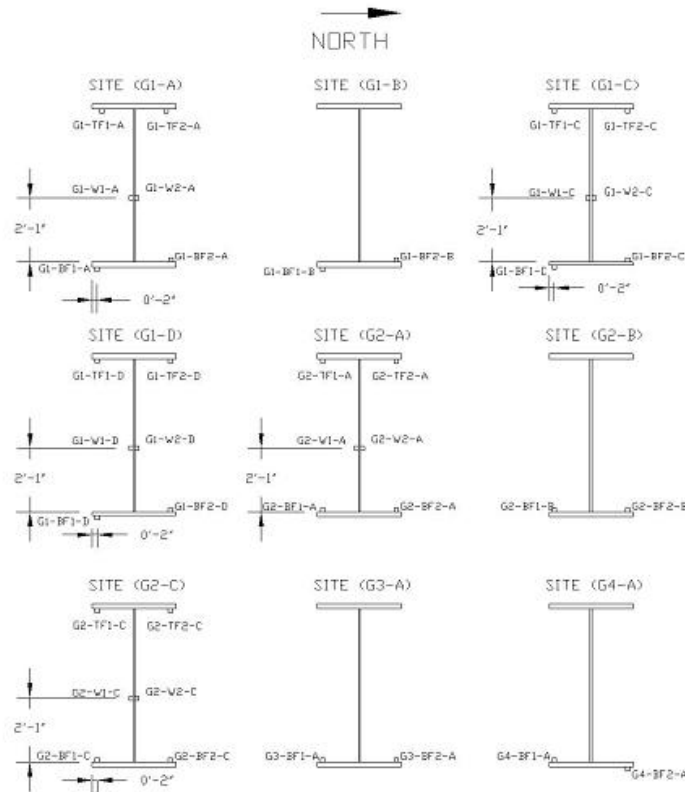
Figure 4.3   Girder Instrumentation Layout

C), and G1-D (Gauge G1-BF1-D) are attached on the bottom of the bottom flange fascia 2 in. from each girder edge. A second pair of gauges is attached to each side of the web, 25 in. from the top of the bottom flange. It was preferred to attach the gauges at the middle of the 60 in. deep web. However, this was not possible due to the presence of a longitudinal stiffener at mid-height of the exterior girders and the desire to have all the gauges attached at the same position. A third pair of gauges is located 2 in. away from each outer edge on the bottom fascia of the top flange.

Figure 4.4 displays (again via the square symbols) the locations of each individual gauge on the cross frames within the four gauge groupings on the cross frames previously identified in Figure 4.2. The view shown in the figure is once again from the

perspective of looking toward the west, which corresponds to the left side of Figure 4.2. The labeling convention of the cross frame gauges was similar to that of the girders. The first part of the label begins with the letter "CF" followed by a number denoting the gauge grouping number from Figure 4.2. The second part of the label indicates which steel angle (bottom angle, middle angle, or top angle) and which leg of the angle the gauge is affixed to; a "1" means that the gauge was located at the bottom leg of the angle and a "2" means that the gauge was located on the top leg. The last part of the label is used to distinguish between gauges located on the south (A) and north (B) side of Cross Frame 2; all other cross frames have only one set of gauges per member and these all end with the "A" designation.

All the cross frame strain gauges were attached to the interior fascia of the steel angles. In situations where only one leg of an angle is instrumented, the gauge is affixed to the leg that is concentric with connection between that member and the girder. The gauges on the inclined and top chords are also located at midspan of the members. Such a location was also desirable for the bottom chords, but could not be achieved due to the connection at midspan of the member. Instead, the gauges on this chord were located at the quarter point that was closest to Girder 2 (where the load was concentrated), with the exception of the bottom chord gauges on Cross Frame 2, which had gauges at both quarter points.

Cross frame grouping CF-2 had the most strain gauges with five pairs, totaling ten gauges. This cross frame had the most strain gauges due to the fact that the FEA predicted this cross frame to have the greatest amount of stress compared to the other cross frames.
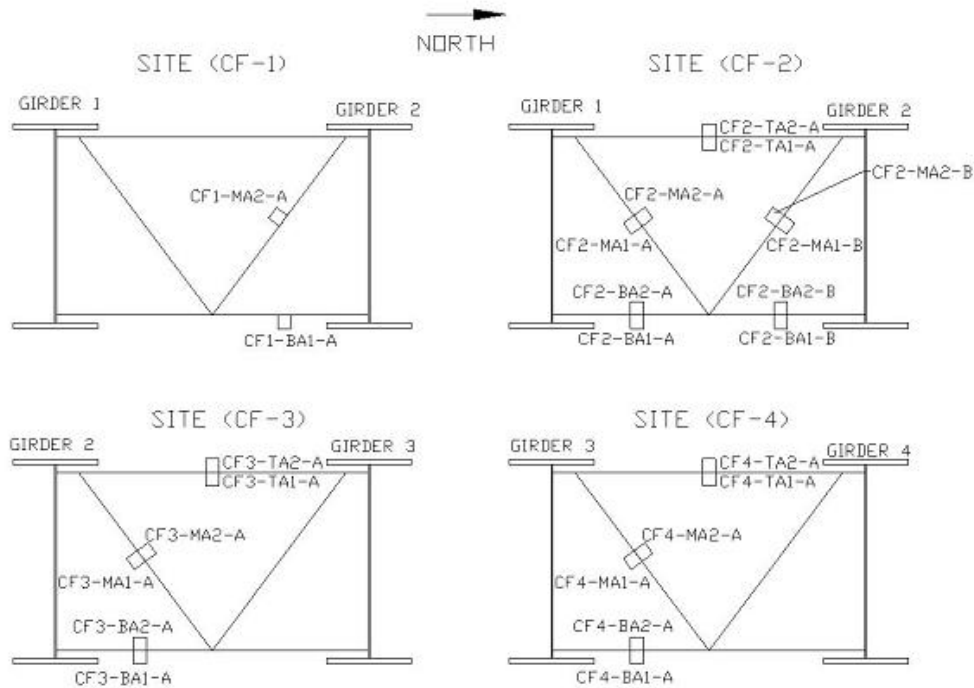
Figure 4.4   Cross Frame Instrumentation Layout

4.2   Field Test Load Data

The degree of accuracy achieved in applying the targeted loading magnitudes onto Bridge 7R cannot be known with absolute certainty, but this can be assessed to some degree by studying the strain gauge data from the gauges that were attached to the coil rods. This section explains the method in which the applied loadings were measured during testing and compared to the theoretical HS-20 truck loadings.

Figure 4.5 displays the microstrain vs. time (in seconds) graph from the coil rod gauges. The forces in the bars are also included, in the secondary y-axis of the figure. The recorded strains at the coil rods were converted to a force by multiplying the strain values to the elastic modulus and area of the bars.
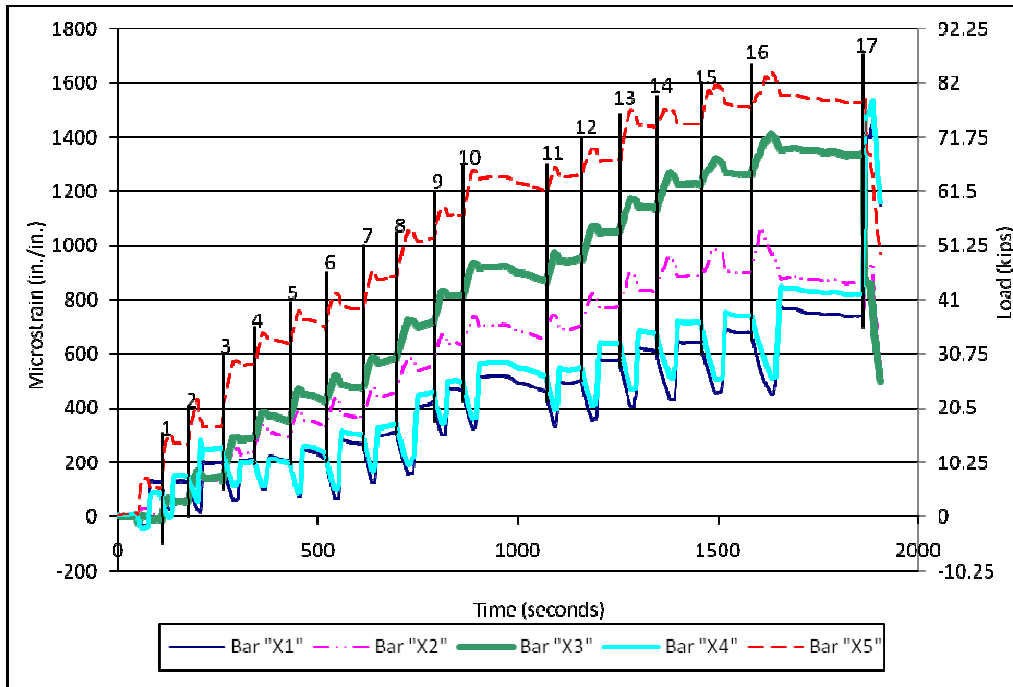
Figure 4.5   Coil Rods Time History Graph

The back bars (X2, X3, and X5) exhibit a similar pattern in the graph in that the strain values increase and decrease at the same times. Bar X5 experiences the highest strain values followed by Bar X3 and then Bar X2, throughout the graph. The fact that the Bar X5 and Bar X3 forces are higher than the X2 forces is expected as the former bars are closer to load jacks (see Figure 4.1). Also as expected, the back bars have higher strain values then the front bars (X1 and X4) since the jack force at the front bar locations is intended to be one-fourth that at the back bar locations, but half the number of coil rods exist at the front bar locations compared to the back bar locations. Not only do the front bars follow a similar pattern to one another, but the strain values of these two bars are closer to one another than any combination of the back bars.

The seventeen peaks on the graph represent the seventeen increments of loading that was applied to the structure. The vertical lines on the graph mark the end of

38

an increment with that increment number above. The end of an increment is defined by the last bar to finish plateauing on the graph, which was determined by looking at each increment in detail as described below.

Figures 4.6, 4.7, and 4.8 show these detailed graphs of increments 1, 2, and 3, respectively. Similar graphs of increments 4 through 17 can be found in Appendix B. The fact that the front and back bars were not jacked simultaneously during the test is evident in these graphs. Specifically, the back bars (X2, X3, and X5) were jacked first at every increment, which can be seen due to these strain values increasing first. These bars generally begin to increase due to the applied loadings at the beginning of each increment. The shift in the centroid of the loading that occurred between when the front and back bars were jacked caused the front bar strains to decrease at the start of each increment. However, later in each increment there is generally a net increase in force in these bars after the jacking force is applied to them.

After the jacking sequence is completed, the strains decrease and then plateaus as the load stabilizes (denoted at the horizontal portions on the graph). The end of an increment is defined as when a significant change in microstrain is observed in the data used to create Figure 4.5. Engineering judgment was used to determine what constituted a significant change based on the trends in the strain data in a specific gauge at a specific time; this corresponds to a difference of 4 to 13 microstrains from one time stamp to the next second at a given gauge. Time stamps are consistently used to report gauge readings for all gauges at the respective increments. The data was also evaluated to assess when significant changes in slope occurred; at the last time stamp for a given truck increment, the slope over the previous five seconds of data ranged between negative

39
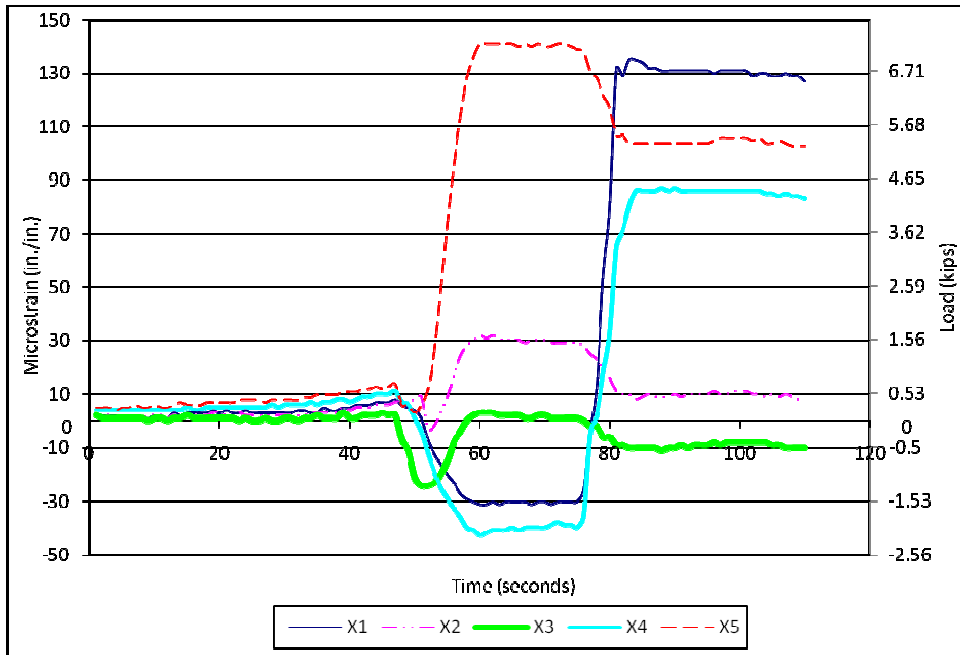
Figure 4.6   **Increment 1, Time History Graph**
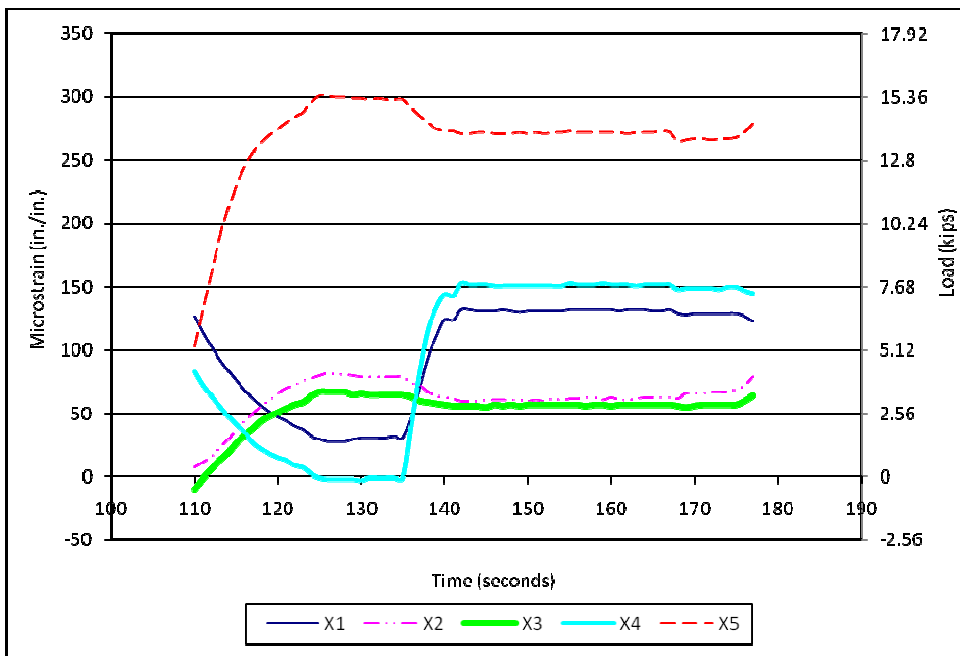
Figure 4.7   **Increment 2, Time History Graph**
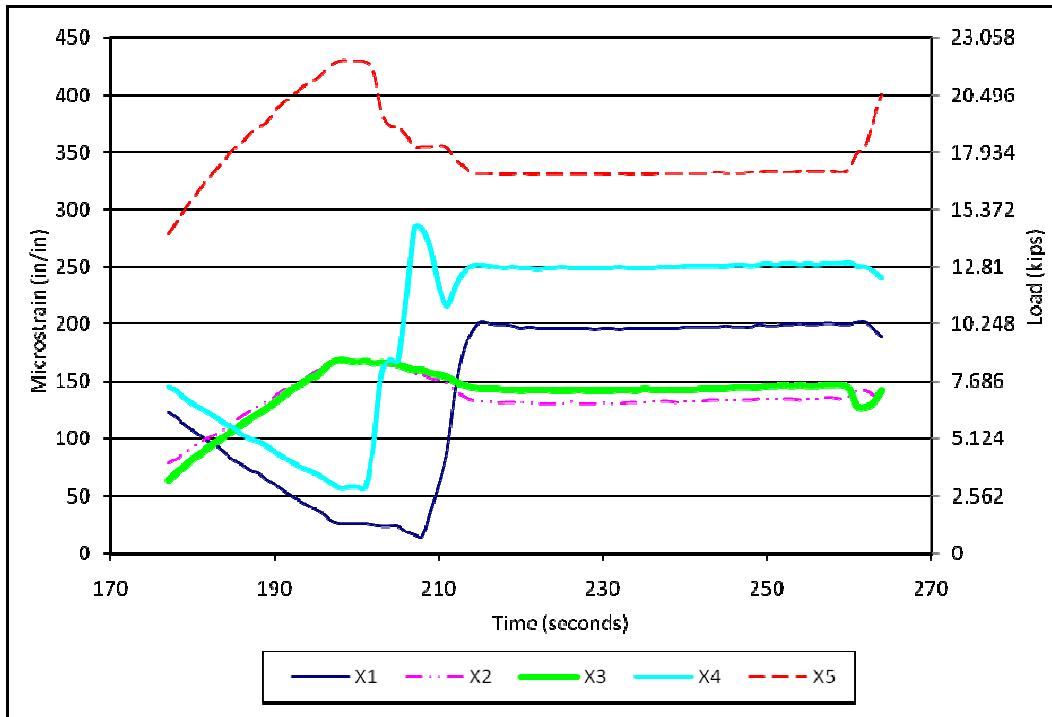
Figure 4.8   Increment 3, Time History Graph

0.2 and 4.6 for the governing bar and then becomes more significantly negative (steeper

slope) in the front bars as the next truck increment begins.

In all cases, the strain data for one of the two front bars (X1 or X4) was the

first to experience a significant change after the loading was applied, so this change

constituted the end of one increment and the beginning of the next. In all cases this

change was also a decrease in strain as loading was starting to be applied to the back bars.

Table 4.1 displays the time stamp corresponding to the end of each increment and these

time stamps are consistently used to report gauge readings for all gauges at the respective

increments.

The time stamps in Table 4.2 were used to create the graphs of strain (and

load) versus increment number in Figures 4.9 through 4.11. The graphs compare the five

41

coils rod forces to the theoretical HS-20 truck loadings that were targeted. Specifically,

Figure 4.9 compares the theoretical loading of 2 kips of force (or 39 microstrains) per

increment to the actual front coil rod forces. Figure 4.10 compares the theoretical loading

of 4 kips of force (or 78 microstrains) per increment to the actual back coil rod forces.

Figure 4.11 compares the total theoretical loadings of 16 kips of force (or 312

microstrains) per increment and total actual forces from two previous figures. The total

theoretical loading is the targeted sum of the five bars (two front bars and three back

bars) during each increment.

The forces in the coil rods show reasonable correlation with the targeted

theoretical loadings. The forces in the two instrumented front bars show the weakest

correlation and are higher than the targeted loadings by 30% on average. The

Increment	Time (seconds)
0	0
1	110
2	177
3	264
4	344
5	431
6	522
7	613
8	698
9	791
10	864
11	1072
12	1160
13	1254
14	1347
15	1459
16	1585
17	1841

Table 4.2   Time Stamp for each Increment
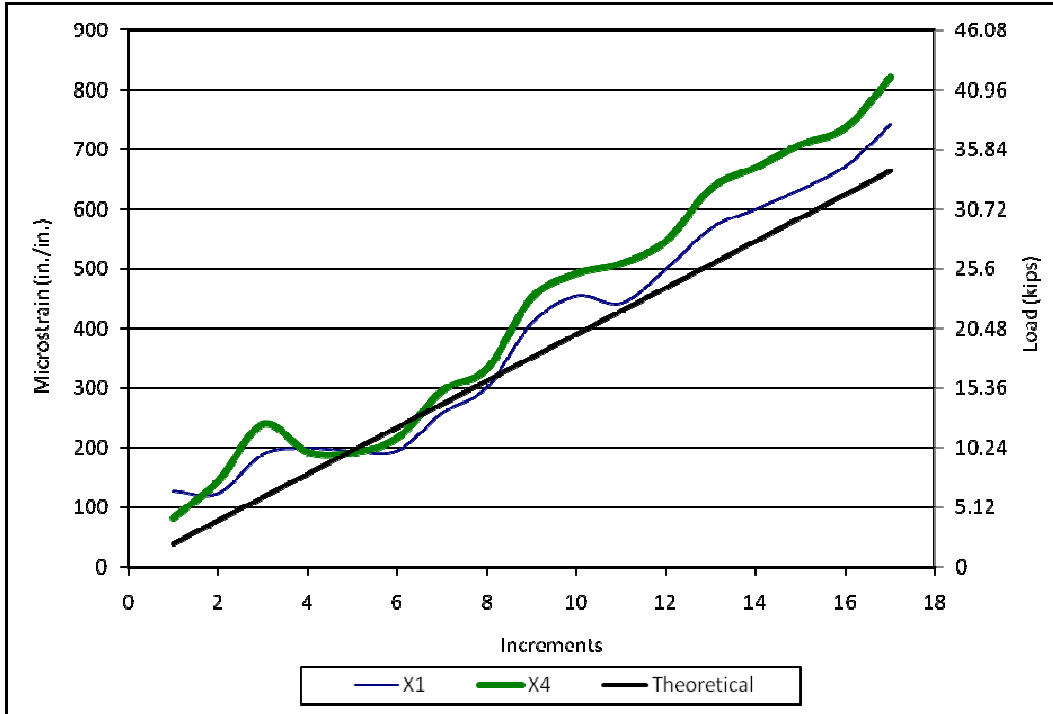
Figure 4.9   Theoretical vs. Actual Front Coil Rods
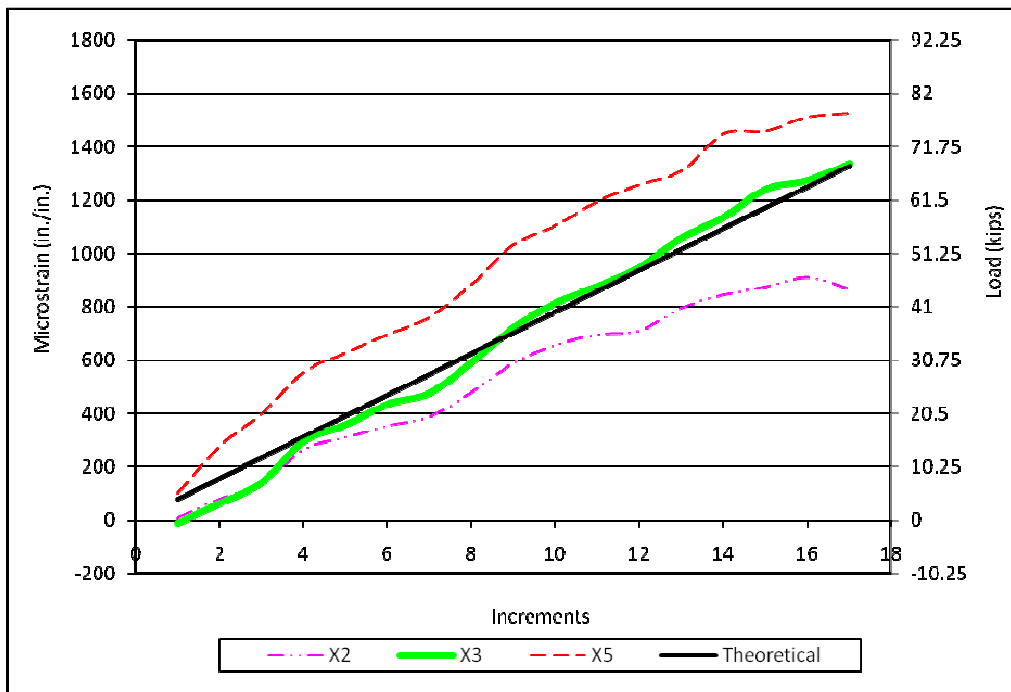
Figure 4.10   Theoretical vs. Actual Back Coil Rods

43
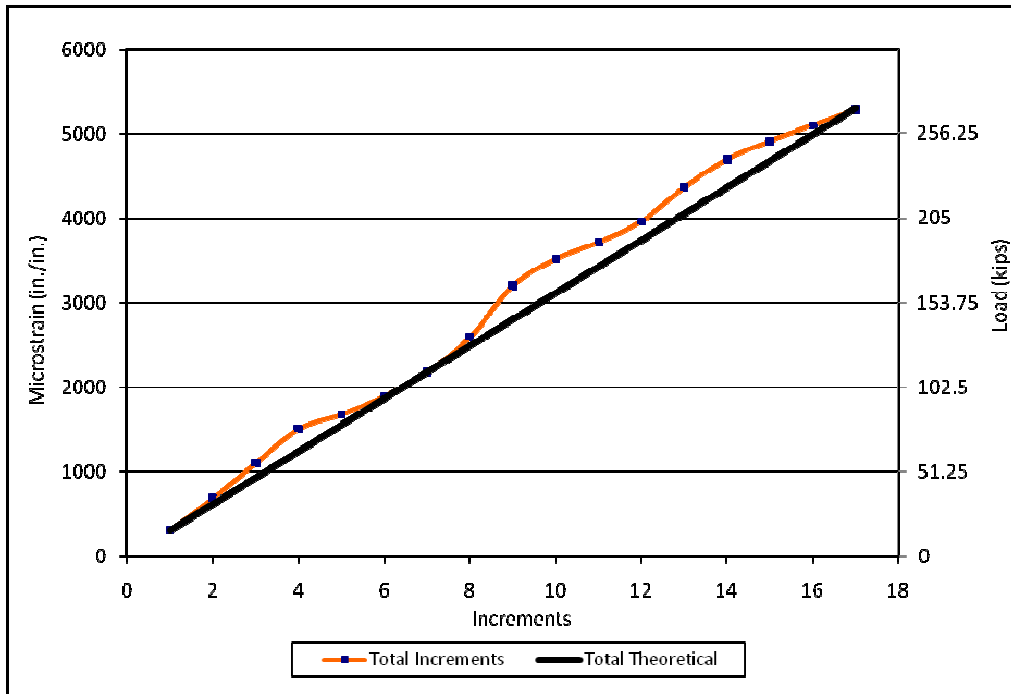
Figure 4.11   Theoretical vs. Actual Total Coil Rods

 instrumented back bars show much better correlation, differing from the targeted

loadings by only 10% on average. However, the average percent difference for the sum

of the five bars was very consistent with the theoretical loadings, differing by an average

of only 7%. The percent differences were calculated by taking the absolute difference

between the actual loads and theoretical loads, then dividing by the theoretical loads.

It may also be noteworthy that the strains plotted in Figure 4.9 show that

the strain is increasing very little in the front bars between increments 4 and 7, with

almost no increase between increments 4 and 6. This may have also played a role in the

issues related to the variable neutral axis position and changes in girder strain that were

observed during these increments that will be discussed in the following section.

4.3   Field Test Girder Data

4.3.1   Neutral Axis Evaluation

Gauge groupings G2-A and G2-C were the two groups (where data was retained) have strain gauges attached to the top flange, web, and bottom flange of the girder. Thus, the neutral axis location of the girder can be assessed at these two cross-sections. Figure 4.12 displays the cross-section strains from gauge grouping G2-A and Figure 4.13 displays cross-section strains from gauge grouping G2-C. Both graphs show the cross-sectional strains between increments 13 and 17, where relatively consistent neutral axis locations are observed. The neutral axis position during all increments will be subsequently discussed.

The cross-sectional strains in Figures 4.12 and 4.13 generally indicate an ideal elastic flexural response through the cross-section in that the strains at the top flange, web, and bottom flanges proportionately increase as more load is applied to the structure. Between increments 13 and 17 at gauge grouping G2-A (Figure 4.12), increment 13 had the lowest neutral axis location at 54 in. from the base of the bottom flange and increment 17 had the highest neutral axis location at 57 in. At gauge grouping G2-C (Figure 4.13), increment 17 had the lowest neutral axis location at 51 in. from the base of the bottom flange and increment 13 had the largest neutral axis location at 52 in. These neutral axis locations were quantified based on visually observing where the trend lines (generated using Microsoft Excel's smooth line feature) in the figures above crossed the vertical axis. As mentioned in Section 2.2.3, the estimated neutral axis location from the diagnostic test for the interior girders of the bridge was 54.4 in. from the base of the

45
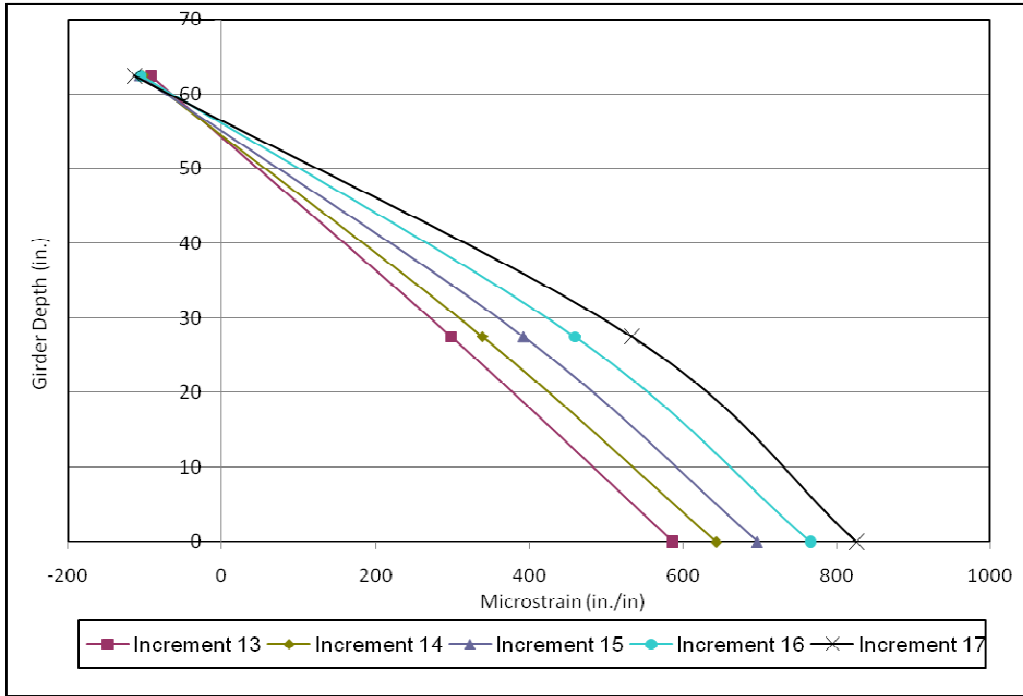
Figure 4.12   Gauge G2-A Cross-Section Strain Increments 13-17
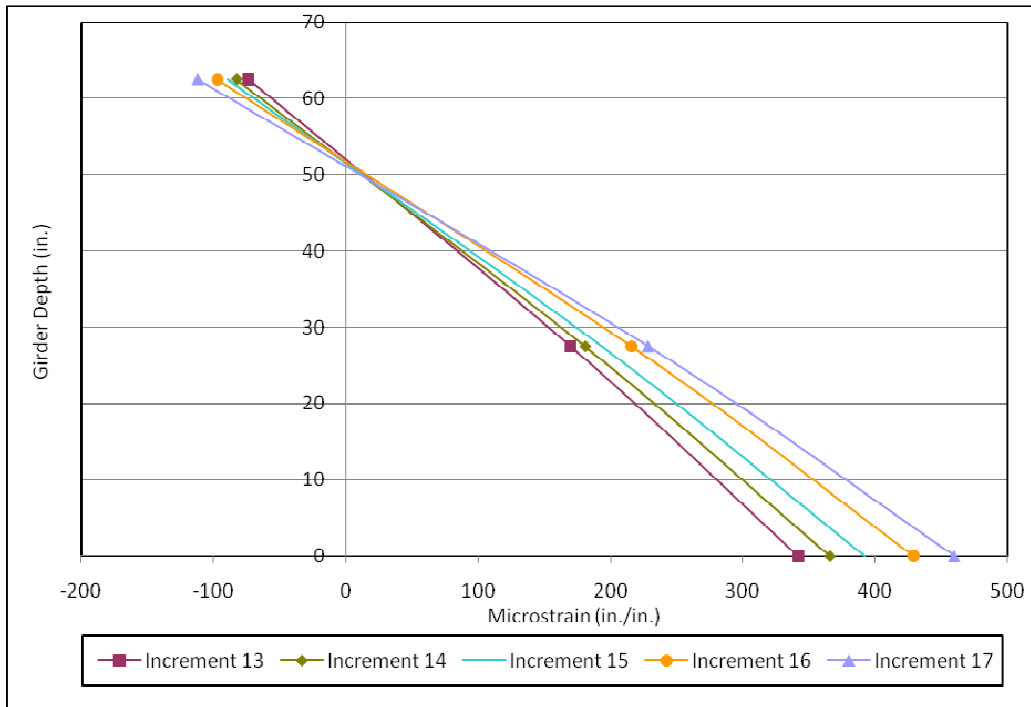
Figure 4.13   Gauge G2-C Cross-Section Strain Increments 13-17

46

bottom flange. The calculated value is 51 in. (based on the effective concrete width of 96 in., concrete density of 150 pcf, and concrete compressive strength of 9,000 psi). Thus, these results (particularly at G2-C) are generally consistent with expectations based on the previous predictions. The fact that the neutral axis is relatively high at gauge grouping G2-A at increment 17 suggests that the bottom flange may be beginning to yield at this location; this is also suggested when visually comparing the linearity of increment 16 versus 17 in Figure 4.12. This potential yielding is discussed in more detail in the following section.

Figures 4.14 and 4.15 are graphs of the cross-sectional strains between increments 1 through 6 and 7 through 12 (respectively) for gauge grouping G2-A. During increments 9 through 12 the neutral axis locations were all within 3 in. of the calculated value of 50.8 in. At increments 4, 6, 7, and 8 the neutral axis locations were greater than 3 in. away from the calculated neutral axis value. Figures 4.16 and 4.17 are similar graphs for gauge grouping G2-C. Increments 9-12 were within 2 in. of the calculated value. Increment 3 shows a neutral axis position 10 in. higher that the theoretical value; however, this position is sensitive to the decreasing magnitude of a small strain value recorded in the top flange at this increment. Increments 6, 7, and 8 show neutral axis locations at least 7 in. lower than the theoretical value. It is assumed from Figures 4.14 through 4.17 that there was some loss of composite action between increments 4 and 8 caused by the close proximity of the concentrated loads to the gauge locations. The more consistent neutral axis position displayed from increments 9 to 17 was then perhaps due to the friction between the slab and the girder.
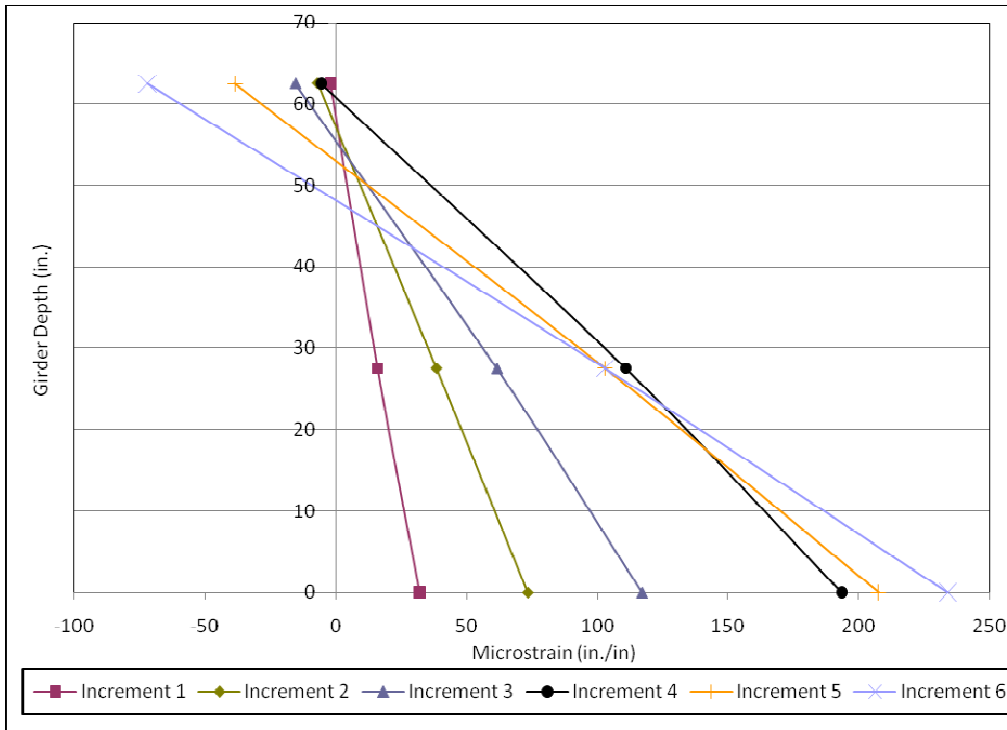
Figure 4.14   Gauge G2-A Cross-Section Strain Increments 1-6
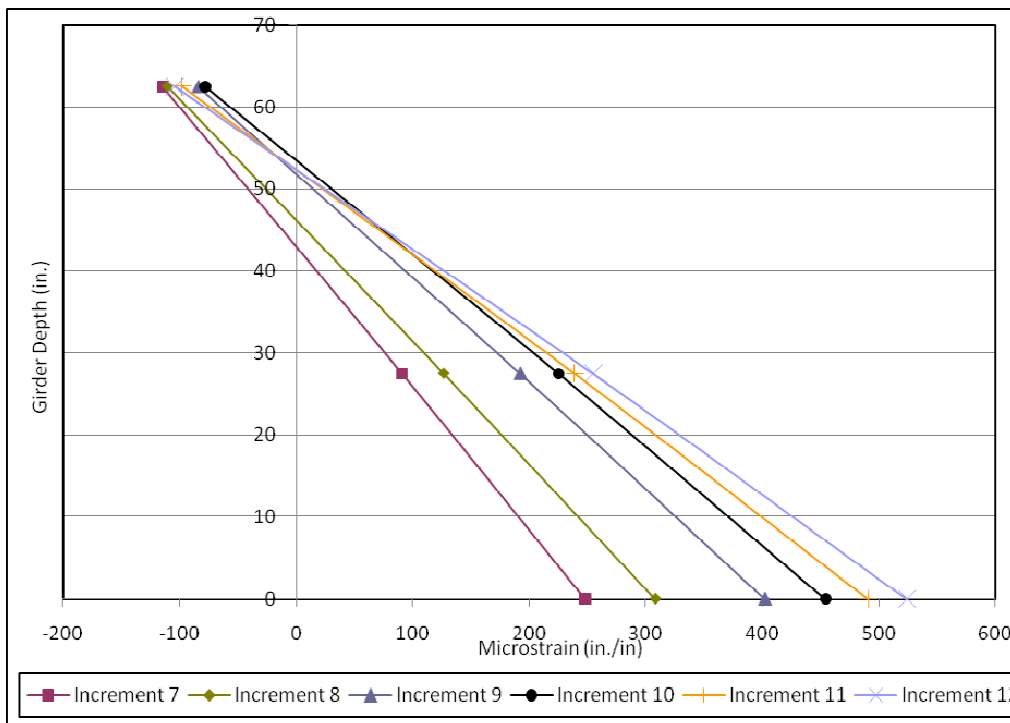
Figure 4.15   Gauge G2-A Cross-Section Strain Increments 7-12

48
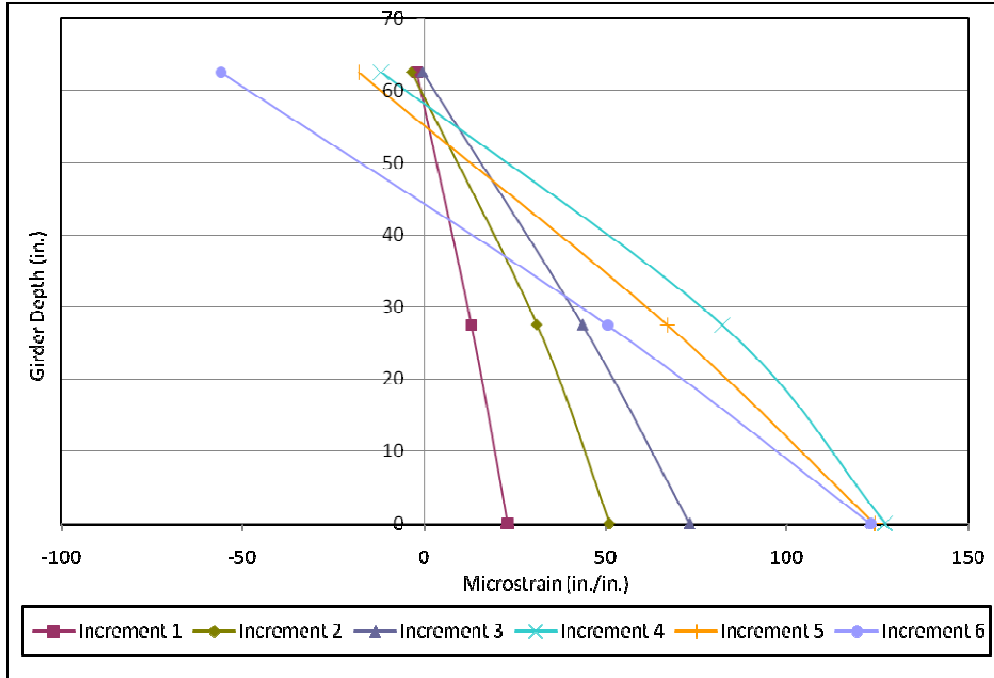
Figure 4.16   Gauge G2-C Cross-Section Strain Increments 1-6
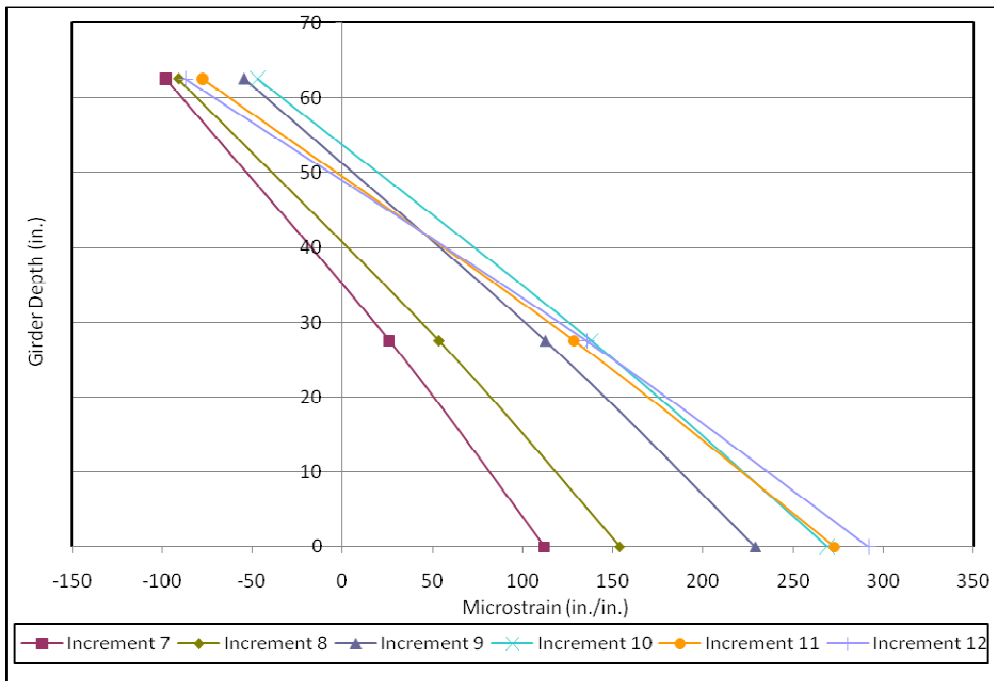
Figure 4.17   Gauge G2-C Cross-Section Strain Increments 7-12

4.3.2 Strain Evaluation

The ultimate goal of the destructive test was to evaluate the post-elastic response of the structure. However, the loadings onto the bridge were not sufficient to cause the structure to yield. A7 steel has an elastic modulus of 29,000 ksi and minimum specified yield strength of 33 ksi, making the yield strain of the girders to be at least 1138 microstrains. Gauge G2-BF2-A had the maximum recorded strain value of 872 microstrains. Including the estimated 175 microstrains from the dead load (based on the FEA results); the total strain at gauge G2-BF2-A is 1047 microstrains (which corresponds to a stress of 30.4 ksi). Thus, extrapolating the recorded data, it is predicted that yielding would have occurred at 19 trucks. However, it was discussed in the previous section that the cross-sectional strain plots suggest that there may have been some yielding in the bottom flange at increment 17. This could be due to the presence of residual stresses in the girder.

As mentioned in Section 3.4, according to the design codes, the factored (including the distribution factor and impact) number of trucks to cause yielding to Bridge 7R is 5 trucks and the un-factored capacity is 12 HS-20 trucks. The fact that during testing the girders did not yield until at least 17 truck loads demonstrates the significant reserve capacity of the structure that is unaccounted for in the modern design codes.

Figures 4.18 through 4.20 display graphs of the load increment vs. average microstrains in the bottom flanges, web and top flanges, respectively. These three graphs are plotted with consistent x and y-axis scales for better comparison between the three graphs. In general, these graphs report the average of the north and south gauges on each component of each cross-section with the exception that the average between G2-BF1-C

50

and G2-BF2-C (in Figure 4.18) was not used because the recorded values from G2-BF1-C were inconsistent compared to the other bottom flange strain data. Therefore strain gauge data from G2-BF2-C was used for this figure. All bottom flange and web strain values in Figures 4.18 and 4.19 are in tension and all top flange strain values in Figure 4.20 are in compression.

For the most part, the strain values decreased the further away the gauge location was from the loading centroid. The highest recorded strain values occurred at Gauge G2-BF-A , which was the gauge closest to the centroid of the bridge loadings. In Figure 4.18 Gauge G2-BF2-C and G3-A strain values were nearly the same through the first 9 increments of loading. At the final 8 increments of loading, Gauge G2-BF2-C strain values were greater than Gauge G3-A. Although Gauge G3-A is approximately 6 ft. closer to the centroid load compared to Gauge G2-BF2-C. The trend between the two gauges suggests that the loading travels longitudinally more so than transversely for this range of loading. This will be further evaluated throughout the full range of loading in the FEA analyses, as discussed in Section 5.2.2.

The gauge locations in Figures 4.18 and 4.19 (bottom flange and web locations) display an unusual trend generally between increments 4 and 7. The strain values increase from increments 1 to 3, but from increments 4 to 7, the strain values stay the same or in some instances decrease. This would suggest that the structure has infinite or negative rigidity, which is not possible. This odd trend is hypothesized to be a result of the lost composite action between increments 4 and 7 that was previously discussed in Section 4.3.1. As expected due to the neutral axis position, the top flange strain values

51
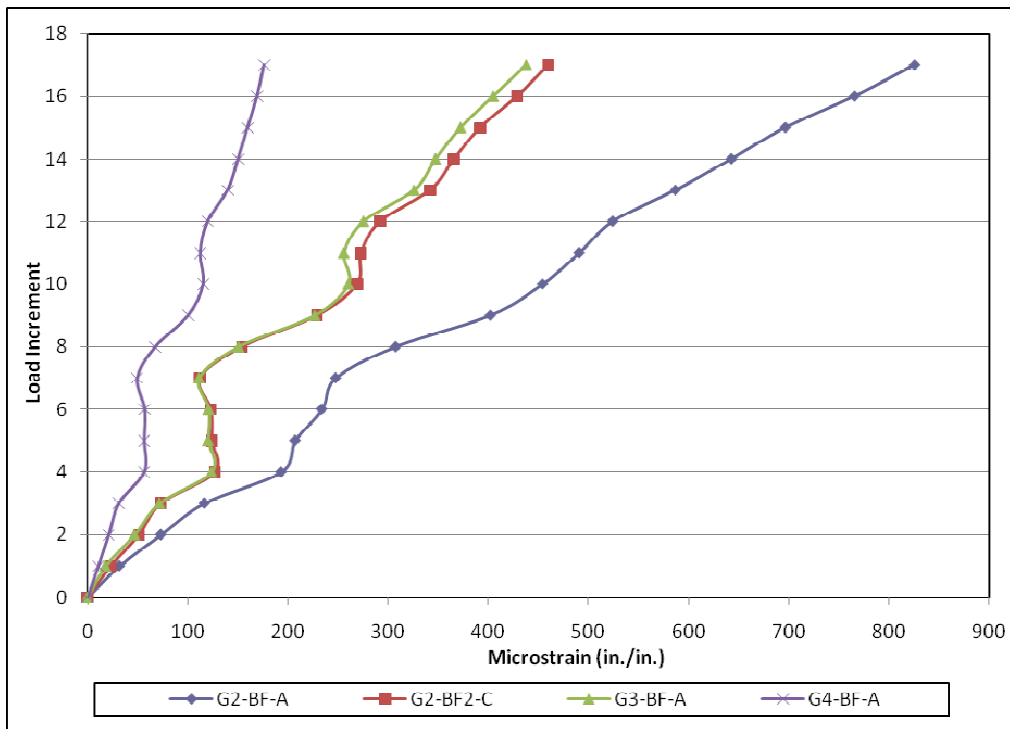
Figure 4.18 Field test bottom flange data
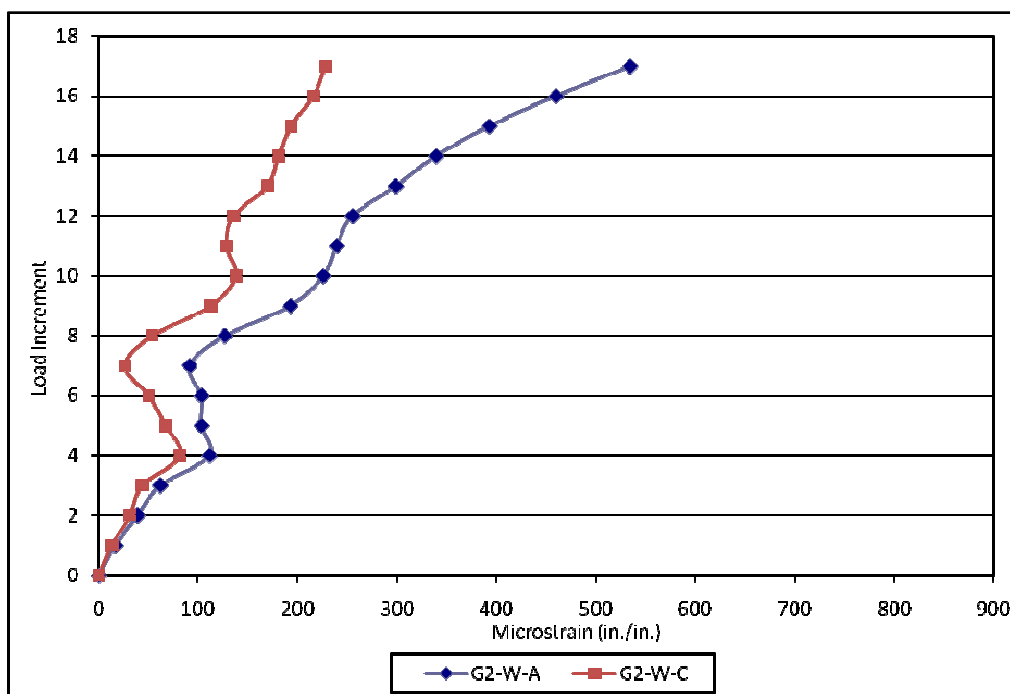
Figure 4.19 Field test web data
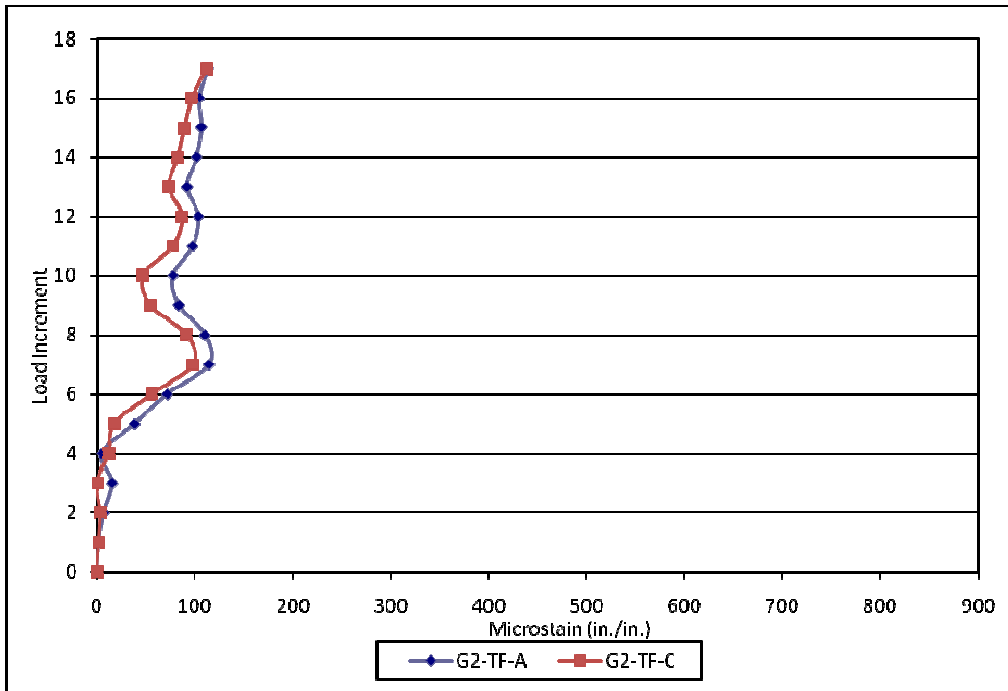
Figure 4.20   Field test top flange data (compression)

displayed in Figure 4.20 were relatively low. These strain values also show nonlinear

increases in strain indicating potential changes in the degree of composite action in

Girder 2.

4.4   Field Test Cross Frame Data

Although none of the girders yielded during the destructive test, yielding of

the cross frames was recorded at one location, Gauge CF3-BA2-A. This gauge was

located on the concentric leg of the bottom angle on Cross Frame 3. The location of this

cross frame relative to the bridge can be found in Figure 4.2 and Figure 4.4 displays the

location of Gauge CF3-BA2-A on this cross frame. Assuming the standard properties of

A7 steel, the yield strain of the cross frames is 1138 microstrains. The live load strain at

increment 10 exceeded this value by 7 microstrains (1145 microstrain). Adding the dead

load strain in this member that is predicted from the FEA (73 microstrains), brings the total estimated strain at increment 10 to 1218 microstrains following increment 10. The strain continues to increase up through increment 15, where the recorded strain is 1456 microstrains. Including the estimated 73 microstrains of dead load strain to this value, the total strain value in the cross frame is estimated to be 1529 microstrains, which exceeds the estimated yield strain by 34%. Gauge CF3-MA1-A had the next highest recorded strain value at 728 microstrains. The estimated dead load strain at this location was only 14 microstrains, for a total of 7 42 microstrains.

Figures 4.21 through 4.23 graphs the strain history of the gauges that are attached to the concentric legs of the cross frame members (Gauges CF3-BA1-A, CF3-MA2-A, CF3-TA2-A, CF4-BA1-A, CF4-MA2-A, and CF4-TA2-A), where the data is grouped according to whether the gauge is on the bottom, middle, or top chord of the cross-frame. Corresponding graphs for the gauges that were attached to the eccentric angle leg (Gauges CF3-BA2-A, CF3-MA1-A, CF3-TA1-A, CF4-BA2-A, CF4-MA1-A, and CF4-TA1-A) are included in Figures 4.24 through 4.26. For the strain gauges that are attached to the bottom and top chords, positive readings denote tension. While for the strain gauges that are attached to the middle chords, positive reading denote compression.

Several general trends can be observed from Figures 4.21 through 4.26. First, it is seen that the strains generally increase with increasing applied load. In comparing the relative magnitudes of the different gauges it is shown that, as expected, the concentric legs have much higher strain values than the eccentric legs, which typically have strains less than 100 microstrains (the only exception being gauge CF3-BA1-A), including fluctuations between tension and compression. It is also shown that

the strains in CF3 are much higher than the strains in CF4 (by 2 to 6 times in the concentric leg at the last load increment), which is logical since CF3 is much closer to the applied load. Comparing the readings from the different members comprising the cross frames it is also seen that the most strain exists in the bottom angles, followed by the middle angles and then the top angles.

The strain values for the gauges that were attached to concentric legs of Cross Frame 3 also give some insight into the system response of the bridge. As discussed above, it is estimated that the bottom angle of this cross frame began to yield at increment 10. In looking at the data from all of the concentric leg gauge readings on this cross frame (CF3-BA2-A, CF3-MA1-A, and CF3-TA1-A), the strain began to decrease or stays the same (CF3-TA1-1) at increment 15 or 16 in all three cases. The strain also began to decrease in two (CF3-MA1-1 and CF2-TA1-1) of the three eccentric legs at
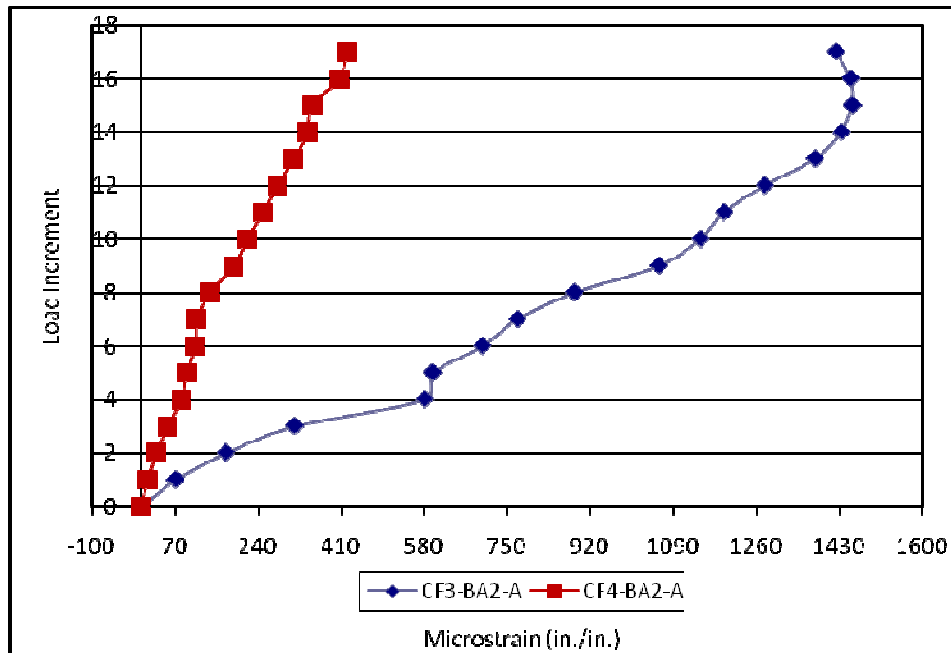
Figure 4.21 Field Test Concentric Leg Bottom Angle Data (tension is positive)
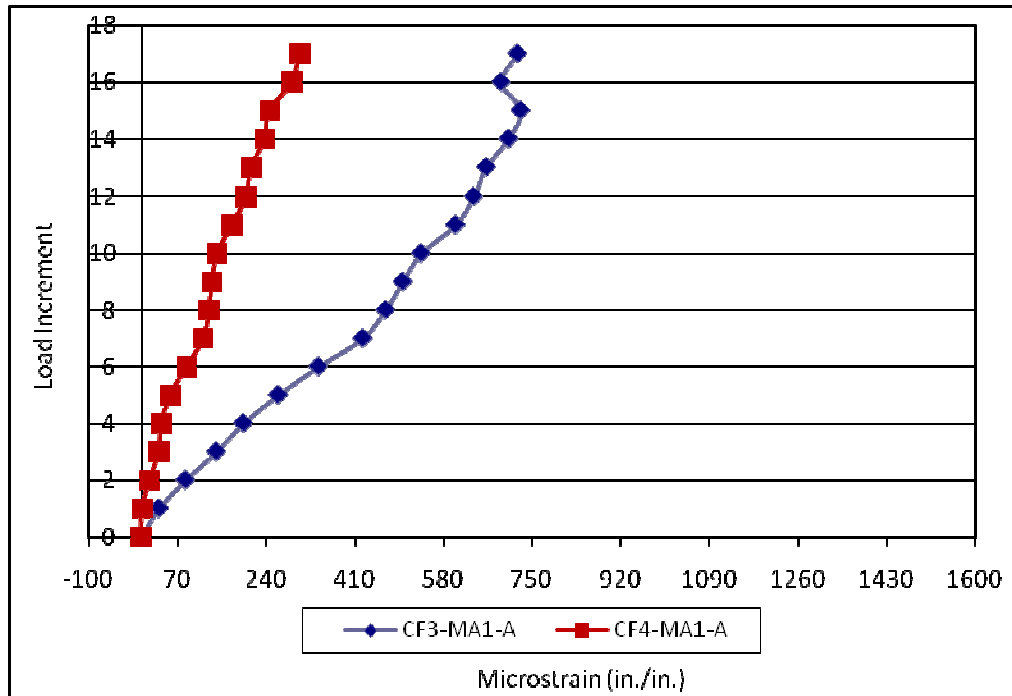
Figure 4.22   Field Test Concentric Leg Middle Angle Data (compression is positive)
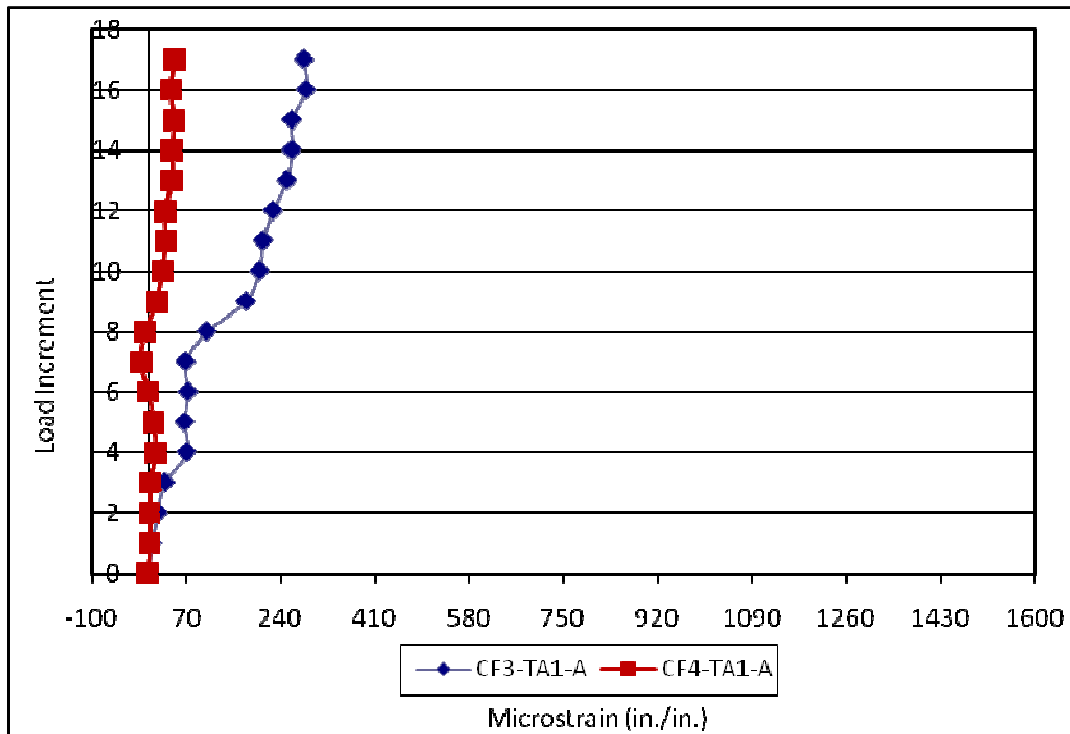
Figure 4.23   Field Test Concentric Leg Top Angle Data (tension is positive)

56
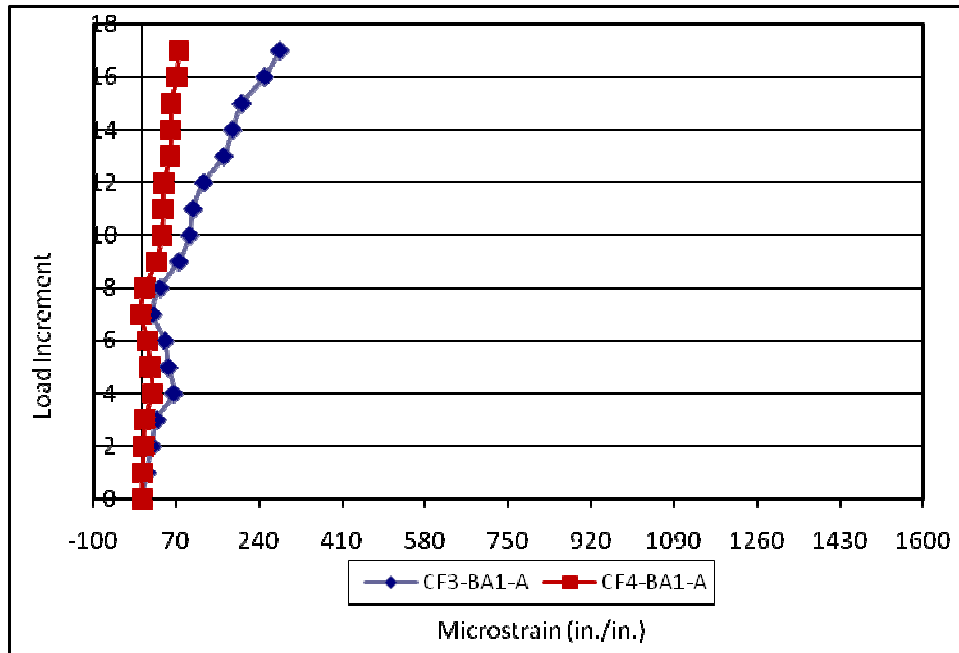
Figure 4.24   Field Test Eccentric Leg Bottom Angle Data (tension is positive)

increment 16 (although this is less meaningful due to the more significant fluctuations in these gauge readings). This suggests a potential change in the load distribution characteristics of the bridge in that less load is being transmitted through Cross Frame 3. This may have been caused by the high magnitude of loading.
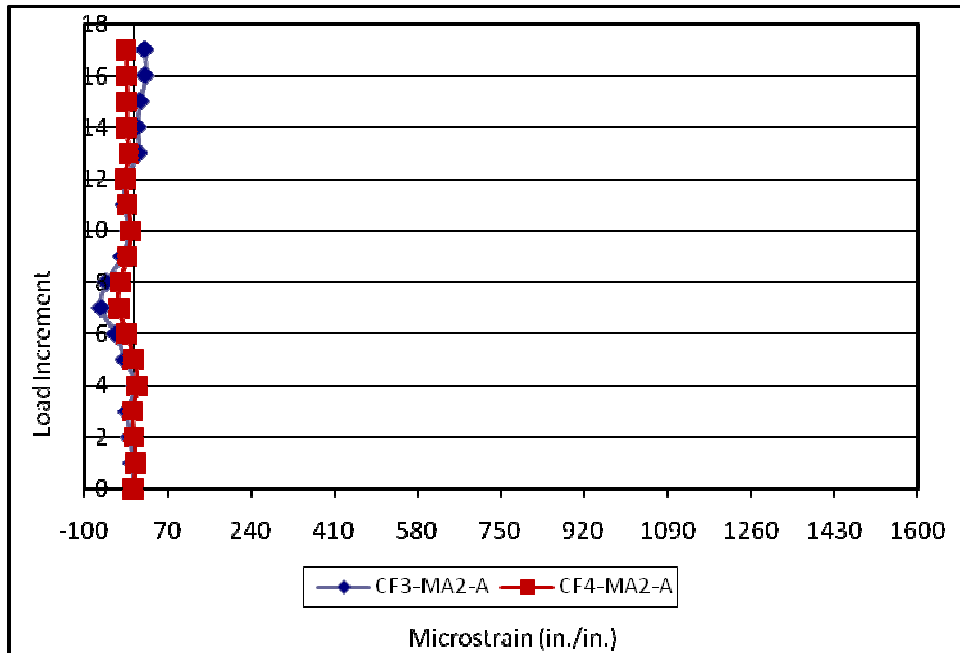
Figure 4.25   Field Test Eccentric Leg middle Angle Data (compression is positive)
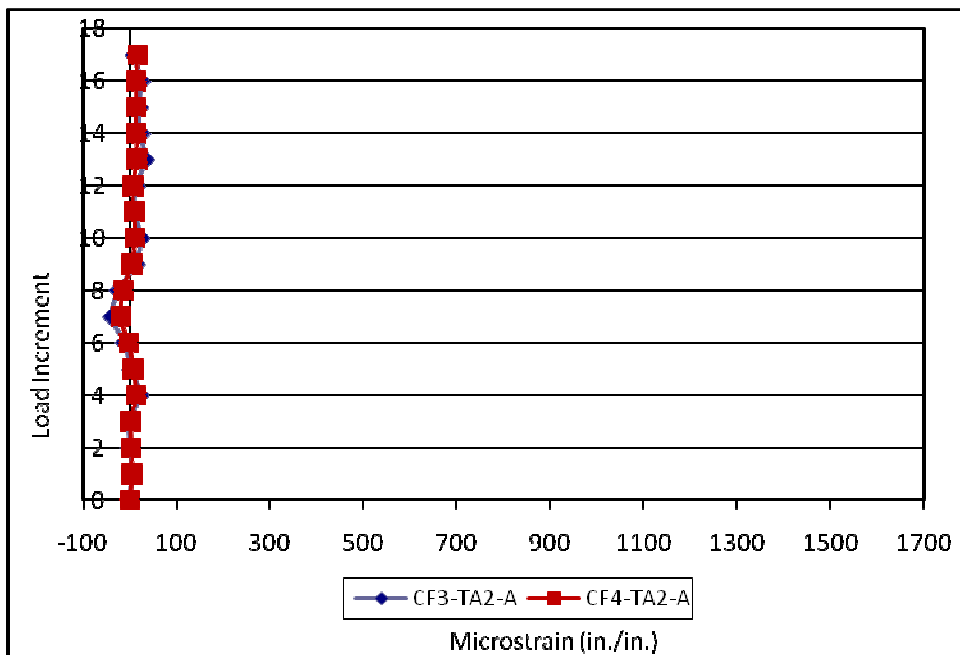
Figure 4.26   Field Test Eccentric Leg Top Angle Data (tension is positive)

58

Chapter 5

FEA RESULTS

A finite element model (FEM) of Bridge 7R was originally created in an earlier study (Ross 2007) to predict the response of Bridge 7R during the destructive test. However, when the results from the model were compared to the actual destructive test results, significant differences were observed. Therefore, the original FEM created by Ross was calibrated to achieve better correlation between the destructive test and FEA results.

Section 5.1 explains the process of how the FEM was calibrated and the rationale used to select the final input parameters for the FEA. At the end of this section the calibrated FEA is compared to the destructive test data. After the model has been validated, Section 5.2 analyzes the results from the calibrated model. The original FEA that was created by Ross (2007) predicted that a plastic moment could form in all four girders of the structure and the ultimate capacity was taken as the load at this stress state. However, the calibrated FEA reached an ultimate capacity before a plastic moment was formed at every girder. Section 5.3 discusses the mechanisms governing the ultimate capacity of the calibrated FEA and Section 5.4 summarizes the ultimate behavior observed in the FEA.

5.1   FEA Calibration

The original FEM created by Ross (2007) was used initially to model the destructive bridge test. The Ross model, or the original model, was created based on the diagnostic test that was completed in 2005, where a 32.5 ton triaxle dump truck was used to load the bridge. During the diagnostic test, this load vehicle was driven across the bridge at three different transverse positions (see Section 2.2 for a full description of the diagnostic testing). The original model was then calibrated based on the longitudinal and transverse position of the load that caused the worst-case scenario at the midspan of each girder. Load distribution under such worst-case scenarios is a fundamental concept in the current line girder approach to bridge design and is relatively well understood. Furthermore, this means that while the load distribution properties of the model were important, the load is typically being distributed over a relatively short distance before arriving at the point of interest.

In contrast, during the destructive bridge test, the loading mechanism was in a fixed location. This necessitated that the load must be distributed over significant longitudinal and/or transverse distances before reaching some gauge locations. Thus, the load distribution properties of the FEA were critical in achieving good correlation between the FEA and field test results and a much more significant evaluation of these properties was required compared to Ross' earlier work.

It should also be noted that a source of some uncertainty in the calibration process is the exact loading applied during the destructive test. As discussed in Section 4.2, it is believed, based on instrumentation readings from 25% of the rods in the reaction frame that the applied loadings were within an acceptable margin of the intended truck

60

loadings. However, the actual loadings cannot be precisely determined. Thus, the intended loadings are assumed to be the load condition when comparing the field test and FEA results.

5.1.1 Original Model

All details of the original FEA were the same as Ross' (2007) final model with the exception of the load input since the loading conditions varied between his preliminary work and the final destructive testing conditions. The finite element analysis was completed using the Riks analysis algorithm available in the commercial finite element software Abaqus. The plate girder, haunch, slab, and end diaphragms were modeled using a relatively fine mesh of 4-node, reduced-integration shell elements. Specifically, the size of the girder elements was typically 2.5 in. square, while the concrete components were typically 7 in. square elements. The cross-frame members were modeled using beam elements. The girder, haunch, and deck were connected using rigid links. In order for this connection to exist in a common vertical plane, a very fine mesh was created along the centerline of the haunch and a merge tolerance of 0.25 in. was used.

The supports of the bridge were modeled using gap elements. These elements allow for uplift at supports but act as a rigid vertical support when a compressive load is applied. These were used because it was revealed that, due to the skewed alignment of the bridge, the torsional stresses within the structure were significant enough to cause uplift at the acute corners of the bridge at some levels of loading. Since there was no mechanism to resist this upward movement in the bearings, the boundary conditions of the model accurately represent this condition.

A bilinear stress-strain relationship, representing the elastic and strain hardening regimes, was input for the girders assuming a 36 ksi yield strength of the steel. The influence of inelastic material properties for the other steel components was investigated, but it was determined that inputting elastic material properties for these components had a negligible effect on results and allowed the analysis to be processed with greater efficiency. Similar results were obtained when inelastic material properties were input for the concrete components (Ross 2007); thus, concrete is assumed to behave linearly-elasticly in the analysis.

The Riks method of analysis contains an optional check for equilibrium due to the presence of geometric nonlinearities. There were difficulties in obtaining convergence when using this option, so geometric nonlinearities are not included in the analysis.

The loadings were applied via six arrays of points loads centered about the node closed to the center of the 150 ton hydraulic jacks used during the destructive test of Bridge 7R. These locations with respect to the bridge were previously shown in Figure 3.1. Each array consisted of a 3-node by 3-node square. Using a loading area equivalent to the full area of the 4 ft by 8 ft load plates located underneath the loading jacks was also investigated as an opposite extreme and negligible results were observed between these two analyses. The six 9-node arrays were then used in all further analyses.

5.1.2   2010 Models

The original model was varied with eight different sets of input parameters, until a calibrated model was chosen to predict the response of the bridge. To achieve the goal of improving the transverse and longitudinal load distribution properties of the

62

model, the elastic modulus (E) of the concrete and the cross frames were the primary parameters investigated as the concrete deck and the cross frames are the components responsible for transverse distribution of force. Thus, changing the stiffness of these members will change the distribution of stress in the bridge and allow for a better correlation with the field data results. While the elastic modulus of the cross frames is known with reliable certainty to be 29,000 ksi, the purpose of varying this property was to quickly evaluate the influence of cross frame rigidity. This rigidity can vary due to the end fixity of the cross frames, which was evaluated more rigorously through changing the connection between the cross frames and the girder after sensitivity to cross frame rigidity was observed.

Out of the eight models analyzed during the calibration process, in four models elastic modulus of the concrete was altered. These models were specifically changed by 8 (3,064,000 psi), 2 (726,000 psi), 1.5 (574,500 psi), and 1/8 (47,875 psi) times the original elastic modulus of concrete (383,000 psi). While some of these values are obviously not realistic, these analyses were meant to show the influence of concrete stiffness. In the remaining four models, cross frame properties were adjusted. Two of these models were altered by inputting 2 (58,000,000 psi) times and ½ (14,500,000 psi) times the original elastic modulus (29,000,000 psi) of the cross frames. In the last two models, the connection between the cross frames and girders were changed from fixed (via merged nodes) to pinned. In one of these models, all other input values were equal to the original input and in the other the elastic modulus of the concrete was increased by 1.5 times.

5.1.3   Evaluation of the 2010 Models

The eight 2010 models were evaluated by comparing the load applied to the structure vs. bottom flange strain obtained from the FEA to that from the field test. The bottom flange gauges were emphasized because this type of data exists for the most locations in the field test and because these strains are among the highest strains recorded. Figures 5.1 and 5.2 show this data for Gauge G2-A for each analysis, where Figure 5.1 shows the analyses with increased elastic modulus values and Figure 5.2 shows the remaining analyses. The corresponding graphs for all other gauges can be found in Appendix B. After viewing these graphs it was concluded that the slopes (load increment divided by strain) of the various series was the most reliable and convenient metric to carry out comparisons.

This data is presented in Tables 5.1 through 5.4 for each analysis and the field test, where each table shows the response at a particular gauge grouping. Table 5.1 displays the data from Gauge G2-A located on Girder 2, Table 5.2 displays the data from Gauge G2-BF2-C located on Girder 2, Table 5.3 displays the data from Gauge G3-A located on Girder 3, and finally Table 5.4 displays the data from Gauge G4-A located on Girder 4. Figure 4.2 shows the exact location of these gauges on the bridge. Each table follows the same order from top to bottom starting with the field data, original model, models with increased elastic modulus, models with decreased elastic modulus, and models with pinned cross frames.

Not only were the slopes over the entire loading range (increments 1 through 17) compared, but the slopes between increments 1 through 4 were also separately calculated. This was done because of the hypothesized change in composite action that
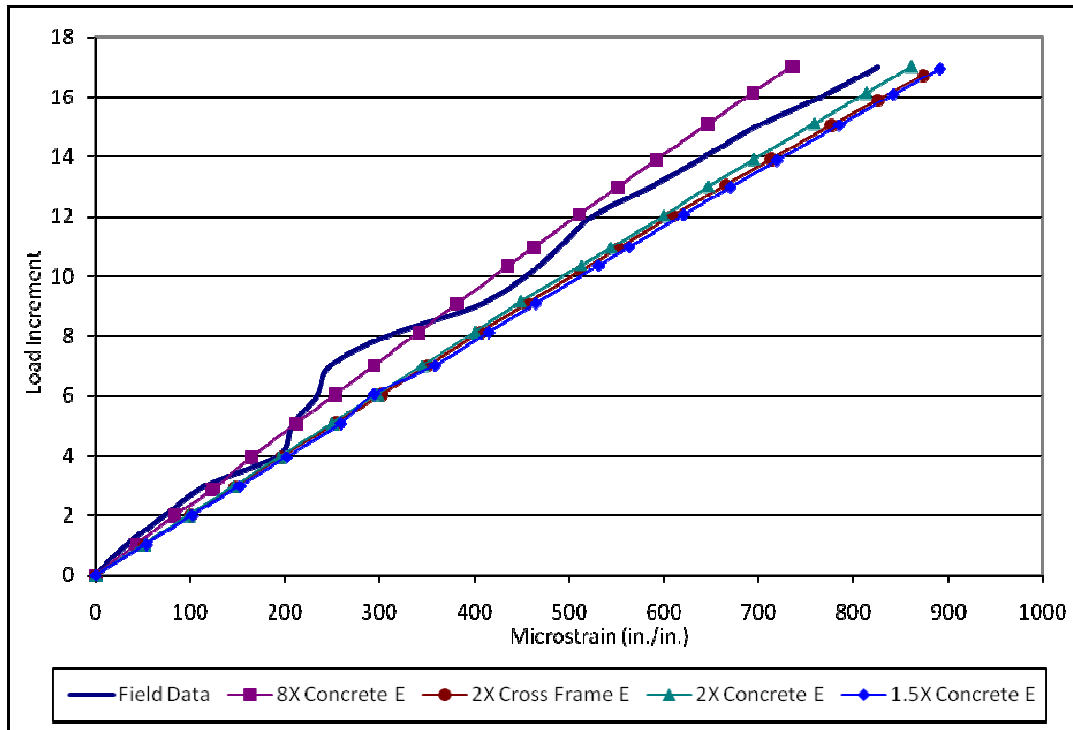
Figure 5.1   Gauge G2-A Increased E FEM

was previously mentioned between increments 4 and 7 in the field test (see Section 4.3).

Because full composite action is assumed throughout the FEA, which was appropriate

since this problem appears to self-correct in the field test, the strains during these

increments (4 through 7) are expected to differ. This will also affect all later strain

values, although the slopes of the FEA and field test should be equivalent once composite

action is restored after increment 7. Thus, the slope values from the full loading range

and increments 1 through 4 are separately tabulated so as to examine the total response

and the response independent of the hypothesized composite action problems.

Tables 5.1-5.4 display the percent differences between the FEA and field test

slopes in the far two right columns. These values were calculated by taking the absolute
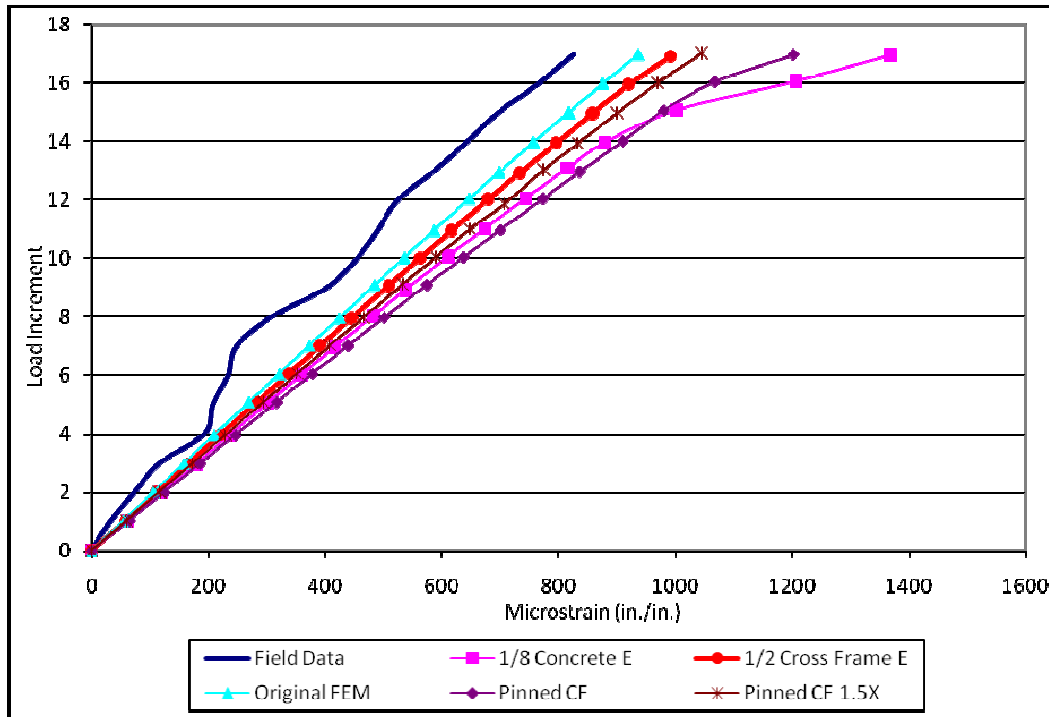
Figure 5.2   Gauge G2-A Remaining FEM

difference between the field data and a specific model, and dividing the value by the field data.

Overall the original model predicted greater strain values (lower slopes) at the majority of increments than what was observed during the field test. In order to decrease the strain values at each increment, the slopes of the load versus strain relationships had to increase to better match the field data. It is intuitive that to decrease the strain, the stiffness of the model should be increased. The results in Tables 5.1 through 5.3 demonstrate that at these three gauge locations, increasing the stiffness (by increasing E of the concrete or the cross-frames) does in fact have the desired effect of increasing the load versus deflection slopes. The converse of this is also true in that when the global stiffness is decreased (by lowering the elastic modulus of the concrete or

removing the moment connection between the ends of the cross-frames and the girders), the slopes decrease at these three gauge locations.

However, for the Girder 4 results in Table 5.4 there is no clear relationship between increasing or decreasing the global stiffness and the resulting change in slope. The more complex behavior at this girder is attributed to the fact that it is the only girder that does not receive load directly from the loading mechanism (in that the loading jacks are placed in one line between Girders 1 and 2 and another line between Girders 2 and 3). Thus, the load distribution to Girder 4 is more complex and increasing the global stiffness of the structure has competing effects on the Girder 4 response.

This fact that there is not a clear relationship between the global stiffness of the structure and the load distributed to Girder 4 is demonstrated in Table 5.5, where the percentage of load distributed to Girder 4 was tabulated for each analysis. For example, increasing the global stiffness of the structure through increasing the elastic modulus of the deck should cause the girders to act less independently and distribute more loads to Girder 4. However, Table 5.5 shows that as the elastic modulus of the concrete was varied, the percentage of load distributed to Girder 4 reaches a minimum when the elastic modulus equals two times the base value. It is hypothesized that this is influenced by the skew of the bridge; specifically, as the elastic modulus of the concrete decreases, Girder 2 deflects more and because the point of the maximum deflection of Girder 2 is in close proximity to the east support of Girder 4, the amount of load transferred to Girder 4 begins to increase. Thus, there are competing affects of varying the elastic modulus of the concrete. However, changing the global stiffness of the structure via altering the

cross frame stiffness follows the expected trend of stiffer structures distributing more load to Girder 4 and vice versa.

Increasing the elastic modulus also increases the stiffness of this member, which would decrease the strains in Girder 4. However, it is shown In Table 5.5 that the variation in strain at truck increment 4 (which was selected since this is where the FEA slopes were evaluated above and calculated using these slopes to compare the strain at exactly the same load level) follows the same trend as the load distribution. That is, as less load is distributed to Girder 4 there is less strain in Girder 4. This suggests that the local stiffness of the member does not play a significant role in explaining the Girder 4 slopes above. Thus, it is concluded that the models with the least load distributed to Girder 4 demonstrate the highest slopes in Table 4.4.

Table 5.6 ranks the most accurate models (with being the most accurate) with respect to the field test data for each gauge grouping between Increments 1 through 17 and 1 through 4. As shown Table 5.6 it is difficult to understand which model should be chosen to represent the field data. At every gauge location and between increments the accuracy between percent differences changes often and no one model stands out from the others. Table 5.7 shows the average of the four percent difference values (given in Tables 5.1 through 5.4) for the four gauge locations from each model (again for increments 1 through 4 and 1 through 17). The column at the far right is denoted as the overall percent difference averages and was calculated by taking the average of the increments 1 through 17 and 1 through 4 data shown to the left of this. This can be thought of as equally weighting the results of the initial portion of the response before the hypothesized composite action problems arose and the entire response. Based on the

FEM	Increment 1-17 Slope	Field Data % Difference Increments 1-17	Increment 1-4 Slope	Field Data % Difference Increments 1-4
Field Data	0.0205	0%	0.0206	0%
2009 FEM	0.0183	11%	0.0189	8%
8X Concrete E	0.0233	14%	0.0237	15%
2X Cross Frame E	0.0193	6%	0.0201	2%
2X Concrete E	0.0199	3%	0.0204	1%
1.5X Concrete E	0.0198	3%	0.0196	5%
1/2 Cross Frame E	0.0173	16%	0.018	13%
1/8 Concrete E	0.0134	35%	0.0167	19%
Pinned CF	0.0148	28%	0.0161	22%
Pinned CF 1.5X	0.0165	20%	0.0173	16%

Table 5.1   Gauge G2-A FEM Slope Comparison

FEM	Increment 1-17 Slope	Field Data % Difference Increments 1-17	Increment 1-4 Slope	Field Data % Difference Increments 1-4
Field Data	0.0363	0%	0.0318	0%
2009 FEM	0.0328	10%	0.0343	8%
8X Concrete E	0.0418	15%	0.0437	37%
2X Cross Frame E	0.036	1%	0.038	19%
2X Concrete E	0.0355	2%	0.0369	16%
1.5X Concrete E	0.0342	6%	0.0355	12%
1/2 Cross Frame E	0.0301	17%	0.0313	2%
1/8 Concrete E	0.0304	16%	0.0318	0%
Pinned CF	0.0266	27%	0.0287	10%
Pinned CF 1.5X	0.0292	20%	0.0308	3%

Table 5.2   Gauge G2-BF2-C FEM Slope Comparison

FEM	Increment 1-17 Slope	Field Data % Difference Increments 1-17	Increment 1-4 Slope	Field Data % Difference Increments 1-4
Field Data	0.0384	0%	0.0319	0%
2009 FEM	0.0268	30%	0.0271	15%
8X Concrete E	0.032	17%	0.032	0%
2X Cross Frame E	0.0281	27%	0.0288	10%
2X Concrete E	0.0283	26%	0.029	9%
1.5X Concrete E	0.0278	28%	0.0282	12%
1/2 Cross Frame E	0.0256	33%	0.0261	18%
1/8 Concrete E	0.0222	42%	0.0227	29%
Pinned CF	0.0251	35%	0.0257	19%
Pinned CF 1.5X	0.0263	32%	0.0269	16%

Table 5.3   Gauge G3-A FEM Slope Comparison

FEM	Increment 1-17 Slope	Field Data % Difference Increments 1-17	Increment 1-4 Slope	Field Data % Difference Increments 1-4
Field Data	0.0926	0%	0.0713	0%
2009 FEM	0.0485	48%	0.0472	34%
8X Concrete E	0.0473	49%	0.0466	35%
2X Cross Frame E	0.0468	49%	0.0455	36%
2X Concrete E	0.0495	47%	0.0491	31%
1.5X Concrete E	0.0493	47%	0.0485	32%
1/2 Cross Frame E	0.0497	46%	0.0487	32%
1/8 Concrete E	0.0434	53%	0.0404	43%
Pinned CF	0.0574	38%	0.0551	23%
Pinned CF 1.5X	0.0561	39%	0.0547	23%

Table 5.4   Gauge G4-A FEM Slope Comparison

Analysis	Percent of Load Carried by Girder 4	Microstrain
8X Concrete E	17.43%	84
2X Concrete E	16.26%	80
1.5X Concrete E	16.27%	81
Original Model (1X Concrete E)	16.53%	84
1/8 Concrete E	20.28%	97
2X Cross Frame E	16.88%	87
1/2 Cross Frame E	14.47%	81
Pinned CF	12.95%	71
Pinned CF with 1.5X Concrete E	7.80%	72

Table 5.5   Percent of Load Carried by Girder 4

overall percent difference averages in Table 5.7, the model with 2 times the elastic modulus of concrete best resembled the field response of the bridge, followed by the model with 1.5 times the elastic modulus of concrete and the model with 2 times the elastic modulus of the cross frames.

The model with 1.5 times the elastic modulus of concrete was then chosen as the final calibrated model. This is based on the fact that, of the three models being identified as "best" in the previous paragraph, this model has the most realistic input.

Using 150 pcf as the density of concrete, and the relationship for equation 2, the theoretical strength of concrete corresponding to an E value of 1.5 times the original value is 9 ksi. While this value is high, it is within reason of potential upper-bounds of concrete strength that may have been possible in the structure. The corresponding strength of concrete for the model that has 2 times the original elastic modulus of concrete is 16 ksi. This strength of concrete is much less likely to reflect the concrete strength in the actual structure. Furthermore, as previously discussed, it is not likely that there is any significant variation in the elastic modulus of the cross-frames, so these

Gauge G2-A		
Rank	Increments 1-17	Increments 1-4
1	2 times the E of concrete	2 times the E of concrete
2	2 times the E of cross frames	2 times the E of cross frames
3	2 times the E of cross frames	2 times the E of cross frames
Gauge G2-BF2-C		
Rank	Increments 1-17	Increments 1-4
1	2 times the E of cross frames	1/2 the E of cross frames
2	2 times the E of concrete	Pinned cross frame connection
3	1.5 times the E of concrete	pinned cross frame connection & 1.5 times the E of concrete
G3-A		
Rank	Increments 1-17	Increments 1-4
1	8 times the E of cross frames	8 times the E of cross frames
2	2 times the E of concrete	2 times the E of concrete
3	2 times the E of cross frames	2 times the E of cross frames
G4-A		
Rank	Increments 1-17	Increments 1-4
1	Pinned cross frame connection	Pinned cross frame connection
2	1.5 times the E of concrete	1.5 times the E of concrete
3	1/2 the E of cross frames	2 times the E of concrete

Table 5.6   Accuracy of FEA compared to the field test

FEM	Increments 1-17 % Difference Averages	Increments 1-4 % Difference Averages	Overall % Difference Averages
2009 FEM	25%	16%	20%
8X Concrete E	24%	22%	23%
2X Cross Frame E	21%	17%	19%
2X Concrete E	19%	14%	17%
1.5X Concrete E	21%	15%	18%
1/2 Cross Frame E	28%	16%	22%
1/8 Concrete E	37%	23%	30%
Pinned CF	32%	18%	25%
Pinned CF 1.5X	27%	15%	21%

Table 5.7   Percent Difference Values

models were not considered as being viable options for the final calibrated model. Thus, the model with the elastic modulus of concrete increased by 150% is believed to offer the best combination of realistic input and correlation with the field test.

$$\left(\frac{E}{33 * w^{1.5}}\right)^2 = f'c$$

(2)

This model gives results that are within 15% of the Girder 2 results and Girder 3 increments 1 through 4 results although there is still significant variation (31%) with the Girder 4 increment 1 through 4 (and increment 1 through 17) results. It is not known if the poor correlation between the FEA and field data for Girder 4 is a result of inadequacies in the modeling or some unaccounted for physical attribute of the system. It is logical that this girder would have the weakest correlation between the FEA and field data because it is farthest from the loading, thus requiring a more precise representation of the system's response to achieve consistent results. However, Ross (2007) observed similar low strain values in Girder 4 during diagnostic field testing of the bridge when the load was placed directly over Girder 4. Furthermore, when the load position was reflected about the longitudinal centerline such that Girder 1 should have a similar response, much higher strains (nearly 50% higher) were achieved in Girder 1. This suggests that either Girder 4 is much stiffer or much less load is transferred to Girder 4 than would be expected based on traditional bridge analysis assumptions. Thus, it is not surprising that the Girder 4 field response was not well duplicated by the FEA.

5.1.4   Calibrated FEA and Field Data Comparison

Table 5.8 compares the strains at each bottom flange gauge location for each of the seventeen increments of the calibrated FEM to the field data. The percent

difference was calculated by taking the absolute difference between the calibrated model and field data, and dividing the value by the FEA data. It is noted that this is mathematically consistent with the method of computing percent differences in the previous section where the strain values were used in the denominator when calculating slopes. The percent difference averages for the 17 increments at each gauge location were taken and are shown at the bottom of the far right column in Table 5.8. The average percent difference values are 14% for Gauge G2-BF2-C and 17% for Gauge G2-A. Both of these gauges are located on Girder 2. As the distance between the gauge location and the applied loading increases, the percent difference values increases significantly. Gauge G3-A is located on Girder 3 which is the next girder north of Girder 2. Gauge G4-A is located on Girder 4 which is the most north girder of the bridge and the next girder north of Girder 3. The average percent difference is 35% for Gauge G3-A and 49% for Gauge G4-A. This suggests that the calibrated FEA accuracy decreases the further the gauges are away from the loadings. However, there is likely some additional elusive explanation for the lack of correlation for the Girder 4 results as discussed in the previous subsection.

Figures 5.3 through 5.6 graphically compare the bottom flange strains from the calibrated FEA and field data. Similar graphs of the web, top flange, and cross frames can be seen in Appendix D. The field data strain values at each increment are generally greater than the calibrated model strain values in the graphs. For the Girder 2 data, this is attributed to the fact that the strain increased very little between increments 4 and 7 during the destructive test (which has been previously discussed in Section 4.3) as it is observed that the slopes of the FEA and field data are very similar for the remaining

74

Increments	Calibrated Finite Element Model				Field Data				% Difference			
	G2-BF-A	G2-BF2-C	G3-BF-A	G4-BF-A	G2-BF-A	G2-BF2-C	G3-BF-A	G4-BF-A	G2-BF-A	G2-BF2-C	G3-BF-A	G4-BF-A
1	53	29	38	21	32	23	18	11	40%	21%	53%	48%
2	102	57	71	41	74	51	47	21	27%	11%	34%	49%
3	152	84	106	61	117	73	72	31	23%	13%	32%	49%
4	201	111	141	82	194	127	124	57	3%	-14%	12%	30%
5	259	144	181	105	208	124	121	57	20%	14%	33%	46%
6	294	171	216	125	234	123	121	57	20%	28%	44%	54%
7	358	198	250	145	248	112	112	50	31%	43%	55%	66%
8	415	231	290	168	308	154	151	68	26%	33%	48%	60%
9	465	258	325	188	403	229	227	101	13%	11%	30%	46%
10	531	295	370	213	455	269	261	116	14%	9%	29%	46%
11	563	313	392	226	491	273	256	113	13%	13%	35%	50%
12	621	346	432	248	525	292	276	120	15%	16%	36%	52%
13	670	360	465	266	587	342	326	140	12%	5%	30%	47%
14	719	401	498	283	643	366	348	151	11%	9%	30%	47%
15	785	439	541	306	697	392	373	160	11%	11%	31%	48%
16	842	471	579	326	766	429	405	170	9%	9%	30%	48%
17	891	499	610	342	826	460	438	177	7%	8%	28%	48%
								Average:	17%	14%	35%	49%

Table 5.8   Strain comparison chart for 1.5 times the elastic modulus of concrete FEA and field test
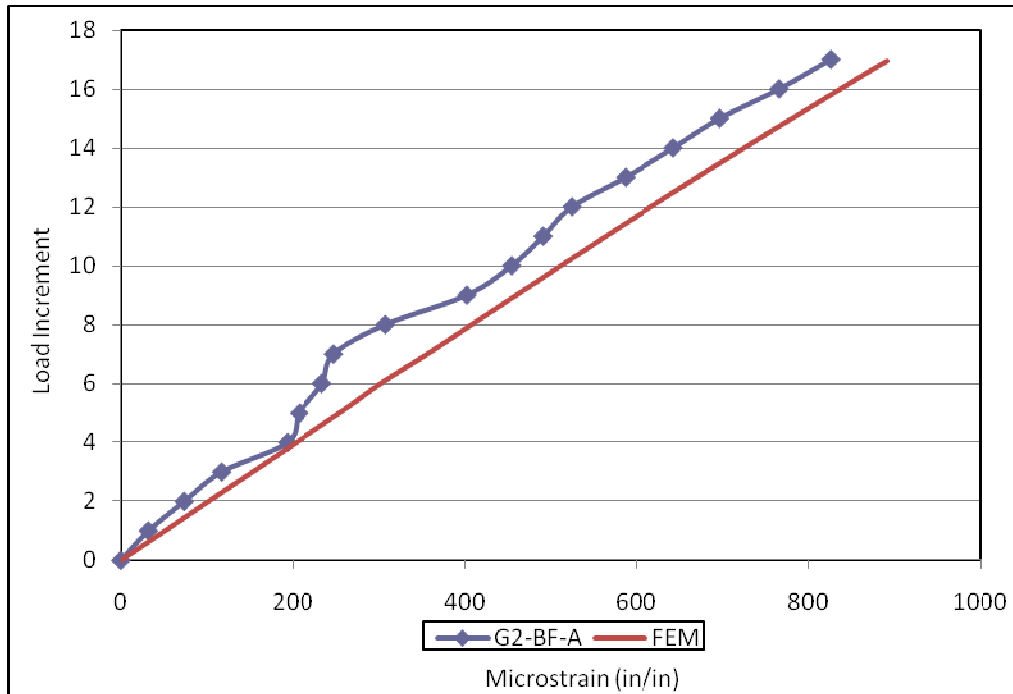
Figure 5.3   Gauge G2-BF-A Field Data and Calibrated FEM Results

increments. This behavior between increments 4 and 7 also influences the Girder 3 and 4 data, but for these locations, the slopes between the FEA and destructive test are less similar throughout the loading range. This again suggests that the calibrated FEA accuracy decreases the further the gauges are away from the loadings.

5.2   Calibrated FEA Results

The primary purpose of creating the FEA was to predict the post-elastic response of the bridge in order to better understand the system behavior of this common bridge configuration. It was determined through the FEA that the ultimate capacity of this structure was 30 HS-20 trucks. The purpose of this section is to investigate the response of the bridge up to this level of loading.
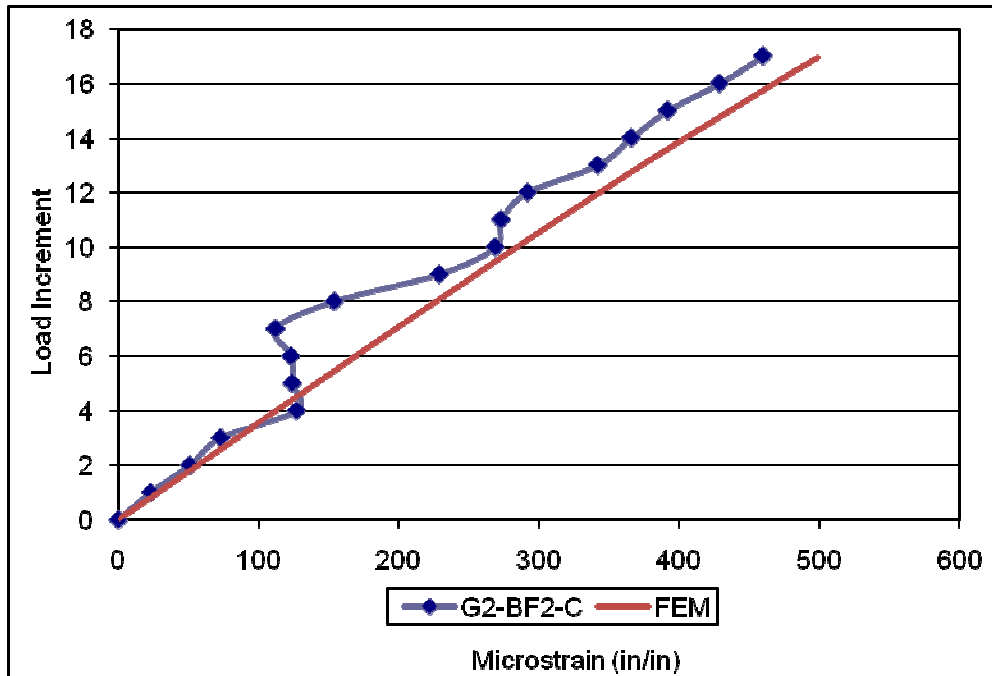
**Figure 5.4   Gauge G2-BF2-C Field Data and Calibrated FEM Results**
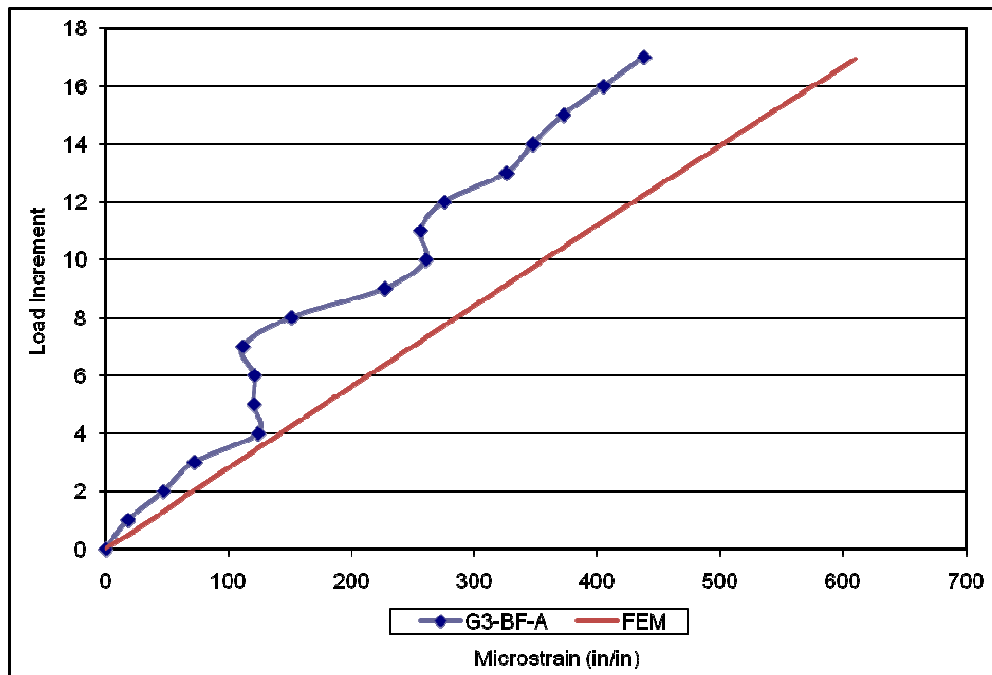
**Figure 5.5   Gauge G3-BF-A Field Data and Calibrated FEM Results**
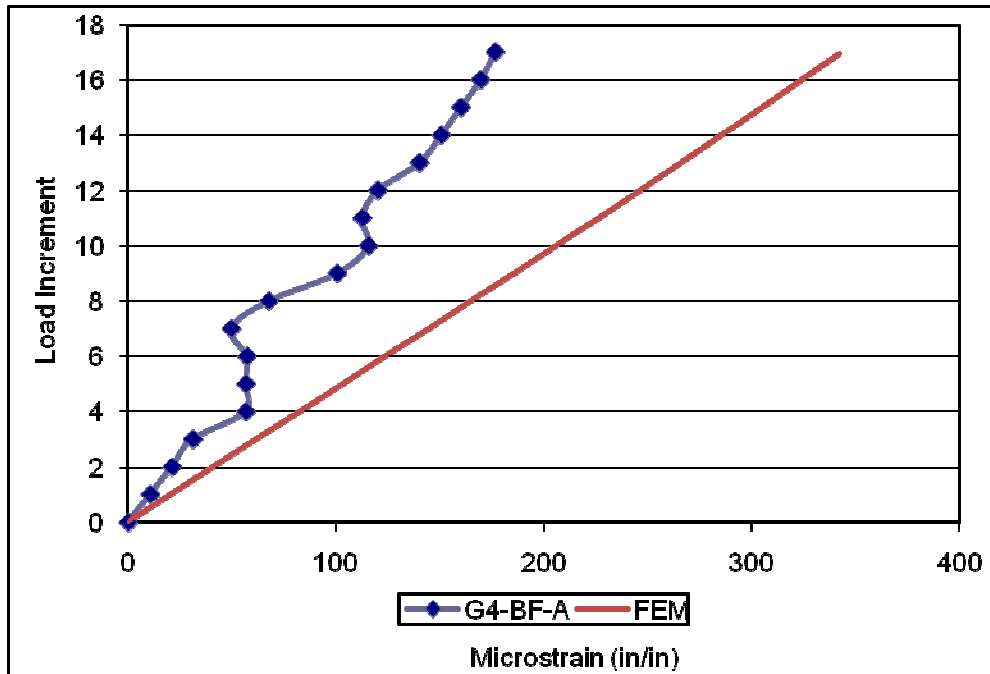
Figure 5.6   Gauge G4-BF-A Field Data and Calibrated FEM Results

5.2.1   Applied Loadings

During the destructive bridge test, the loading mechanism applied increments of loading, with each increment corresponding to an HS-20 vehicle. The location and relative magnitudes of the point loads used in the destructive test was mimicked in the FEA and the FEA loading was then incrementally increased using the Riks analysis method. The first step in the data analysis was then to determine the loading increments from the FEA that most closely corresponded to increments of HS-20 vehicle loadings, where each truck increment represents 72,000 lbs.

To do this, the load proportionality factors output from the Abaqus analysis were used. These factors represent the multiple of the base loads specified in the input file that are applied during each increment of the FEA. Knowing that each truck

increment represents 72,000 lbs and the sum of the loads given in the input file, the load proportionality factors corresponding to each increment of truck loading can be easily calculated by taking the ratio between these two quantities. The load proportionality factors output in the data file resulting from the Abaqus analysis are then evaluated to determine an FEA increment that closely matches each increment of truck loading. These FEA increments are then used to extract the output that is discussed below.

Table 5.9 shows the FEA results for the sum of the live load reactions at the girders compared to the truck loadings targeted during the destructive test. This data is only shown at key truck increments for conciseness. This FEA data was compiled by first summing the reactions at all support nodes at each end of each girder. The dead load reactions at each end of each girder were also summed. The difference between the total reaction forces and the dead load reaction forces was taken to obtain the live load reactions at each end of each girder. The FEA data in Table 5.9 then represents the sum of these eight (from the two ends of each of the four girders) live load reactions.

Increments	FEA Total Loads (lbs)	HS-20 Vehicle Loading (lbs)	Absolute Difference (lbs)	% Difference
1	74005	72000	2005	3%
2	144074	144000	74	0%
3	214154	216000	1846	1%
4	284153	288000	3847	1%
5	365677	360000	5677	2%
10	745432	720000	25432	4%
15	1084900	1080000	4900	0%
20	1442183	1440000	2183	0%
23	1659223	1656000	3223	0%
25	1797918	1800000	2082	0%
28	2015698	2016000	302	0%
30	2159906	2160000	94	0%

Table 5.9   FEA Live Load Reactions and Truck Loading Comparison

The percent difference values in Table 5.9 were calculated by taking the absolute difference between the calibrated FEA applied loads and the HS-20 vehicle loadings, and dividing the value by the vehicle loadings. This shows that the load increments in the FEA were small enough that the applied loading corresponds well to even multiples of the HS-20 vehicle loadings. These live load reactions from the FEA can also be compared to the load proportionality factors as an additional check of the accuracy of the data. The worst percent difference value is at the 1st and 10th increment at 3% and 4% respectively. From the 15th increment on, the percent difference is 0%.

5.2.2 Girder Reactions

Examining the reactions at the girders is essential to understanding the direction in which the forces are traveling throughout the structure. Thus, it was of interest to compare the reactions at each end of each girder and how this distribution changed throughout the range of loading. To accomplish this, the live load reactions at each end of each girder were found as described in the previous section. Because the gap elements allow uplift at each node corresponding to a support location, the vertical reactions at each individual node are either positive or zero. However, when the sum of the nine nodes at each end of each girder is taken at a given truck increment and the same value is calculated under dead load and subtracted from the total, the net result was negative in some cases. Specifically this occurs at increments 3 through 30 at the west end of Girder 3 and increments 1 through 28 at the west end of Girder 4. This has ramifications for calculating the percentage of load at each support as will be discussed below.

After the vertical reaction forces at each end of each girder were obtained, it was desired to then express this data in terms of the percentage of the load at each support. However, the negative (downward) reactions discussed in the previous paragraph necessitated some judgment being exercised in the way these percentages were calculated. Specifically, it was determined that the percentages would be generally calculated using the conventional approach of taking the reaction at a given point and dividing by the sum of all of the reactions at that increment. However, for the purposes of plotting the percentages of load carried by each reaction, the supports having a negative reaction would be plotted as zero. The consequence of this is that if one sums the percentages at a given truck increment in the graphs that follow, the percentages may exceed 100% in some instances (where the highest value is 101.4%). However, this approach is believed to best represent the physical behavior where supports experiencing uplift would carry no force. The small downward reactions, which never exceed 1% of the total load, can be thought of as a rounding error in the analysis.

The total percentage of the reactions at the east and west ends of the bridge were compared first. This showed that the total of the west reactions carried 57% of the

Reactions	Transverse Distance	Longitudinal Distance	Direct Distance
Girder 4 - East Reaction	17'-0"	20'-7"	26'-9"
Girder 1 - West Reaction	7'-0"	36'-8"	37'-4"
Girder 3 - East Reaction	9'-0"	36'-7"	37'-9"
Girder 2 - East Reaction	1'-0"	52'-7"	52'-7"
Girder 2 - West Reaction	1'-0"	52'-8"	52'-8"
Girder 1 - East Reaction	7'-0"	68'-7"	68'-11"
Girder 3 - West Reaction	9'-0"	68'-8"	69'-3"
Girder 4 - West Reaction	17'-0"	84'-6"	86'-4"
Average - East Reactions	8'-6"	44'-7"	46'-6"
Average - West Reactions	8'-6"	60'-8"	61'-5"

Table 5.10   Distances from Centroid of the Loads to Girder Reactions

live loads and the remaining 44% traveled to the east reactions. These percentages were consistent throughout the loading range.

Before further discussing the distribution of the load to the various reaction points, it is helpful to consider the distances (transverse, longitudinal, and direct distances) between each of the eight girder reactions and the centroid of the loading mechanism, which are listed in Table 5.10. Here the reactions are listed in order from those having the shortest direct distance (west reaction of Girder 1) to the longest direct distance (east reaction of Girder 4) to the loading centroid. Figure 5.7 spatially represents these distances, where the asterisk in the figure denotes the centroid of the loading mechanism. The "x" symbols on the figure indicate the jack positions. The girder number and reaction is given after the measurement in Figure 5.7. For example, one of the measurements reads 29'-6" G4-E, meaning the east reaction at Girder 4 is 29'-6" away from the centroid of the loading mechanism.

Due to the skew of the bridge, the east supports of Girders 3 and 4 and west
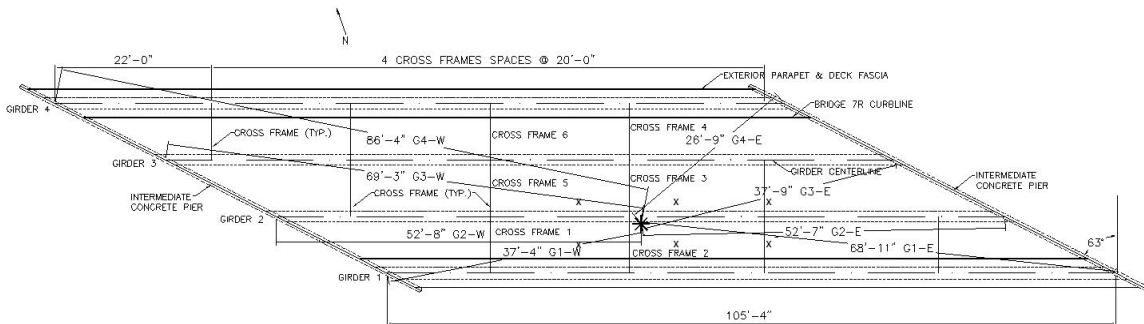
Figure 5.7   Distances from Centroid Loads to Girder Reactions

82

supports of Girders 1 and 2 are closest to the centroid of the loading. At the bottom of Table 5.10 the average of the east and west reaction direct distances (46'-6" and 61'-5", respectively) are listed. One may suspect that the average west girder distances would be closest to the centroid of the loading based on the higher percentage of live load resisted by these reactions (mentioned above), but this is not the case. Instead, the reactions at each girder must be examined.

In order to understand the load distribution in the bridge as well as the variations in load distribution with increasing load, graphs of the percentage of live load vs. truck increments were created. Figure 5.8 displays the percentage of live load carried by each of the four girders. Here it is shown that Girder 1 carried the largest percentage of live load by a significant margin, resisting approximately half of the applied loading throughout the loading range. Girder 2 and 4 resisted the same and second largest percentage of live load during the first 6 increments. After the sixth increment Girders 1 and 4 gradually carry fewer loads as the load is increased and more load is distributed to Girders 2 and 3. Figure 5.8 also shows that at increment 27 there is a local maximum in the percentage of load carried by Girder 2 and local minima in the percentage of load carried by Girders 1 and 4. These changes in load distribution indicate localized yielding in the structure that will be evaluated in greater detail in Section 5.3.

Figures 5.9 and 5.10 show graphs similar to the percent of live load vs. truck increment graph in Figures 5.8 except these graphs consider the reactions at each end of each girder. Specifically, Figure 5.9 graphs the west reactions at each girder and Figure 5.10 graphs the east reactions at each girder. These show that the west support of Girder 1 carried the majority of the live loads, by over a 29% margin, during each increment.
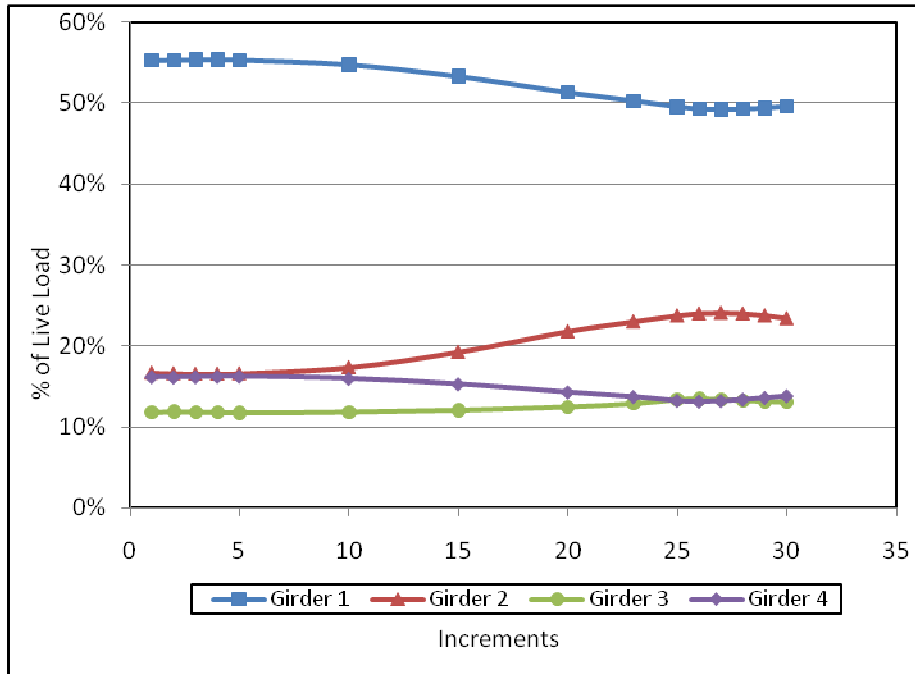
**Figure 5.8   Percent of Loading Carried at each Girder Reaction**
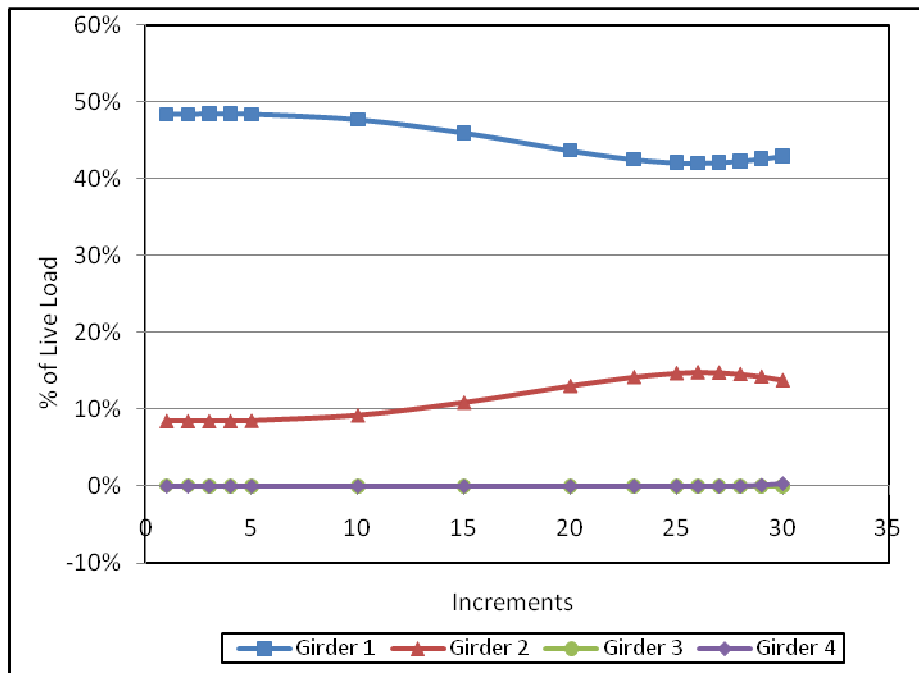
Figure 5.9   Percent of Loading Carried by West Supports

84

The results from these figures shows that the loading initially traveled longitudinally in that the west support of Girder 1 carried the highest load and this support had the shortest longitudinal distance to the centroid of the loading (as shown in Table 5.10), but not the overall shortest distance. However, a significant amount of transverse distribution of force is also exhibited by the fact that the east support of Girder 4, which is the support closest to the centroid of the loading, carries the second highest percentage of loading up to 23 trucks. It should be recalled though that these percentages are low relative to the reaction at the west end of Girder 1. These results are not surprising considering the load transfer mechanisms available and the relative distances to each support. The east end of Girder 4 is closest to the loading centroid, but the loading must travel through Cross Frames 3 and 4 (see cross frame labeling in Figure 5.7) and/or the concrete deck to reach this support. Conversely, the loading is transferred directly from the deck to Girder 1.

Specifically comparing the reactions at the west end of the bridge, it is seen that the majority of the load is carried by Girders 1 and 2 throughout the loading range and all of the load is carried by these girders during truck increments 3 through 28.   This is explained by considering that these two supports are closest to the centroid of the loads and the torsion caused by the eccentric (relative to the transverse centerline of the bridge) loading. It is also shown in Figure 5.9 that as the load distributed to the west end of Girder 1 begins to decrease, there is a corresponding increase in the load distributed to the west end of Girder 2. At increment 1 the percent of loading carried at the west end of Girder 1 is 48% and 8% is distributed to the west end of Girder 2. At increment 30 the percent of loading carried at the west end of Girder 1 is 43% and 14% at the west end of

Girder 2. Thus, the percent of the load at Girder 1 decreases 5% between increments 1 through 30 and increases 6% at Girder 2. The fact that these two percentages do not exactly match is primarily due to rounding error combined with a slight change in the percent of load carried by Girders 3 and 4. These results again suggests that the load is first distributed longitudinally; the load is then redistributed transversely as yielding occurs.

As shown in Figure 5.10, the loading is distributed between the east girder reactions much more evenly compared to the west girder reactions. This is attributed to the fact that the east supports that are closest to the centroid of the loading also require the greatest transverse distribution of loading, making these supports (at Girders 3 and 4)
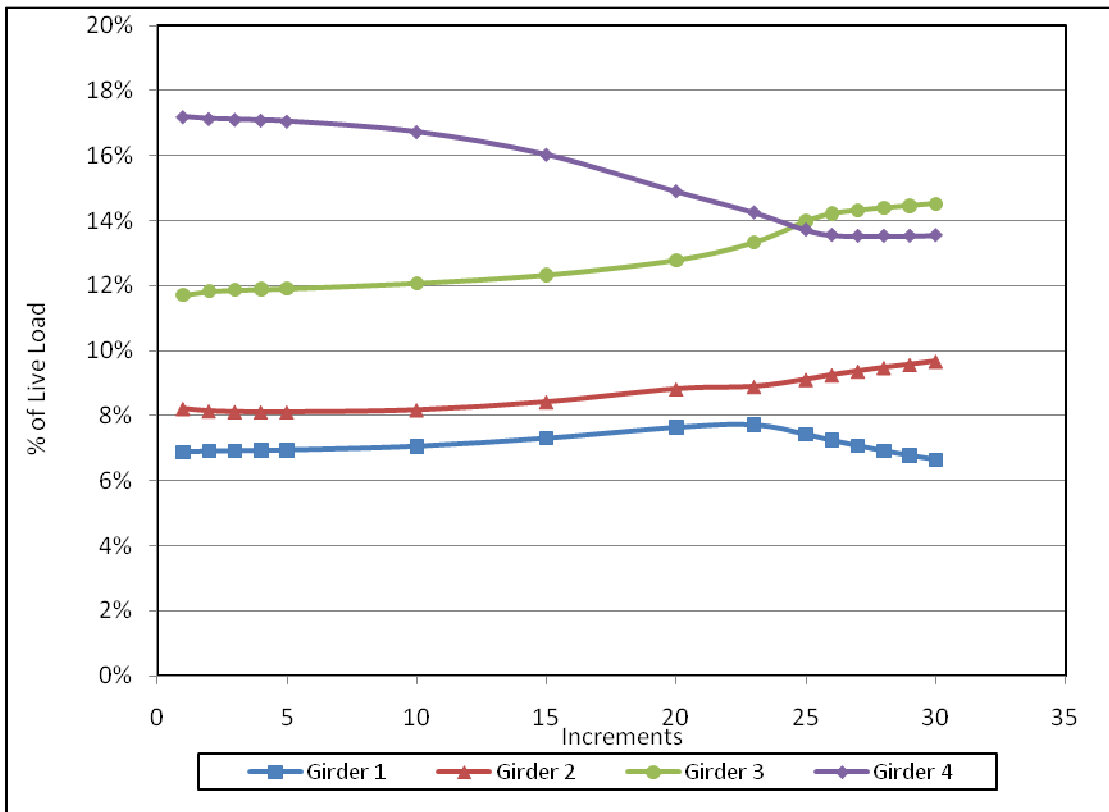

Figure 5.10   Percent of Loading Carried by East Supports

carry a less significant majority of the loading. For example, at increment 1 the percentage of the total live load resisted by each of the east supports is 17% at Girder 4, 12% at Girder 3, 8% at Girder 2 and 7% at Girder 1. The percentage of loading at Girder 4 then decreases throughout the loading range. Up through increment 23, this decrease is shown to be the result of redistribution of this load to the east supports of Girders 1, 2, and 3. The amount of load redistributed to each of these three girders is dependent upon the location of the girder relative to Girder 4, that is, more load is redistributed to Girder 3 versus Girder 2 for example. Beyond increment 23, the percent of the live load carried by Girder 1 also begins to decrease, while the percent of live load carried by Girders 2 and 3 continues to increase. At increment 30, Girder 3 carried the most loads of the east supports, resisting 15% of the live load. The distribution of the live load at the other 3 east supports at increment 30 was 14% at Girder 4, 10% at Girder 2, and 7% at Girder 1. This shows that in this case the distribution of loading between the various east supports becomes more equal at the higher load levels.

5.2.3 Redistribution of Loadings

The progression of yielding and plastification that occurred in the bridge must be examined to understand the load redistribution shown in the previous section. The girders in Bridge 7R were comprised of ASTM-A7 steel. The minimum specified yield strength of ASTM-A7 is 33 ksi. However, the yield strength of the steel input in the FEA is input as 36 ksi as this was the initial assumption of the minimum specified yield strength. Given that these two values are not appreciably different and that the fact that the actual yield strength will be higher than the specified minimum, this discrepancy is not thought to be significant. However, obtaining the actual yield strength and other

material properties via coupon testing would be highly desirable in future studies to provide more accurate FEA input. For the purposes of interpreting the FEA results, "yielding" is quantified as when the von Mises stress in an element exceeds 36 ksi. A girder is considered "plastified" when the von Mises stresses in the bottom flange and the web of any girder cross section have exceeded 36 ksi.

Table 5.11 summarizes the sequence of yielding and plastification that occurs in the cross frames and girders in the FEA. Here the "sequence" number is simply meant to convey the order in which the various types of yielding occurred and to cross-reference these events with their visual depictions shown in Figures 5.11 through 5.13, which are discussed below. A total of 15 areas of yielding and 2 areas of plastification were discovered. In summary, the extent of yielding included the following: the bottom chords of five different cross frames, the inclined chords of two of these same cross frames, shear yielding at the end of one girder, yielding of the bottom flanges of all four girders, flexural yielding progressing into the web of three girders, and plastification of two girders.

Shear yielding is distinguished from flexural yielding by viewing the component stresses in the elements. Specifically, the longitudinal stresses in many of the elements exceeded the yield strength of the material and this could be readily observed through the post processing software. Table 5.11 primarily reports flexural yielding, including the first flexural yielding that occurs at 19 trucks, when complete flange cross-sections yield flexurally, and when the flexural yielding progresses into the web. All entries in the table related to girder yielding are flexural yielding unless noted otherwise. To assess shear yielding, the magnitudes of the various stress components were assessed

Sequence	Truck Increment	Yielding Description Area	Location
1	12	1st element to yield	Bottom Chord of Cross Frame 2
2	13	2nd cross frame member to yield	Bottom Chord of Cross Frame 3
3a	14	3rd cross frame member to yield	Bottom Chord of Cross Frame 1
3b	14	1st girder web yielding, in shear	Girder 1, See Figure 5.9, 5.2 ft from the west support
4	15	4th cross frame member to yield	Bottom Chord of Cross Frame 5
5	16	5th cross frame member to yield	Middle Chord of Cross Frame 2
6	19	1st bottom flange yielding	Girder 2, 45.2 ft from the west support
7	20	Bottom Flange Cross-Section Yielding	Girder 2, 50.6 ft from the west support
8	21	2nd web girder yielding	Girder 2, 51 ft from the west support
9a	23	6th cross frame member to yield	Middle Chord of Cross Frame 1
9b	23	Bottom Flange Cross-Section Yielding	Girder 1, 42.6 ft from the west support
10	25	7th cross frame member to yield	Bottom Chord of Cross Frame 6
11	26	Bottom Flange Cross-Section Yielding	Girder 3, 66.6 ft from the west support
12	27	3rd web girder yielding	Girder 3, 56.9 ft from the west support
13	28	1st plastic hinge	Girder 2, 51 ft from the west support
14a	30	Bottom Flange Cross-Section Yielding	Girder 4, 20.4 ft from the west support
14b	30	2nd plastic hinge	Girder 1, 36 ft from the west support

Table 5.11   Sequence of Yielding and Plastification in FEA

in several of the elements thought to be experiencing shear yielding and it was found that

the shear stress comprised at least 84% of the total stress (summing the two in-plane

stresses and the shear stresses) in these elements. The yielding that occurred at the

bottom flanges over the supports was neglected when compiling the data in Table 5.11

and Figures 5.11 through 5.13 because this yielding is fairly isolated (never extending

through the web depth). However, the shear yielding at the end of one girder that is

mentioned above is included because this yielding is much more significant, extending

through the full depth of the web and beyond the 22.5 ft distance between the support and

the nearest cross frame location (as will be shown below). Figures 5.11 through 5.13

present an upside-down view of Bridge 7R from the FEA. Thus, Girder 1 is at the top of

the figures and Girder 4 is at the bottom of the figures and the bottom flanges are towards

the top of the figures and the top flanges are towards the bottoms of the figures. The
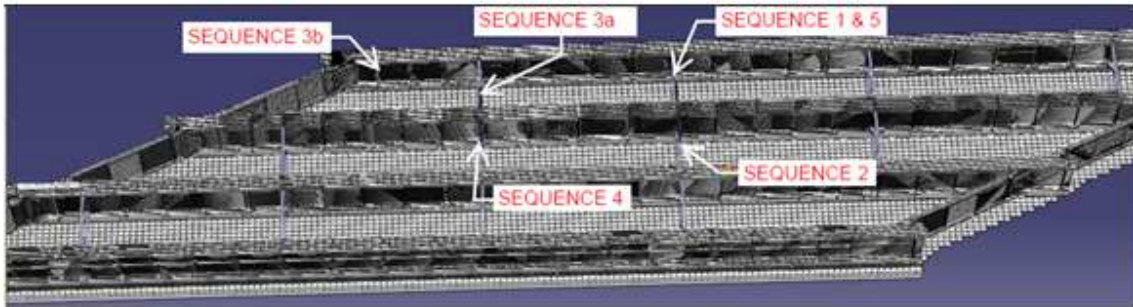
Figure 5.11   16 HS-20 Truck Yielding Pattern
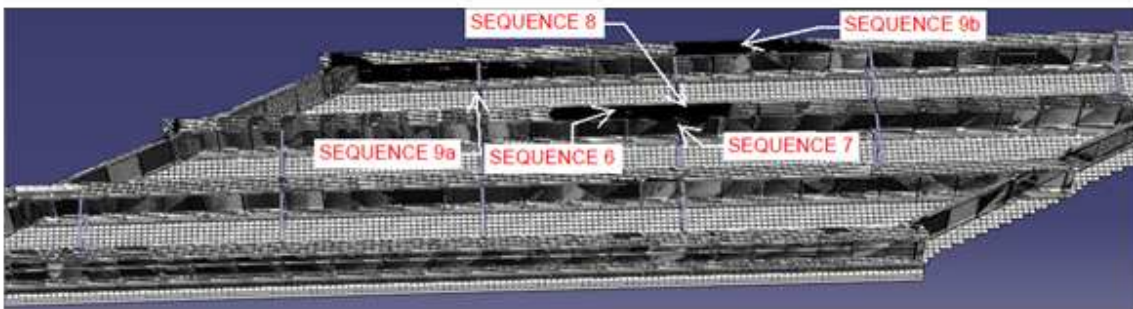
Figure 5.12   24 HS-20 Truck Yielding Pattern
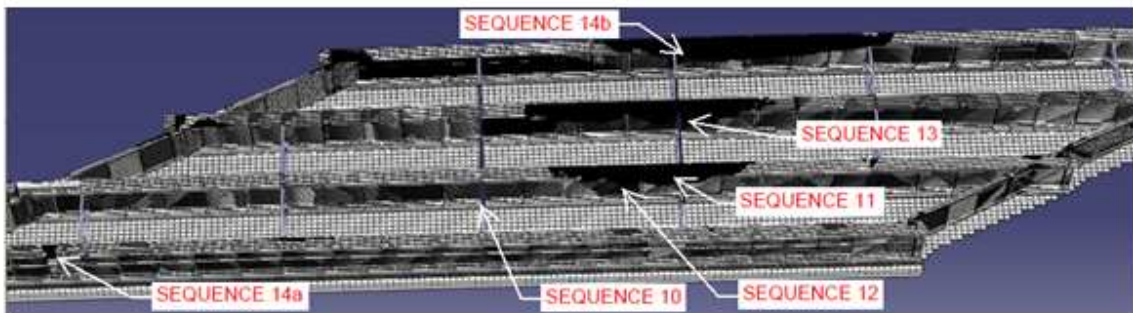
Figure 5.13   30 HS-20 Truck Yielding Pattern

girders are comprised of the denser mesh (which therefore appears darker in color) with the larger square elements represent portions of the concrete deck that are visible between the girders; the light-colored lines perpendicular to the girders are the cross frames. Elements that have yielded are filled black. Figure 5.11 displays the predicted yielding at a load of 16 HS-20 trucks and the yield described by sequences 1 through 5 as defined in Table 5.11. The majority of the yielding that occurs during these sequences occurs in the cross frames. Figure 5.12 displays a similar figure corresponding to 24 HS-20 trucks and sequences 6 through 9. A significant amount of the yielding that occurs during increments 6 through 9 occurs in the girders of the bridge. Figure 5.13 corresponds to 30 HS-20 trucks and sequences 10 through 14. All of the additional yielding that occurs during these sequences occurs in the girders, including the development of two plastic hinges.

The first element to experience yielding was located at the bottom chord of Cross Frame #2 during the 12th truck increment. The location of the cross frame can be found in Figure 5.11 where the label of "Sequence 1" is pointing towards the cross frame. In all cases, the labels in these figures point towards the location where yielding in that member initiates. The first girder yielding occurred during the 14th truck increment in the web of Girder 1. This yielding was due to shear and is located adjacent to the west reaction at Girder 1. This yielding is shown in Figure 5.11 where the label of "Sequence 4" is pointing to the yielded area. It was not surprising to see shear yielding at this location considering the adjacent reaction carried nearly 50% of the live load (as discussed in the previous section).

The first flexural yielding of the girders occurred in Girder 2 at 19 trucks (sequence 6). From this level of loading through the end of the loading range, the yielding spreads longitudinally, transversely, and vertically throughout the girders. The spread of plasticity is extensive in the longitudinal direction, where the lengths over which the bottom flanges of Girders 1, 2, 3, and 4 are yielded are 24.2, 20.91, 16.8, and 1.3 ft respectively.

The centroid of the loading is near the location where the first plastic hinge occurred during the 28th truck increment, which is also labeled as sequence 13. The longitudinal position of the centroid is also nearly in line with Cross Frames 2, 3, and 4, with Cross Frames 2 and 3 being most proximate to the centroid. This explains why these two cross frames are the first members to yield. Also, 3 out of the 7 cross frame members to yield are in Cross frames 2 and 3.

Knowing the progression of yielding that occurs can help explain the trends in load distribution that were presented in the previous section. For example, the west support of Girder 1 was shown to carry the vast majority of the applied loading (see Figure 5.9), but this begins to significantly decrease between increments 10 and 15. From viewing the progression of yielding, it is clear that this is due to shear yielding throughout this end of this girder. A correlation between sequence 9b where the bottom flange of Girder 1 begins to yield at 22 trucks and the beginning of a decrease in the east reaction of Girder 1 (see Figure 5.10) is also observed. Similarly, there is a correlation between the first plastic hinge forming in Girder 2 at 28 trucks during sequence 13 and a decrease in the west reaction of Girder 2 (see Figure 5.9) at this same load level. The

following section will more closely evaluate how the combined state of yielding resulted in the ultimate capacity of the structure being achieved.

5.3 FEA Termination

The ultimate capacity of the calibrated FEA was exactly 30.22 HS-20 trucks. After this point in the analysis, the applied load continuously decreased. It is known from the analysis of the results that was presented above that the ultimate capacity was the result of excessive yielding in the structure (rather than any stability-related issues). However, the exact sources of yielding that limit the capacity of the structure are not readily apparent.

Conceptually the ultimate capacity of this model (where all members other than the girders are modeled as linear-elastic elements) could be considered as the load when all four girders have reached their design capacity or the load when all four girders have plastified. Evaluating the concept of ultimate capacity based on design capacity would mean that the ultimate capacity would be when all four bottom flange cross-sections have yielded. This occurs at 29.56 trucks. Thus, the structure demonstrated additional capacity beyond this level of loading, reaching an ultimate capacity of 30.22 trucks. While this may not seem like an appreciable difference in loading, it is considered that in Ross' (2007) results, it was demonstrated that all four girders could sustain load up through forming plastic hinges (which he quantified as 80% of the web depth having stresses exceeding the yield stress).

However, this level of plasticity is not achieved in the present model, with only two girders have plastified at 30 truck increments. This suggests that the ultimate capacity is being limited by the ability of the system to redistribute forces. Furthermore,

Cross Frame #	Location	1 Element	2 Elements	3 Elements
1	Top connection of CF 1 at Girder 1	13	13	20
	Top connection of CF 1 & 5 at Girder 2	18	19	27
	Bottom connection of CF1 at Girder 1	24	25	27
	Bottom connection of CF 1 & 5 at Girder 2	26	27	29
2	Top connection of CF 2 at Girder 1	14	18	18
	Bottom connection of CF 2 & 3 at Girder 2	20	21	27
	Top connection of CF 2 & 3 at Girder 2	20	23	24
	Bottom connection of CF2 at Girder 1	23	25	27
3	Bottom connection of CF 3 & 4 at Girder 3	28	28	29
4	Top connection of CF 4 at Girder 4	29	30	30+
5	Bottom connection of CF 5 & 6 at Girder 3	29	30	NA
6	Top connection of CF 6 at Girder 4	30	30+	NA
	Bottom connection of CF 6 at Girder 4	30	30+	NA

Table 5.12   Occurrence of Breakdowns

since (again) the concrete deck and cross frame members are modeled as linear elastic elements, the only possible attribute of the system that can be creating this condition is that the elements surrounding the cross frame-to-girder connection have yielded.

Each of the ends of the cross frame members was connected to a node on the girders, which are in turn surrounded by four elements. The progression of yielding in these elements was analyzed based on the premise that the more elements adjacent to the cross frame connection that yield, the less loading that will be transferred to the cross frame. The summary of this analysis is presented in Table 5.12. Overall elements surrounding 14 connection points between the cross frames and girders had yielded. The location of each of these cross frames can be seen in Figure 5.14. It should be noted that, because of the way the cross frames are connected directly to the girders in the model, adjacent cross frames in the same bridge cross-section will share a common connecting node (for example the chords of Cross Frames 1 and 5 both connect to the same nodes on Girder 2). The entries in the table are organized by cross frame members but since two cross frames can connect to a girder, the yielding maybe shown at a different cross frame. The three columns to the right of the table display the truck increment at which the given

94
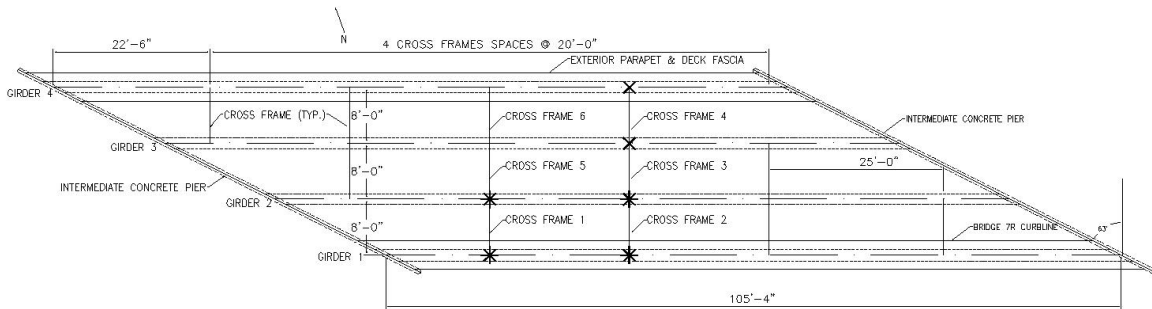
Figure 5.14   Cross Frame Locations

number of elements has yielded. When all four elements yielded was not evaluated because it was believed that the yielding of three elements significantly compromised the connection, but this hypothesis was not rigorously evaluated. The "NA" entries in the table indicate that the listed number of elements does not yield prior to the ultimate capacity of the structure being achieved. Lastly the 30+ entry denotes yielding occurred at loads between 30.00 and 30.22 truck increments.

Viewing the data presented in Table 5.12 in relationship to the geometry of the structure (see Figure 5.14) suggests that the yielding along the line of cross frames formed by Cross Frames 2, 3, and 4 caused the ultimate capacity of the structure to be achieved. This line of cross frames is the one closest to the centroid of the loading and is a means of transferring the applied forces to the west support of Girder 4, which initially carries the second highest percentage of the live load. At least one end of each of the members in Cross Frames 2, 3, and 4 had yielding in three or more of the four elements that it connected to. Figure 5.14 shows this with the asterisk and X at the location were the cross frame connects to the girders. An X denotes that one out of the two cross frame members of the cross frame had three or four elements that yielded and the asterisk

95

denotes when both the ends have three or more elements that has yielded. Furthermore, the last discontinuity (yielding in three of the elements surrounding a connection) to occur in the FEA was located at the connection between the top chord of Cross Frame 4 and Girder 4. Immediately after this final discontinuity occurred, the loading in the model began to decrease at the next FEA increment. Thus, it is believed that at this point transverse redistribution through this cross section of the bridge and to the west support of Girder 4 became sufficiently limited to cause the ultimate capacity of the bridge being achieved.

5.4   Conclusion

The calibrated model in this research predicted an ultimate capacity of 30.22 HS-20 vehicles. At this level of loading, plastic hinges had formed in Girders 1 and 2, the hinge in Girder 2 forming at 28 trucks and the hinge in Girder 1 forming at 30 trucks. This would necessitate that additional live loads redistribute to Girders 3 and 4, particularly at the west ends of the girders where Girders 1 and 2 carried all of the loading between increments 3 and 28. The fact that Girder 4 was experiencing uplift up to 28 increments of loading and then begins to resist the applied loads combined with the observations that: (1) the plasticity in Girder 3 spreads more to the west than to the east after yielding of this flange originates and (2) that the flange yielding in Girder 4 occurs between the west support and the adjacent cross frame suggests that the structure was attempting to redistribute loading to the west reactions of these girders. However, the mechanisms for this redistribution to occur became limited by yielding at the girder to cross frame connections. The most severe example of this was in the line of cross frames (Cross Frames 2 through 4) located nearest to the longitudinal position of the centroid

and the plastic hinge locations in Girders 1 and 2, as discussed in the previous section. Therefore, it is believed that the ultimate capacity of the bridge was reached because the loadings could not be efficiently redistributed.

Chapter 6

CONCLUSIONS

6.1   Summary

The focus of this thesis was to study the reserve capacity of a skewed steel I-girder bridge up to its ultimate capacity. In today's method of designing bridges, the strength of each member in the system is considered individually and redistribution of loading from one girder to another is not considered. A system-level approach of examining the bridge accounts for the redistribution of loadings between girders. This redistribution of loading has proven in this research to allow for significantly greater capacity than is reflected in the current design code predictions based on strength of individual members.

This research involved both destructive field testing and FEA. The destructive field test was described in Chapters 3 and 4 and this present chapter concludes with recommendations for future destructive field tests. During the field test, the equivalent of seventeen HS-20 vehicles stacked on top of one another (or an HS-340 vehicle) was applied to the single-lane, simple span bridge having a span length of approximately 100'. As a result, no yielding was recorded in any of the girders. Based

on the recorded strains and estimates of the dead load from the FEA, it is estimated that a maximum of 30.4 ksi of flexural stress was generated at midspan of the bottom flange of Girder 2, which was the most-heavily loaded girder. The minimum specified yield strength of the girders was 33 ksi. More information on the recorded strain gauge data for the girders can be found in Section 4.3. Yielding did occur at one of the strain gauges that were attached to the bottom chord of a cross fame. This yielding appeared after the 10th increment of loading (corresponding to 10 HS-20 vehicles) was applied. For additional information about the cross frame strain data see Section 4.4.

A finite element analysis (FEA) was used to examine the ultimate capacity of Bridge 7R based on calibrating an existing model created by Ross (2007) using the field test results. As a result of the calibration process, the elastic modulus of the concrete was increased 150% (to a value of 574.5 ksi) over what was assumed in the initial model. Section 5.1 explained how the calibrated model was chosen and Sections 5.2 through 5.4 discussed results from the model. As a result of the model, the ultimate capacity of the bridge (for the assumed loading configuration) was predicted to be 30 HS-20 trucks. At this level of loading, plastic hinges had formed in two of the four girders and insufficient mechanisms for load transfer to the remaining two girders existed due to extensive yielding of the connections between the cross frames and the girders. The following section compares the ultimate capacity results from the calibrated FEA to the design codes in order to understand the amount of addition capacity the system-level approach offers compared to the design codes.

6.2   Bridge 7R Ultimate Capacity in Comparison to M_p

A key objective of this thesis was to evaluate the ultimate capacity of Bridge 7R. This was primarily accomplished by using the destructive testing results to calibrate a FEM of the bridge and then evaluating the ultimate capacity predicted by the model. Sections 5.2 through 5.4 have discussed these FEA results. Additionally, the system capacity was calculated based on the girder capacities given in the AASHTO LRFD Bridge Design Specifications (2010) in Section 3.4. The focus of this present section is to compare the ultimate capacity observed in the calibrated FEA to that predicted based on AASHTO Specifications to demonstrate the conservatism of these specifications and the tremendous opportunities available for improving the efficiency of routine bridge design by considering the system capacity of structures as opposed to the current approach of calculating capacities based on the strength of individual members.

Since modern design codes (e.g., AASHTO 2010) only predict the strength of individual members, the AASHTO system capacity was taken as the summation of the strengths of the four girders of the bridge cross-section. For the slender web girders in this structure, this capacity is equal to the yield moment of the girders. Using this approach and neglecting load factors, it was shown in Section 3.4.2 that the ultimate system capacity of Bridge 7R was 25.3 AASHTO HS-20 trucks (totaling 1,822 kips) based on the position of the loading mechanism. These same calculations were repeated considering (1) a moment capacity of M_p to give an upper-bound system capacity of 32.2 HS-20 trucks and (2) the load factors and the worst-case position of the loading (which differed only slightly from that of the loading mechanism) in Section 3.4.3 to predict an ultimate system capacity of 10.3 AASHTO HS-20 vehicles (totaling 742 kips).

Table 6.1 shows the progression of flexural yielding (in terms of when a single element first yields and when all the elements in any bottom flange cross-section of a girder yields) in the FEA results. The locations of this yielding were generally at midspan of the girders, with the exception of the yielding in Girder 4, which occurred near the west quarter-span point, 19' 3" from the support. The calibrated FEA predicted the first flexural yielding (in Girder 2) under a load of 19 HS-20 vehicles, while AASHTO predicts this should occur at 12 HS-20 vehicles discounting load factors and 5 HS-20 vehicles including load factors. If the ultimate system capacity is taken as the load causing the bottom flange of all four girders to yield (the stress state corresponding to M_y), the system capacity is 30 trucks.

Comparing this FEA system capacity to the capacity (of 25 trucks) predicted using the sum of the AASHTO girder strengths (discounting load factors); this is 5 additional HS-20 trucks (or 20%). (If the FEA results are compared to the sum of the AASHTO girder strengths and load factors are included, the percent increase is 300%). This demonstrates that there is additional system strength (assuming adequate strength of the concrete deck) even beyond what is predicted based on what are fairly liberal, by today's standards, hand calculations of the system capacity. These results are in line with previous studies (Bechtel 2008) demonstrating there is significant potential available for economizing bridge design by developing rational three- dimensional design procedures. One specific reason for the increased strength is that there is also a longitudinal spread of plasticity (particularly in skewed girders) that is not accounted for in these rather simplistic calculation methods. Capturing this behavior in a theoretical framework is a suggested avenue for future research.

Girder	Load causing single element flexural yielding (in HS-20 truck increments)	Load causing bottom flange cross-section flexural yielding (in HS-20 truck increments)
2	19	20
1	22	23
3	24	26
4	27	30

Table 6.1   Number of Trucks that caused Flexural and Cross-Sectional Yielding

Furthermore, the system has additional capacity beyond when the bottom flanges of all girders yield because at this point the plasticity is still restrained. While, due to rounding, it may first appear that the yielding of the bottom flanges of all four girders coincides with the ultimate capacity in the FEA, the former actually occurs at a load of 29.56 HS-20 trucks while the latter occurs at a load of 30.22 HS-20 trucks (54 FEA increments later). It was previously discussed (in Sections 5.3 and 5.4) that this ultimate capacity is thought to be limited by plastic hinges in the two most heavily loaded girders combined with yielding at the cross frame connection points limiting the mechanisms available for redistributing the load from these girders. Thus, through alterations to the design of the transverse members, the system capacity could be even greater.

6.3   Recommendations for Future Destructive Bridge Tests

The loading mechanism (described in Chapter 3) proved to be an efficient method of loading the bridge and a significant improvement over that used in the research team's previous work (Quinn 2005). It allowed for the loads to be applied in a fairly concentrated, well-defined, and controlled manner. However, the seventeen HS-20 vehicles (totaling 1,224 kips) applied onto the structure was not enough to cause yielding in any of the steel plate girders. Increasing the loading beyond this point was not

possible due to safety concerns related to the forces in the coil rods approaching their capacity

Devices similar to the loading mechanism used in this study are recommended for application in future destructive bridge test, but improvements to this system would be advantageous. One such improvement that could be made includes incorporating load cells to record the actual loadings induced at each load point (as opposed to strain readings at a sampling of the reaction points of the loading mechanism as done in this research). Another important improvement that should be made is to improve the prediction of the desired loading on the structure (through the FEA techniques described herein for example) and design the loading mechanism accordingly. Had this been done in the current research, additional coil rods could have been provided to observe yielding in the girders.

APPENDICES

Appendix A

Manually Recorded Field Test Data

As mentioned in Section 4.1, nearly half the strain gauge data was not retained due to a malfunction of one of the data acquisition systems. The strain data from Gauges G2-BF1-B and G2-BF2-B (see Section 4.1 for a description of the location of these gauges) was not retained due to this malfunction. However, during testing, data from these two gauges was manually recorded. The readings were taken near the end of each loading increment and the corresponding time stamps noted, but these time stamps do not correspond to those systematically selected in the final data analysis. Table A-1 displays the microstrain data for each gauge and the corresponding time stamp at which the data was recorded. Because these time stamps differ from those used in the remaining gauges, this data was not ultimately considered in the data comparisons; however, it is presented in here in the event that it becomes useful in future work.

Increment	Time Stamp	G2-BF1-A	G2-BF2-A
0	0	0	0
1	72	51	55
2	132	83	90
3	204	129	135
4	296	210	216
5	370	255	259
6	460	276	280
7	550	265	267
8	640	295	297
9	744	389	387
10	816	465	462
11	896	529	525
12	1096	500	495
13	1200	573	569
14	1290	631	628
15	1396	656	669
16	1510	694	731
17	1652	770	843

Figure A-1   Microstrains for Gauges G2-BF1-B & G2-BF2-B

Appendix B

Increments 4-17 Coil Rod Strain Time History Graphs

Section 4.2 graphed the strains in each of the five coil rods versus time for increments 1-3. The contents in this appendix contain similar strain graphs from increments 4-17. The increments of loading are discussed in Section 3.1.
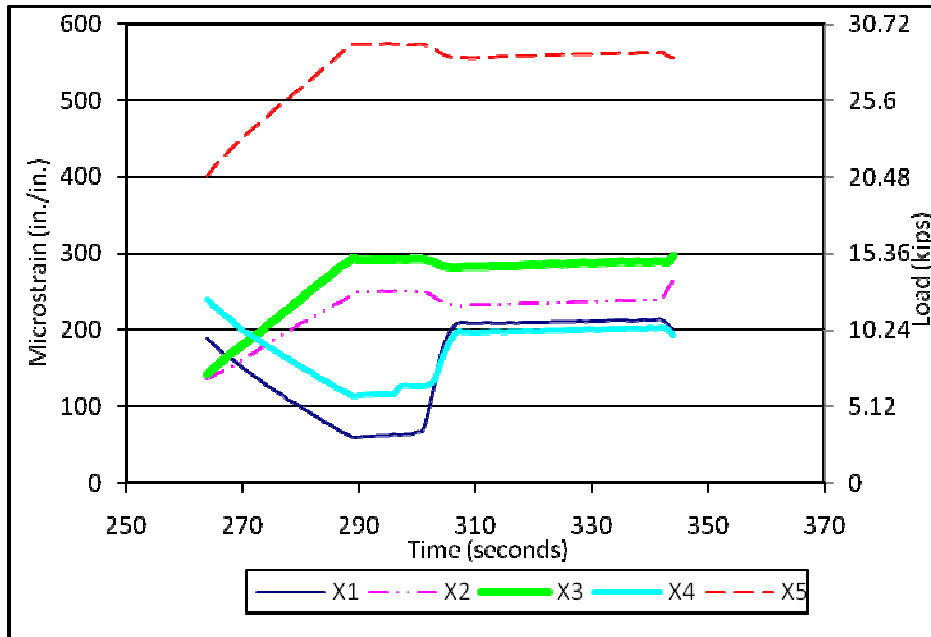
Figure B-1   **Increment 4, Time History Graph**
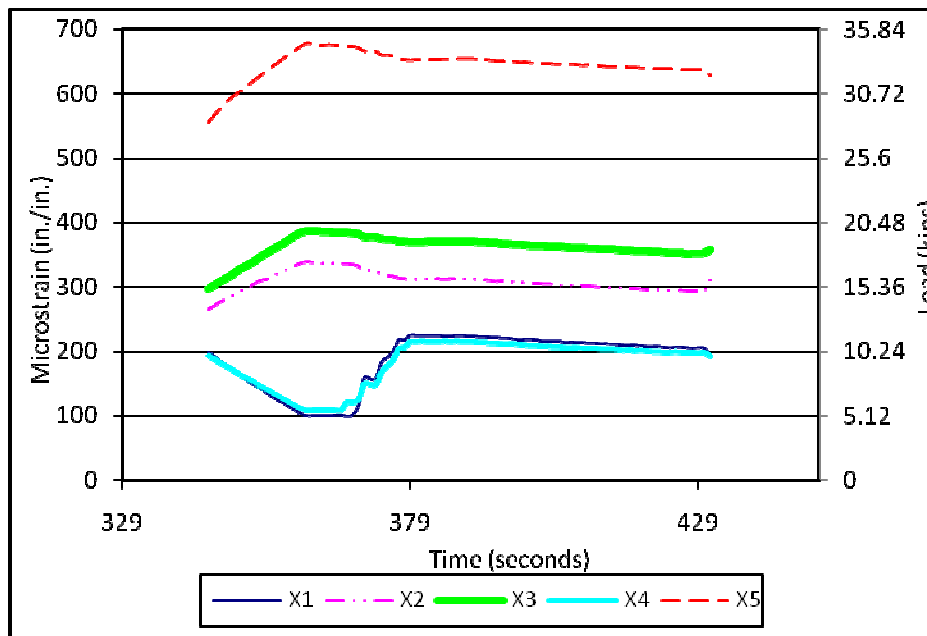
Figure B-2   **Increment 5, Time History Graph**
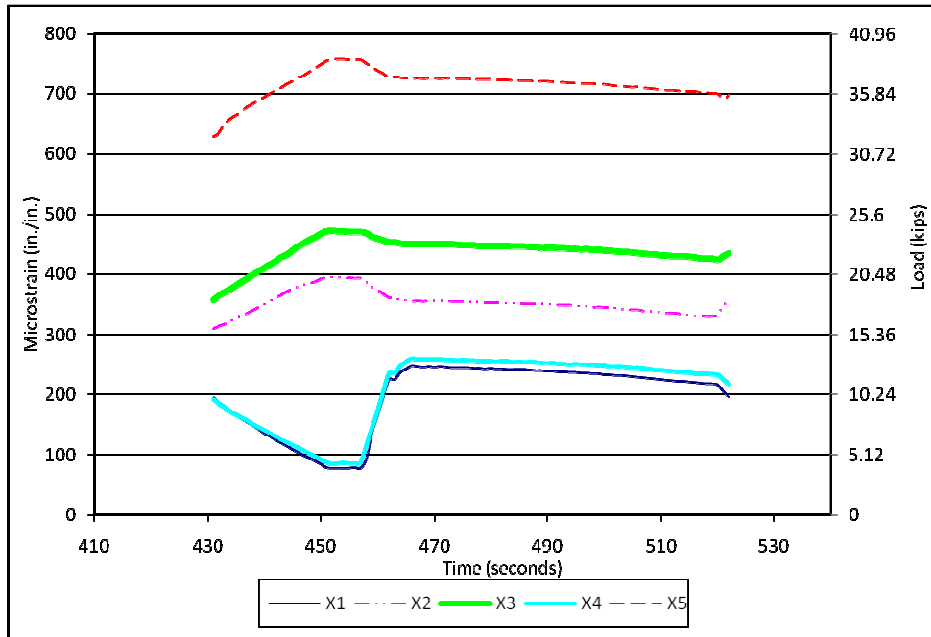
Figure B-3　　　　　　　Increment 6, Time History Graph
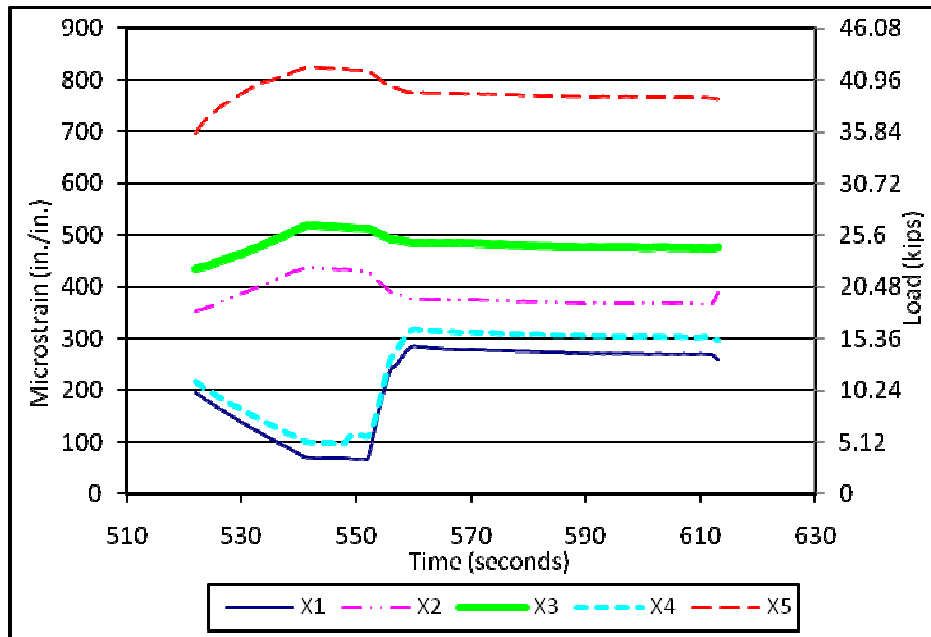
Figure B-4　　　　　　　Increment 7, Time History Graph
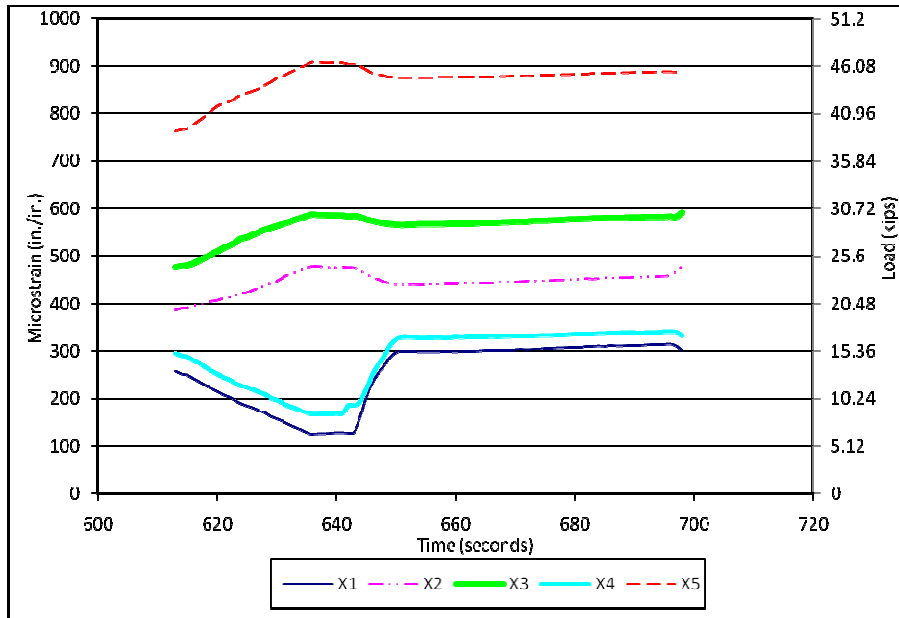
Figure B-5   Increment 8, Time History Graph
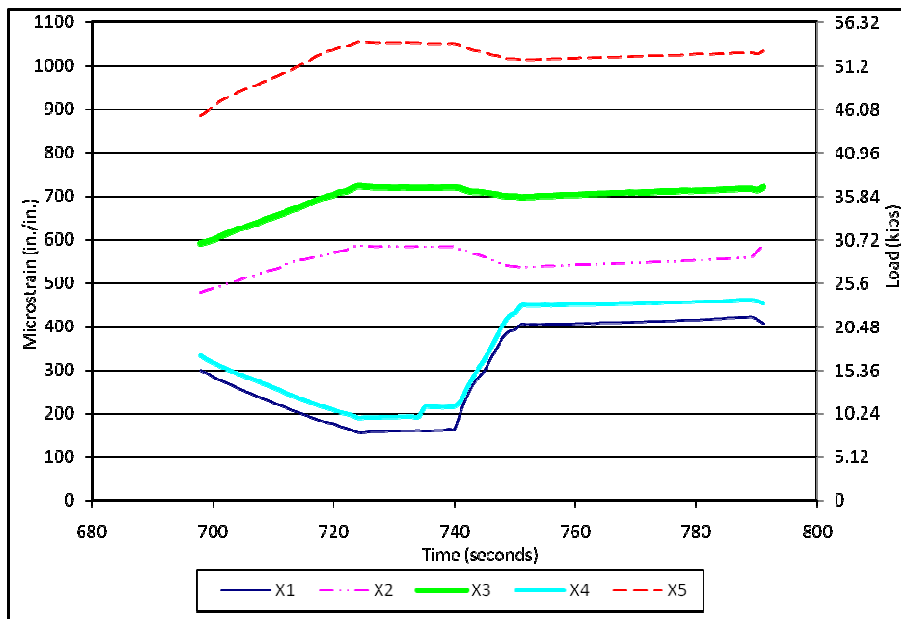
Figure B-6   Increment 9, Time History Graph

109
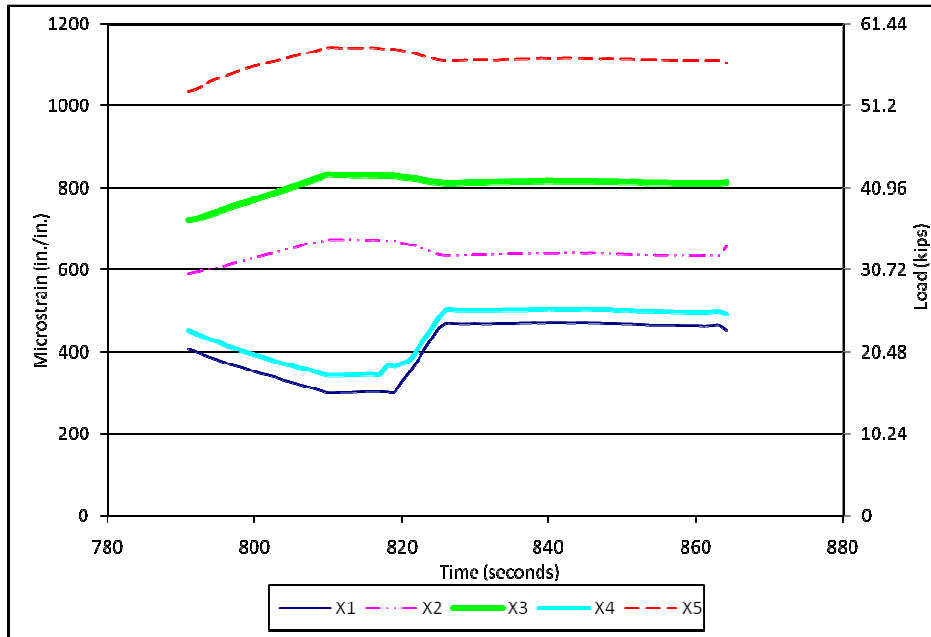
Figure B-7   Increment 10, Time History Graph
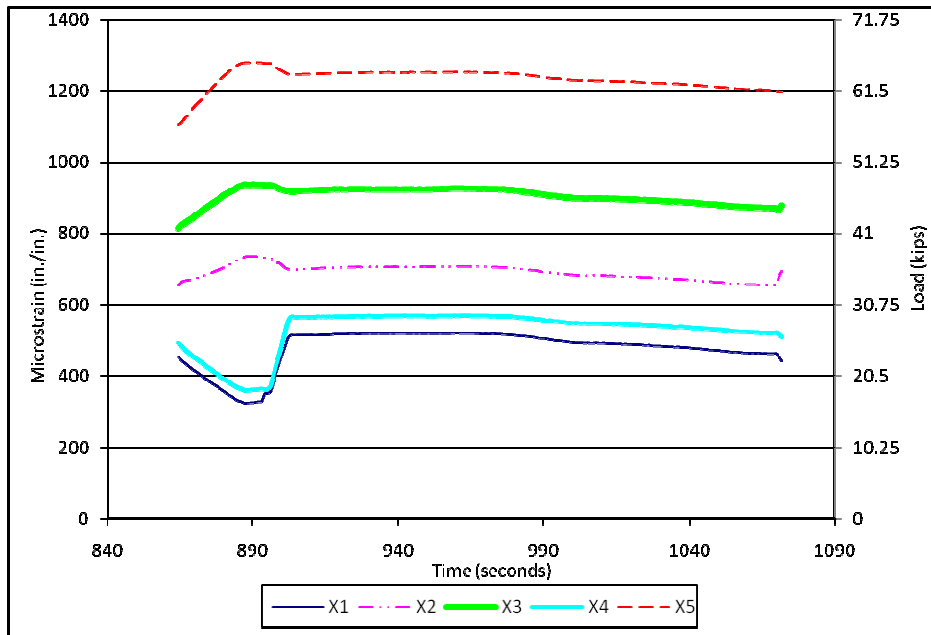
Figure B-8   Increment 11, Time History Graph
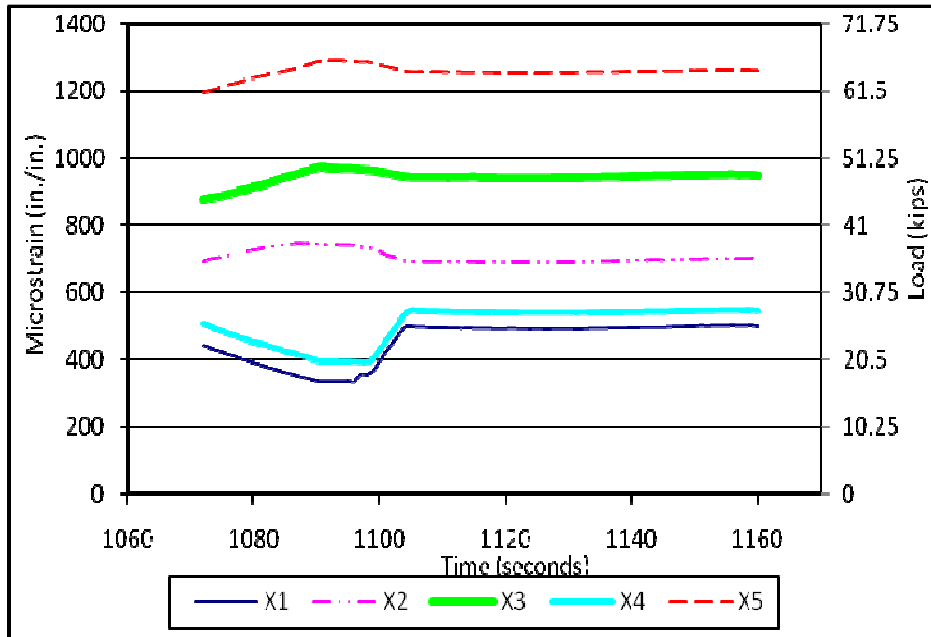
Figure B-9   Increment 12, Time History Graph
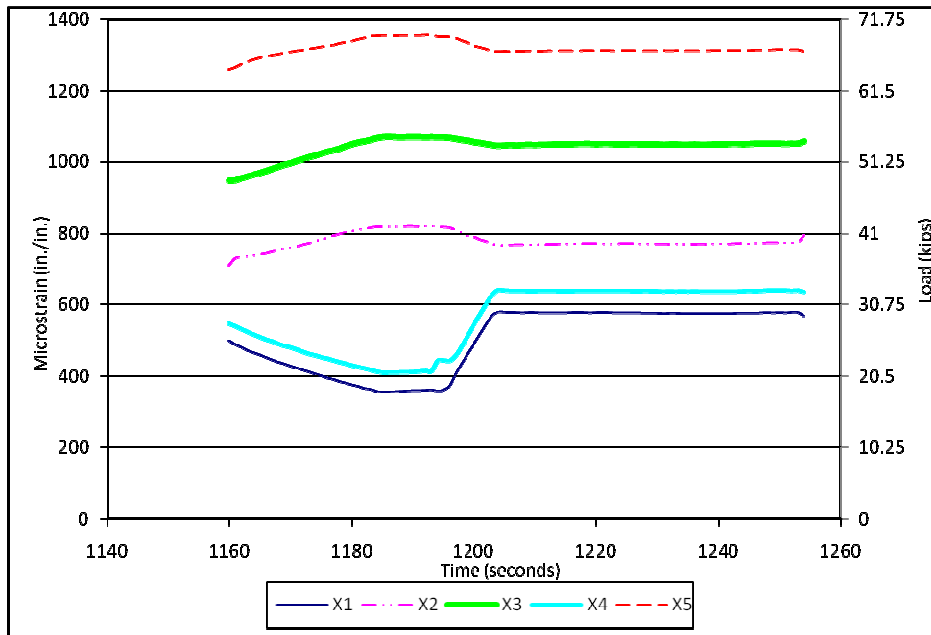
Figure B-10   Increment 13, Time History Graph
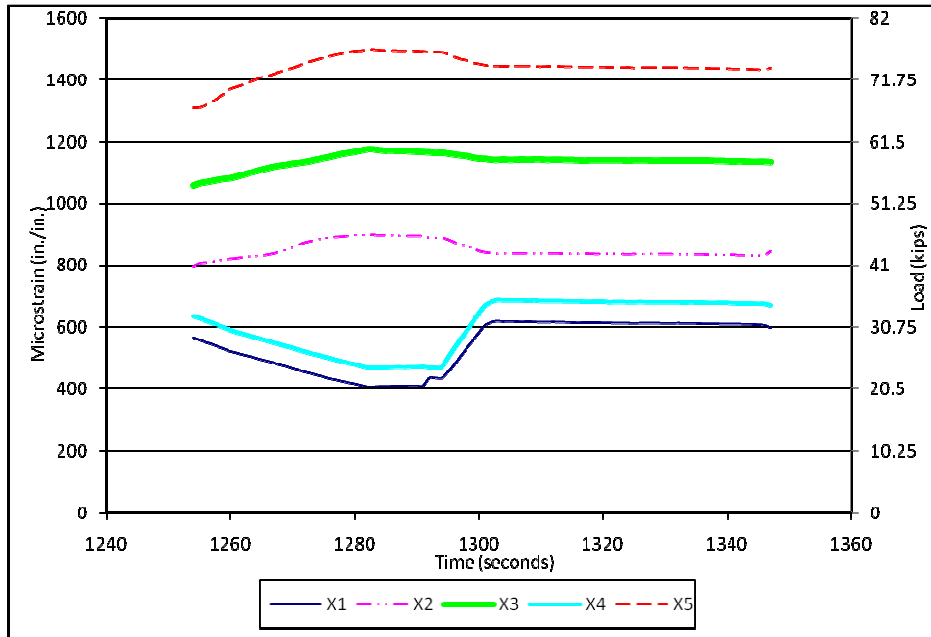
Figure B-11   Increment 14, Time History Graph
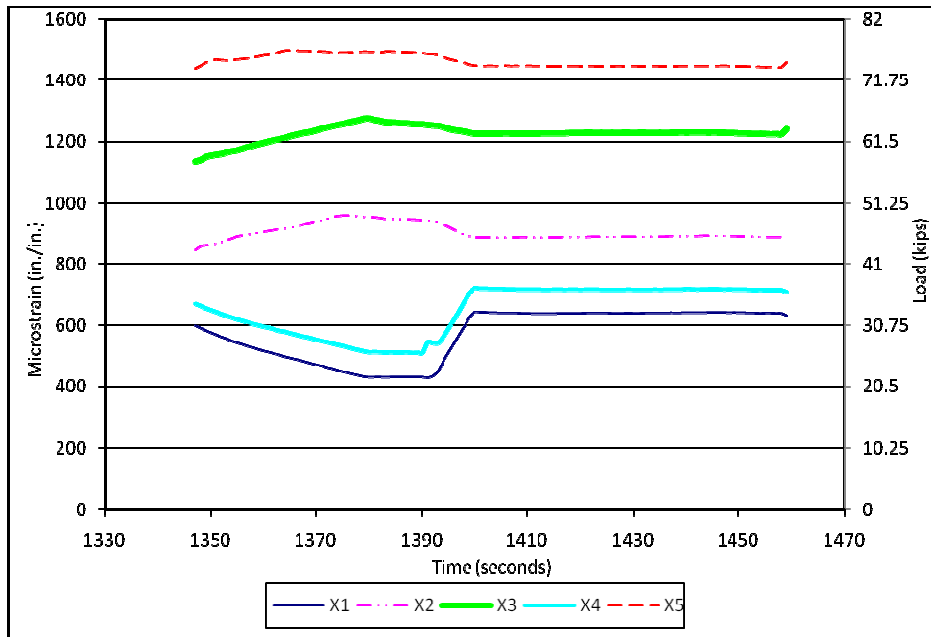
Figure B-12   Increment 15, Time History Graph

112
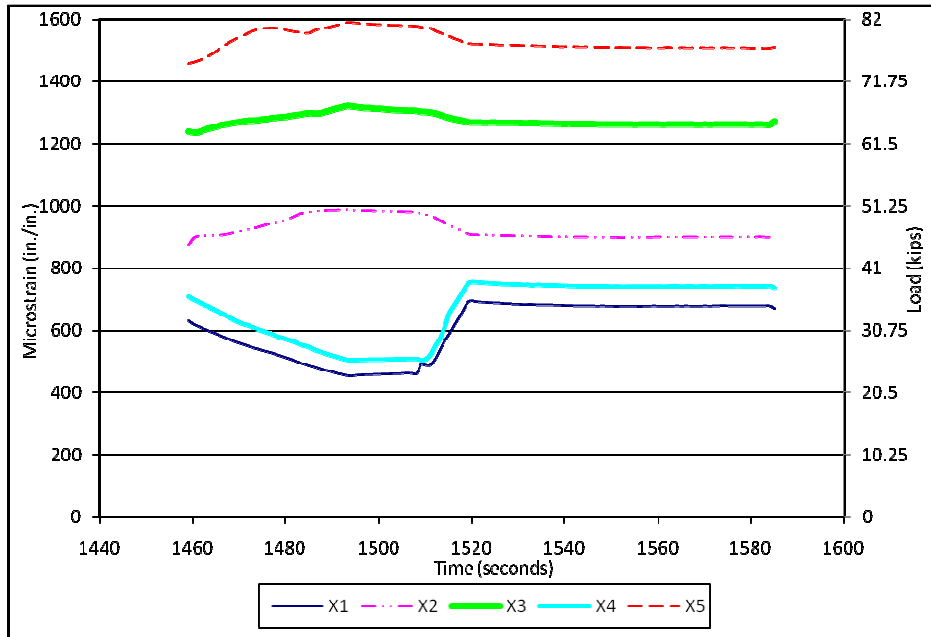
Figure B-13   Increment 16, Time History Graph
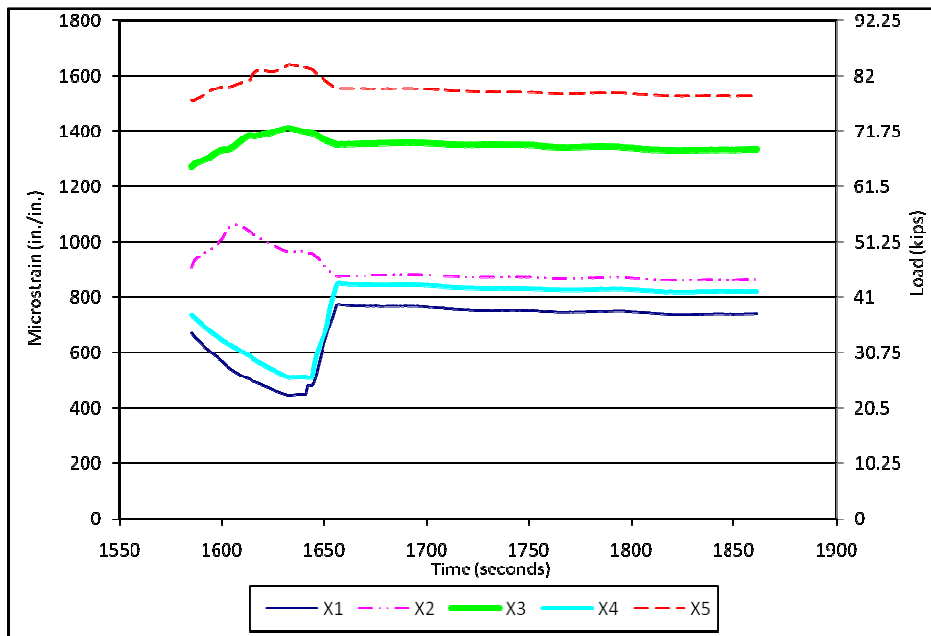
Figure B-14   Increment 17, Time History Graph

113

Appendix C

FEA Comparisons

Figures C-1 through C-6 graph truck increments versus microstrains resulting from the FEA and field testing. This is the data used to calculate the slope values presented in Tables 5.1 through 5.4. The data at each gauge location is plotted on two different graphs due to the large number of data generated at each gauge. Here one graph shows the series that involved increasing the elastic modulus in the model and the other graph shows all other analyses. The field data is shown in all graphs for comparison purposes. Specifically, Figures C-1 to C-2, C-3 to C-4, and C-5 to C-6 are graphs of Gauges G2-BF2-C, G3-A, and G4-A respectively. Figures C-1, C-3, and C-5 are graphs of field data results along with the models that had the elastic modulus of the concrete or cross frames increased. Figures C-2, C-4, and C-6 are graphs of the field test data, 1/8 elastic modulus of concrete, ½ elastic modulus of the cross frames, the original model, and both the pinned cross frame connection models.
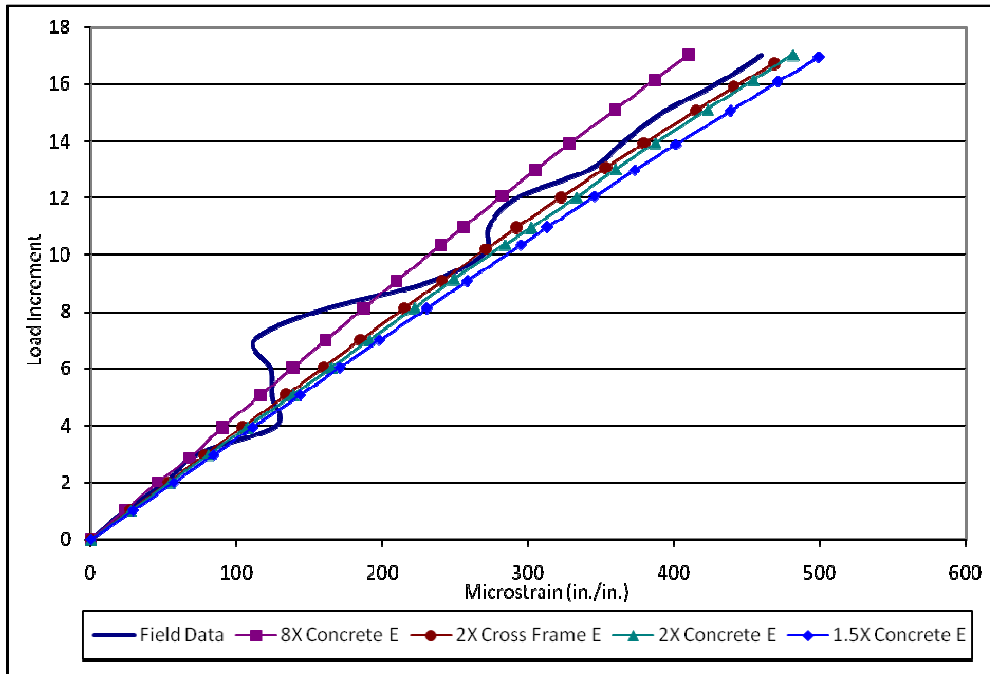
Figure C-1   Gauge G2-BF2-C Increased E FEM
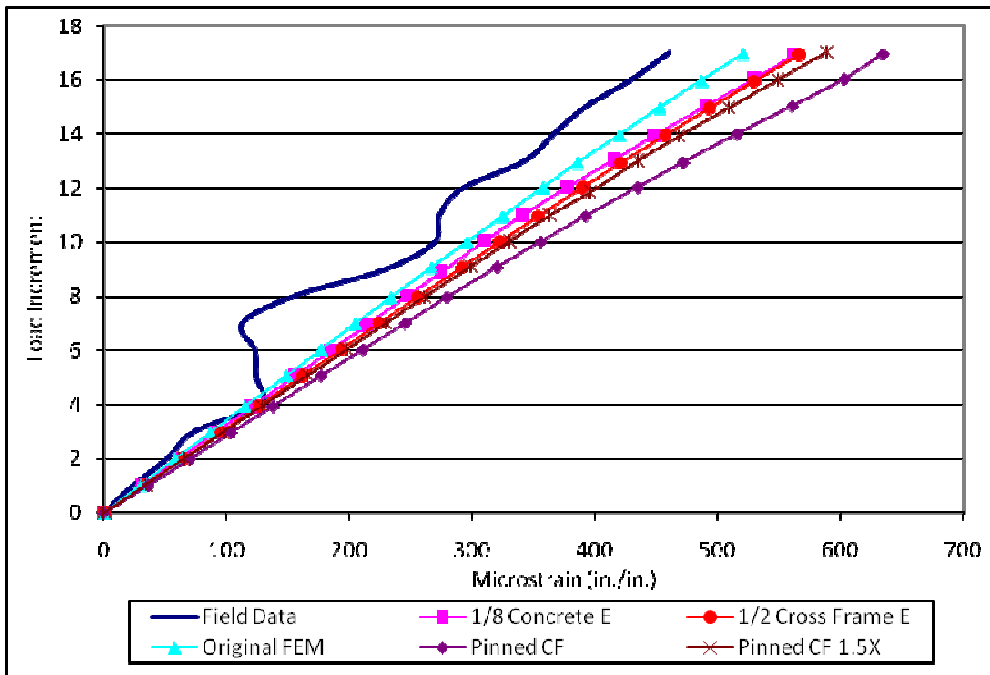
Figure C-2   Gauge G2-BF2-C Remaining FEM

115
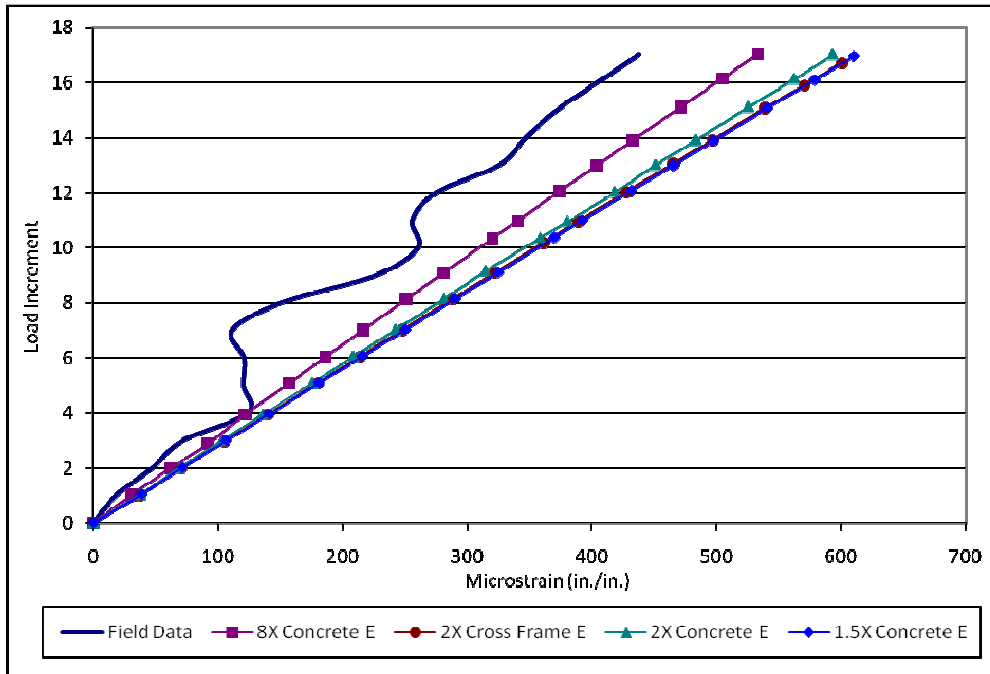
Figure C-3   Gauge G3-A Increased E FEM
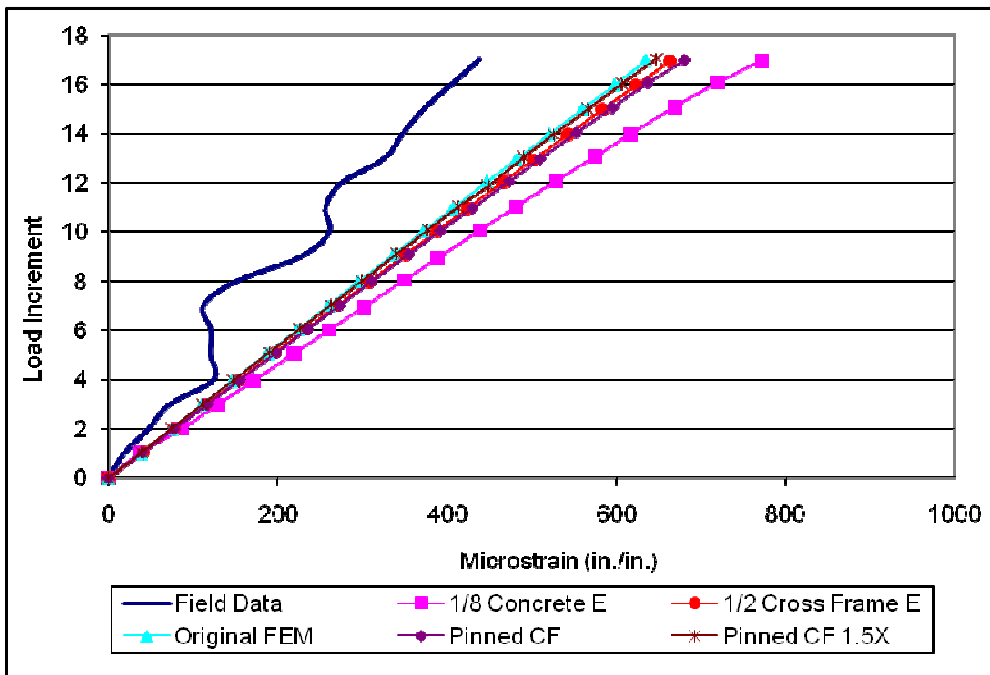
Appendix C-4   Gauge G3-A Remaining FEM
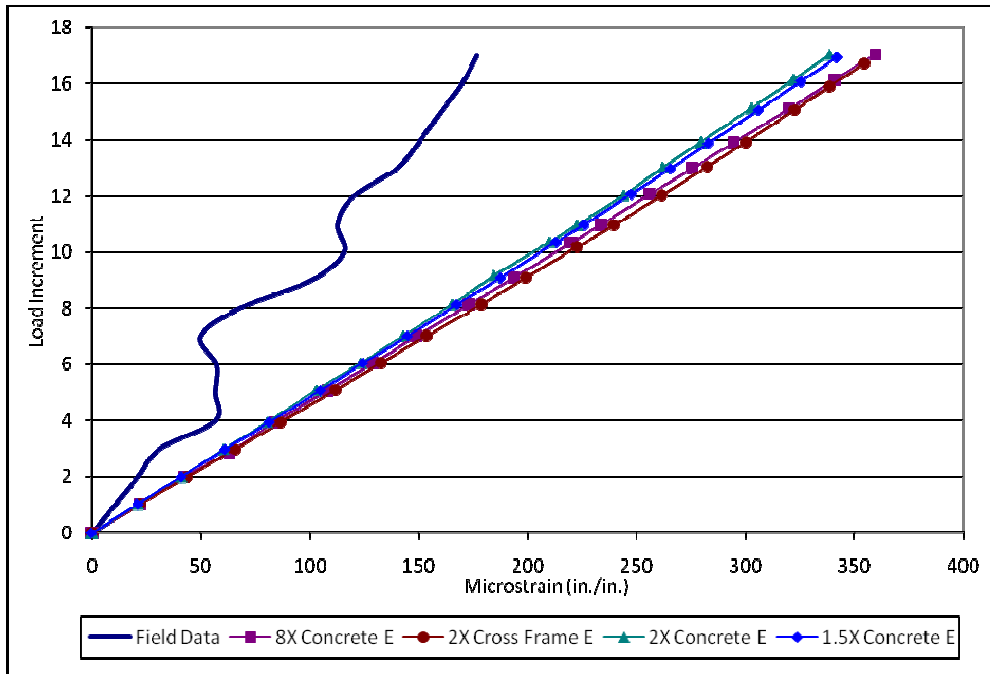
Appendix C-5   Gauge G4-A Increased E FEM
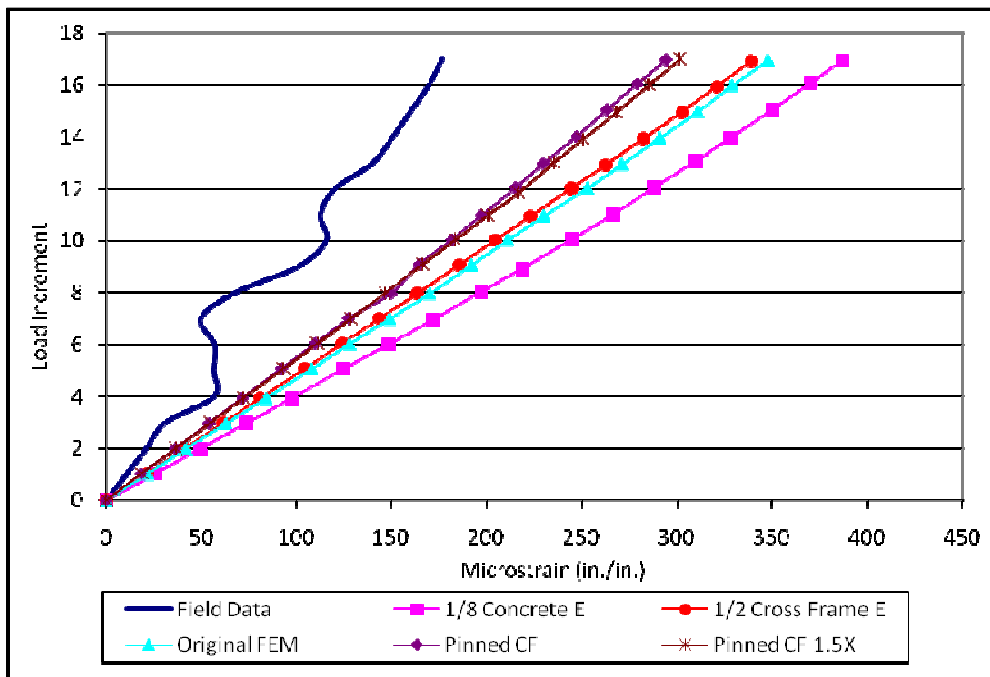
Appendix C-6   Gauge G4-A Remaining FEM

117

Appendix D

Field Data and Calibrated FEA Comparison

The graphs in Appendix D are graphs of the load increments vs. microstrains from the field test data and the calibrated FEA, which increased the elastic modulus of the concrete by 150% compared to the original model. The webs, top flanges, and Cross Frame 3 graphs (Figures D-1 to D-7) from the FEA predict greater strains than the field test at the majority of increments. The Cross Frame 4 graphs (Figures D-8 to D-10) are similar to the bottom flange comparisons of the field data and calibrated model (shown in Figures 5.1-5.4) in that the field data strains are greater than the FEA strains at the majority of the increments. The comparison between the field data and calibrated model shown in this appendix is only included for completeness. Due to the difficulty in achieving correlation between the bottom flange strains in the model and field data, no attempt was made to achieve consistency between the FEA results shown in this appendix and the field data.
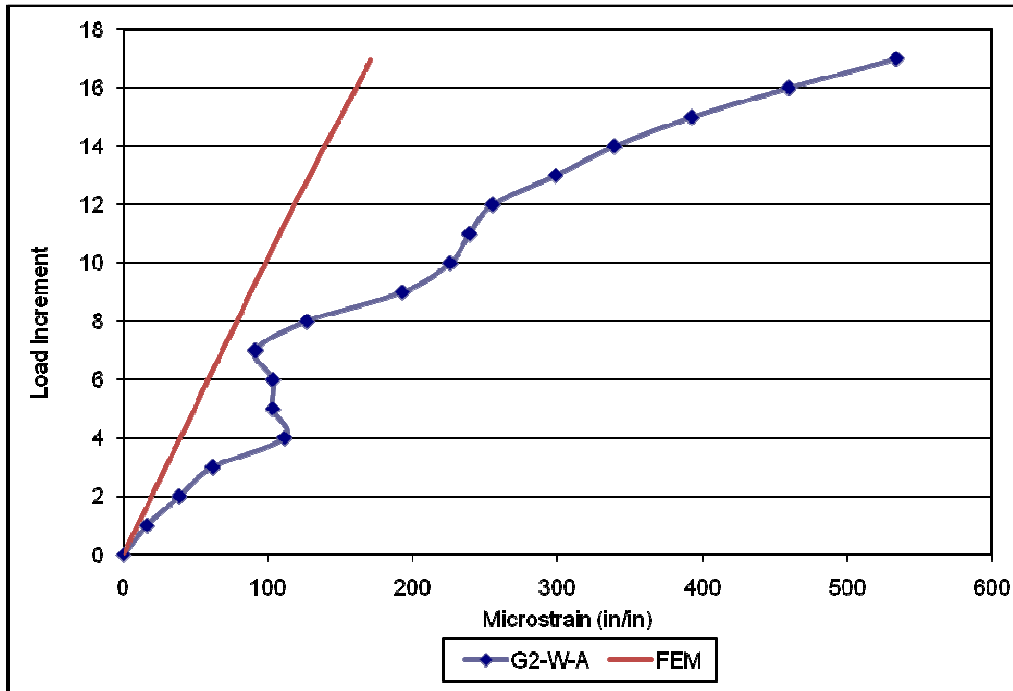
**Figure D-1   Gauge G2-W-A Field Data and FEM Results**
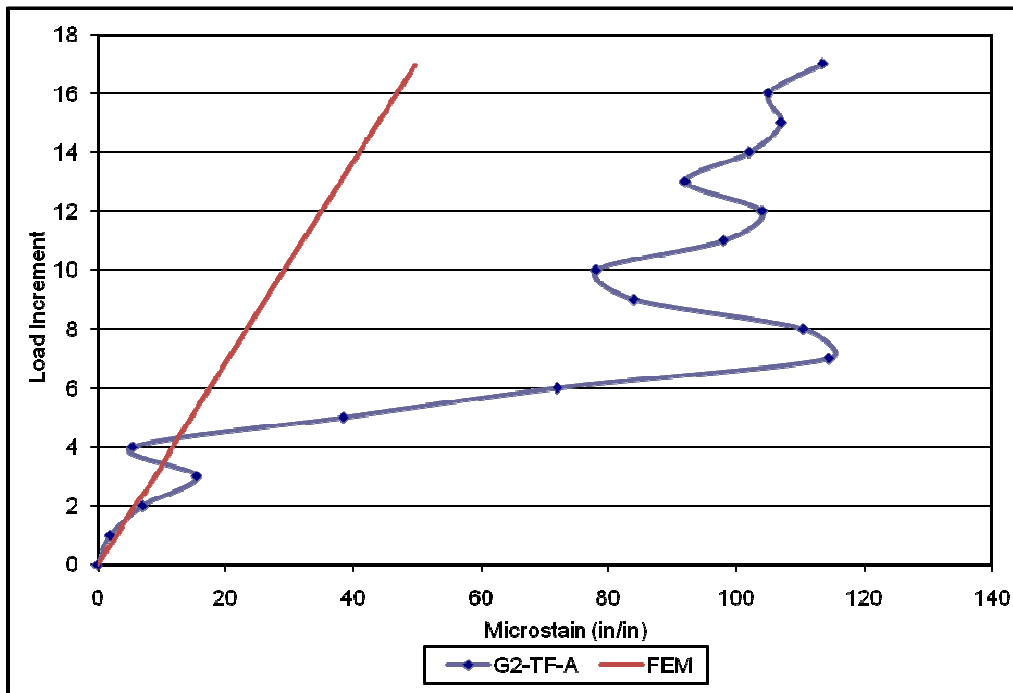
**Figure D-2   Gauge G2-TF-A Field Data and FEM Results (compression)**
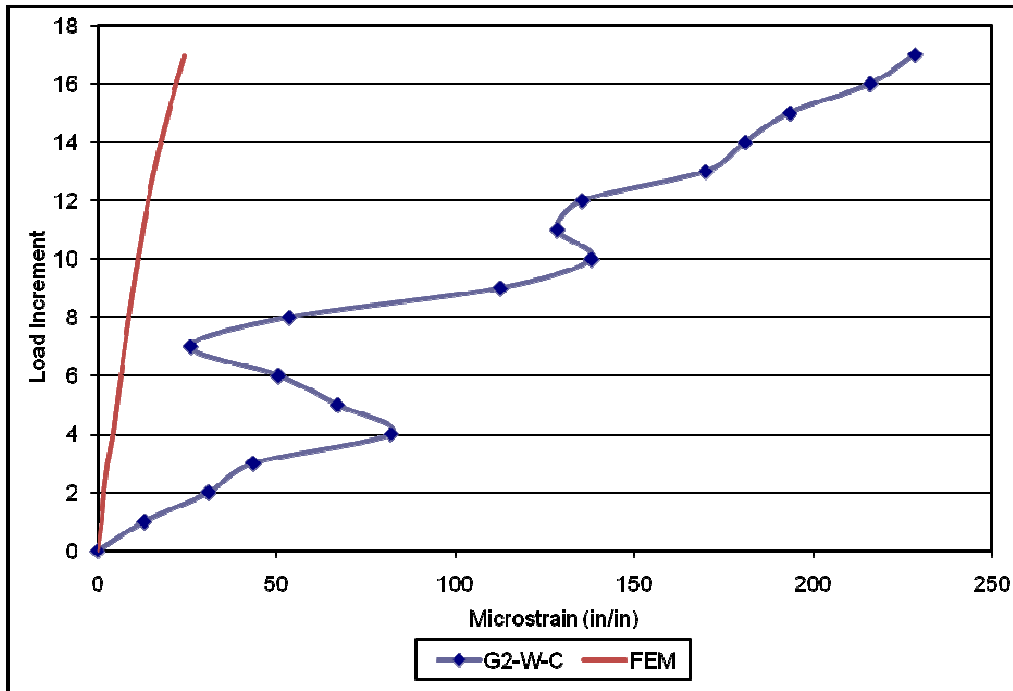
Figure D-3   Gauge G2-W-C Field Data and FEM Results
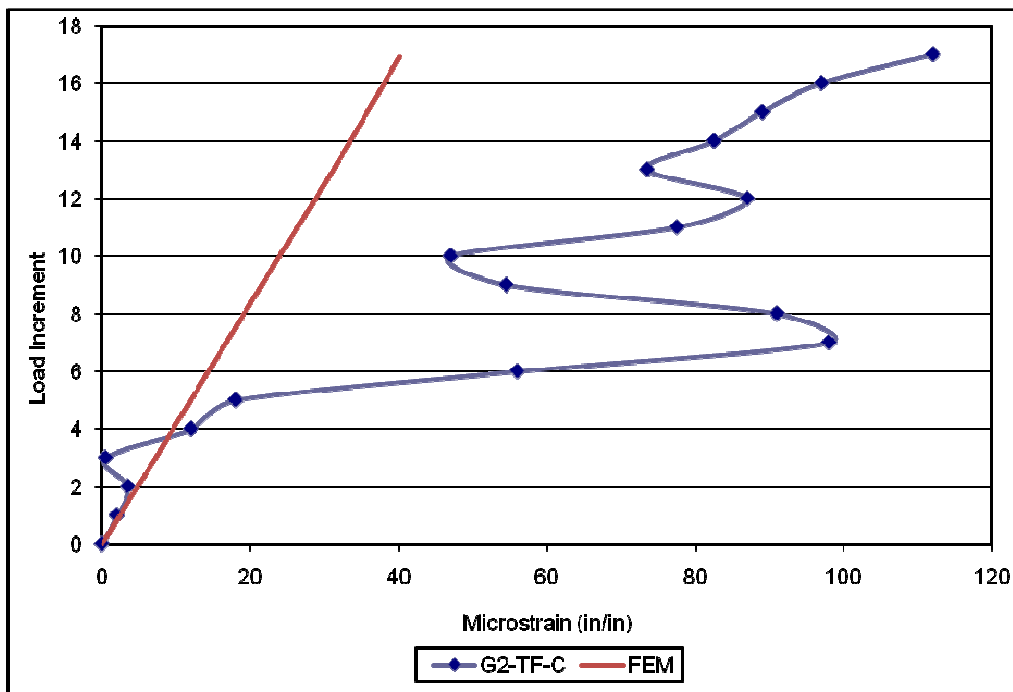
**Figure D-4   Gauge G2-TF-C Field Data and FEM Results (compression)**

120
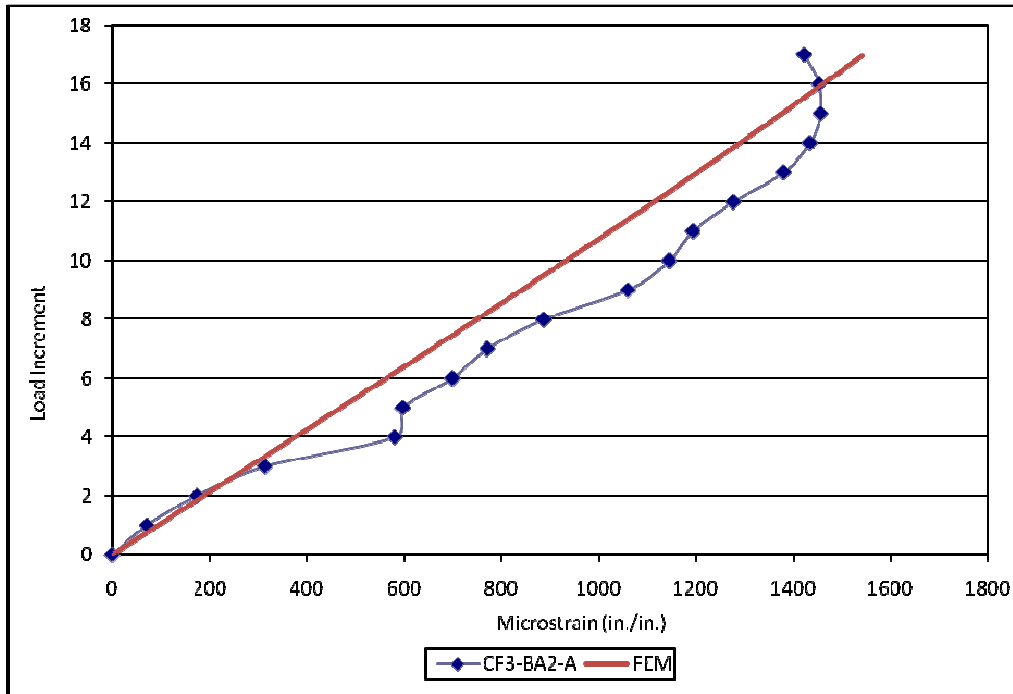
**Figure D-5   Gauge CF3-BA2-A Field Data and FEM Results**
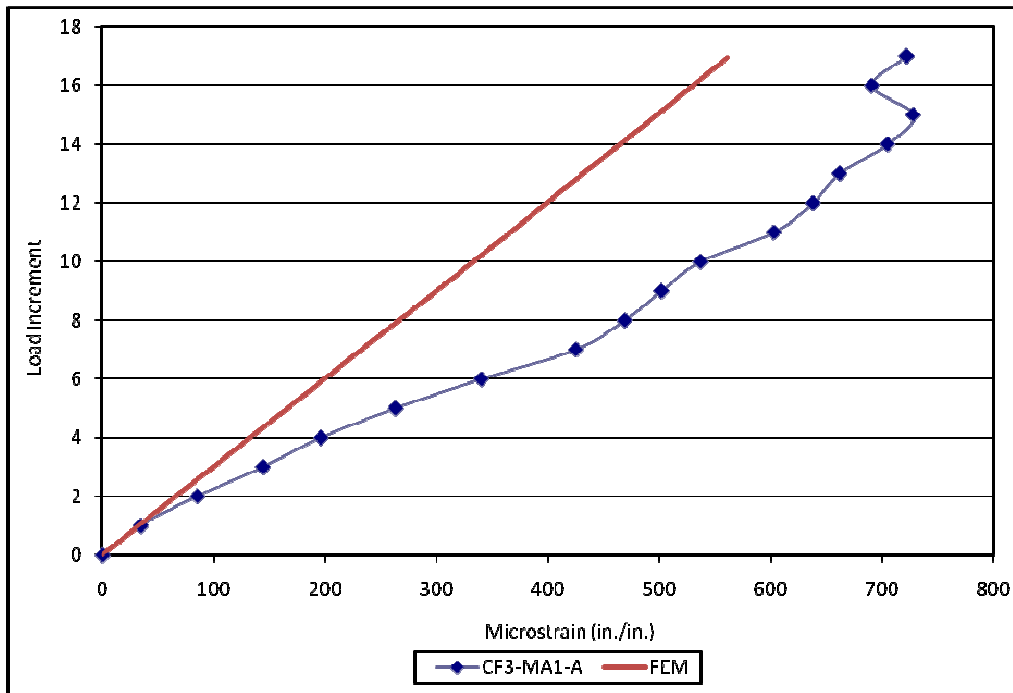
**Figure D-6   Gauge CF3-MA1-A Field Data and FEM Results (compression)**

121
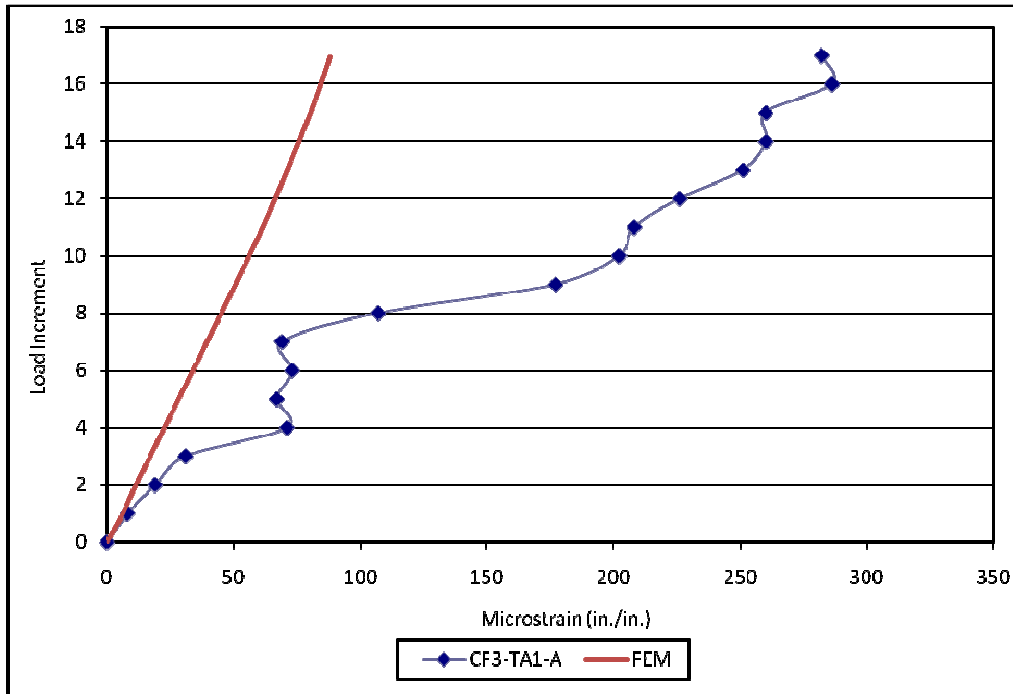
**Figure D-7   Gauge CF3-TA1-A Field Data and FEM Results**
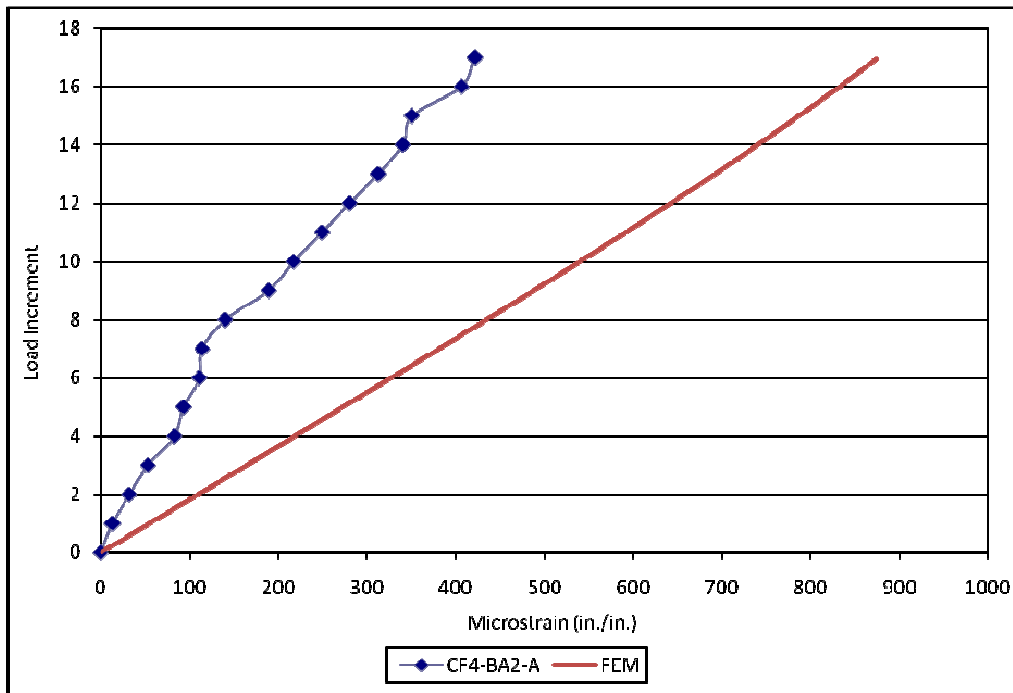
Figure D-8   Gauge CF4-BA2-A Field Data and FEM Results

122
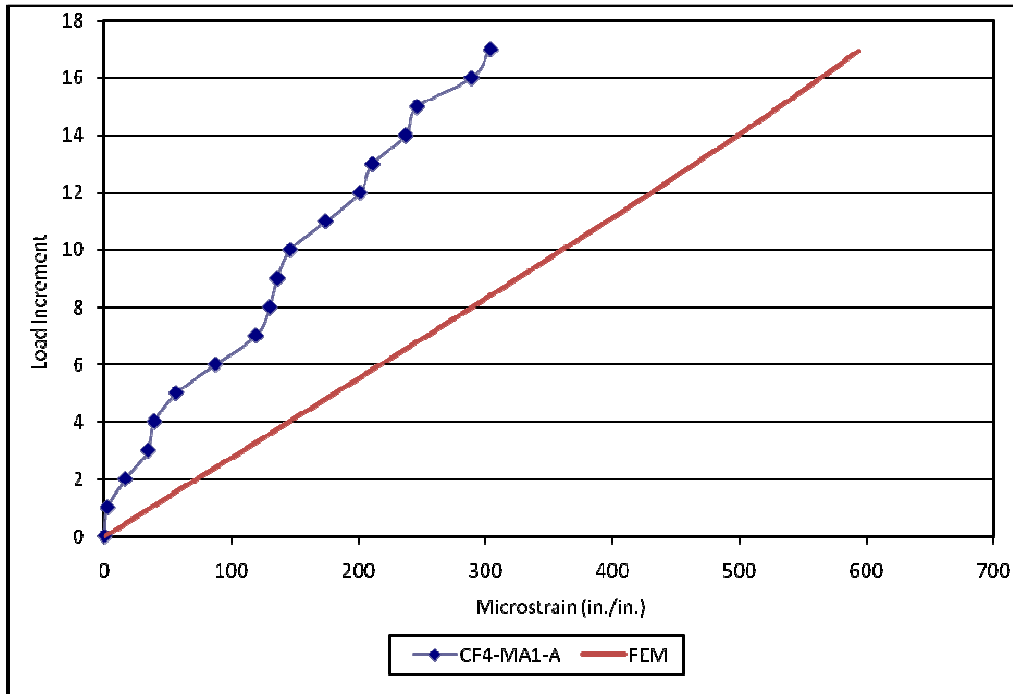
Figure D-9   Gauge CF4-MA1-A Field Data and FEM Results (compression)
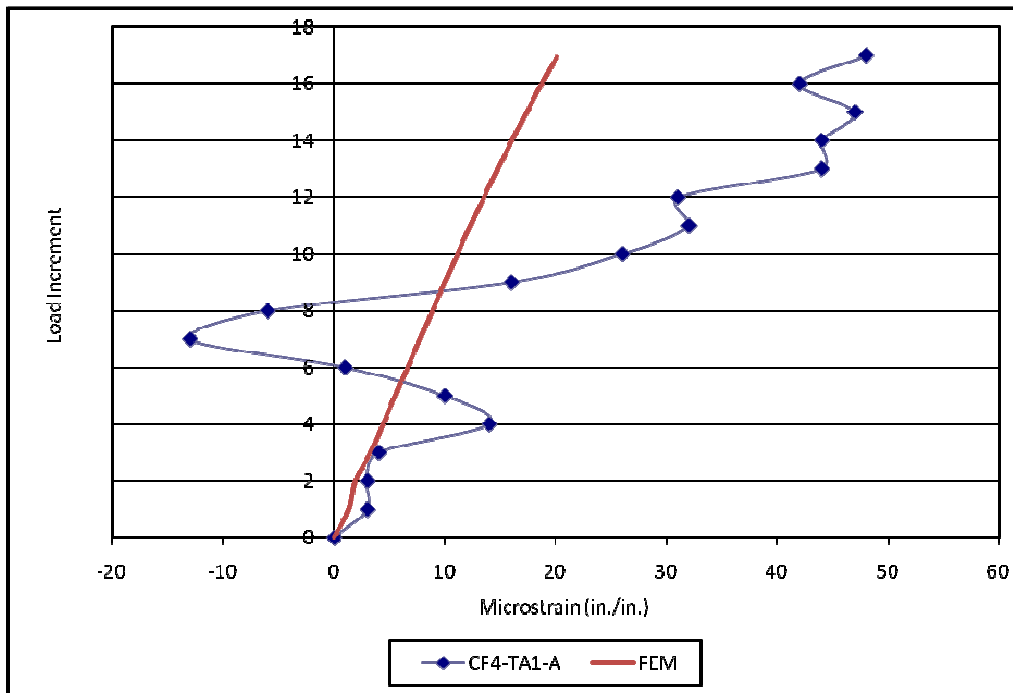

Figure D-10   Gauge CF4-TA1-A Field Data and FEM Results

123

REFERENCES

AASHTO (2010). *Load and Resistance Factor Design Bridge Design Specifications*, (SI Units, 4th Edition), American Association of State Highway Transportation Offices, Washington, D.C.

Bechtel, A.; McConnell, J.; and Chajes, M. (2011). "Ultimate Capacity Destructive Testing and Finite Element Analysis of Steel I-Girder Bridges", ASCE Journal of Bridge Engineering, 16(2), scheduled, <doi:10.1061/(ASCE)BE.1943-5592.0000137>.

McCormac, J.C., & Nelson, J.K. (2006). *Design of Reinforced Concrete ACI 318-05 Code Edition Seventh Edition.* United States: John Wiley and Sons, Inc.

Quinn, P., 2005, *Understanding Steel Bridge Behavior Through Destructive Testing*, Master's Thesis, University of Delaware, Newark, DE.

Ross, J., 2007, *Evaluating Ultimate Bridge Capacity Through Destructive Testing of Decommissioned Bridges*, Master's Thesis, University of Delaware, Newark, DE.

Salmon, C.F., & Johnson, J.E. (1996). *Steel Structures Design and Behavior Fourth Edition.* Upper Saddle River: Prentice-Hall, Inc.

Weidner, K., 2006, *Failure Analysis of a Steel Slab-On-Girder Bridge*, National Science Foundation Summer Research Experience for Undergraduates, University of Delaware, Newark, DE.